THE STUDY OF CONDENSED MATTER BY DEEP INELASTIC NEUTRON SCATTERING

by

Alan Charles Evans B.Sc.

The research presented in this thesis was conducted at the ISIS facility at the Rutherford Appleton Laboratory as part of the requirement for the degree of Doctor of Philosophy at the University of Warwick.

August 1993.

VARIABLE PRINT QUALITY

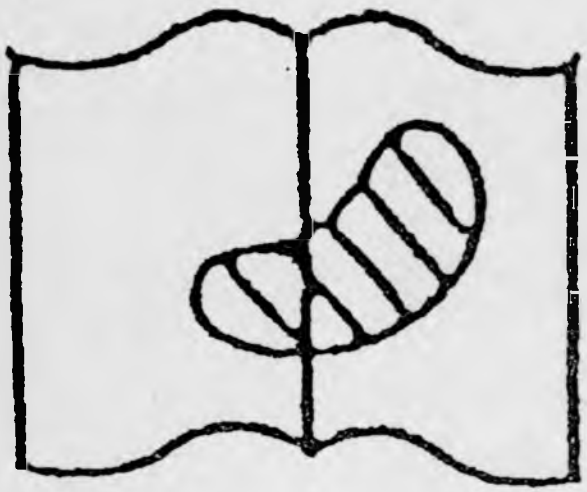

ABSTRACT

Electron-Volt Neutron Spectroscopy of Condensed Matter

This thesis describes the technique of electron-volt neutron spectroscopy at the pulsed spallation neutron source ISIS at the Rutherford Appleton Laboratory. A number of systems were studied, with the emphasis on the validity of the impulse approximation in each case. Assuming a Gaussian momentum distribution, the mean kinetic energies of ZrH_2, ZrD_2, NbH and NbD and lithium metal between 20 K and 300 K were measured. By numerical calculation, it is shown that anharmonicity in metal hydride systems can be dealt with in terms of a Gaussian momentum distribution, as for harmonic systems. The vibrational density of states of H in ZrH_2 was determined from inelastic neutron scattering measurements of the dynamic structure factor made on the MARI spectrometer, and used to perform exact numerical simulations of eVS measured neutron Compton profiles for a range of momentum transfers. The deviations of these simulated data from the impulse approximation due to final state effects were compared to deviations from the impulse approximation of data measured on eVS. It is shown that these deviations are small enough to be treated by a straightforward correction procedure.

THE STUDY OF CONDENSED MATTER BY DEEP INELASTIC NEUTRON SCATTERING

CONTENTS

ACKNOWLEDGEMENTS

I have been fortunate enough to work with many helpful people at the Rutherford Appleton Laboratory for the best part of three years. I thank the Science and Engineering Research Council for granting me a three year studentship, the Rutherford Appleton Laboratory for allowing me to continue to work on eVS since November 1992 when my SERC studentship ended, and those at the Rutherford Appleton Laboratory who have helped me along the way.

I am grateful to Dr. G. Styles of the University of Warwick, who permitted the use of the hydriding apparatus under his care. Special thanks are due to Dr. Jerry Mayers, instrument scientist for eVS who supervised my work at the Rutherford Appleton Laboratory, Dr. Steven Bennington for his help in the MARI experiments, Professor Malcolm Cooper, my Ph.D. Supervisor, and Dr. David Timms at Portsmouth University, who has continued to work closely with me on eVS.

DECLARATION

The experimental work presented in this thesis was performed on the Electron-Volt Spectrometer (eVS). The analysis procedures described in chapter 2 are due largely to the instrument scientist Dr. Jerry Mayers. Chapter 3 presents measurements on zirconium hydride. The MARI experiments were performed with the help of Dr. S. N. Bennington, instrument scientist of MARI. The data reduction used in chapter 3 to derive a density of states from these measurements was designed and performed solely by the author. The FORTRAN program for the numerical simulation of eVS data from the density of states is due to Dr. J. Mayers. Chapter 4 presents measurements on metal hydrides and deuterides. These were manufactured at the University of Warwick by the author with the help of Dr. D. N. Timms. The eVS measurements were performed by the author. The numerical and analytical calculations of the momentum distribution of a particle in an anharmonic potential are entirely due to the author. Finally, the lithium experiment was performed in collaboration with Dr. J. Mayers, Dr. D. N. Timms and Prof. M. J. Cooper.

FIGURE CAPTIONS

Figure 1.1 The incoherent approximation. The term $\mathbf{q} \cdot [\mathbf{r}_j(t) - \mathbf{r}_j(0)]$ will always be much greater than 2π (see text) and so $\langle \exp(\mathbf{q} \cdot [\mathbf{r}_j(t) - \mathbf{r}_j(0)]) \rangle$ will average out to zero. Hence terms with $i \neq j$ in equation 10 can be neglected.

Figure 1.2 Illustration of how the neutron Compton profile $J(y)$ is calculated. $J(y)$ is an integration of $n(\mathbf{p})$ over a plane R perpendicular to $\mathbf{q}$ at a distance y from the origin of atomic momentum space (known as y-space). In the simple illustration, $n(\mathbf{p})$ is a solid sphere and $J(y)$ is the area of intersection of the sphere and the plane R.

Figure 2.1 Detector scans on eVS through (q, ω) space. For the experiments described in this thesis, the eVS had forty detectors at forward scattering angles. Thirty of these were at angles useful for hydrogen scattering, which are considered for convenience grouped together in three banks of detectors 36° to 44° (bank A), 46° to 54° (bank B) and 57° to 66° (bank C). Each detector scan for each bank lies in the shaded region A B or C marked on the figure. The dashed curves represent the peak position and HWHM of $S(q, \omega)$ in the case of scattering from ZrH_2.

Figure 2.2 Momentum distribution for a particle in a one-dimensional double potential well. The potential is $V(x) \propto (x - a)^2 + (x + a)^2$. The first two maxima occur at $p/\hbar = \pi/a$. The momentum distribution shown is for $a = 1.8$ Å.

Figure 2.3 A series of time-of-flight difference measurements of ZrH_2 measured on one of the low-angle detector banks on eVS. The broad peak is scattering from hydrogen, while the narrow peak is scattering from aluminium (in the sample holder) and zirconium. Note how the separation of the two peaks and the width of the hydrogen peak both become larger at higher scattering angles.

Figure 2.4 The effective thermal neutron flux from laboratory (□), reactor (○) and accelerator based neutron sources (△) (from [2]).

Figure 2.5 The effective neutron flux for the cold, thermal and hot sources on the ILL

reactor at Grenoble, (...), and the liquid H_2, liquid methane and ambient water (AP) moderators on the pulsed neutron source ISIS at the Rutherford Appleton Laboratory (from [2]).

Figure 2.6 Principle of the filtered beam spectrometer in direct (2.6a and 2.6b) and inverse (2.6b and 2.6c) geometries.

Figure 2.7a Principle of the chopper spectrometer.

Figure 2.7b Principle of the resonance detector spectrometer. This operates in inverse geometry and uses a scintillation detector (n+γ) to observe the gamma-ray cascade that results when a neutron is absorbed in the vicinity of the strong resonance at $E = E_R$ possessed by the analyser foil.

Figure 2.8 The resolution of direct and indirect geometry spectrometers. The solid line is $\Delta E_R/\omega$ for an inverse geometry machine that uses a gold analyser foil ($\Delta E_R \simeq 140$ meV) and has primary and secondary flight paths of 11m and 1m respectively. The broken line is $\Delta E_R/\omega$ for a direct geometry machine with primary and secondary flight paths of 6m and 3m respectively.

Figure 2.9a Detector scans through (q, ω) space for angles of 20, 40 and 60 ° for scattering from hydrogen and for inverse and direct geometry. The calculations are performed for a gold analyser foil ($E_R = 4922$ meV and $\Delta E_R = 140$ meV). The DG scans are the three solid lines and the IG scans are the dashed lines. The dotted-dashed lines mark the maximum and the FWHM of $S(\mathbf{q}, \omega)$ for hydrogen in ZrH_2 which has a momentum distribution variance of 4.18 $Å^{-1}$.

Figure 2.9b Detector scans through (q, ω) space for angles of 20, 40 and 60 ° for scattering from hydrogen and for inverse and direct geometry. The calculations are performed for a uranium analyser foil ($E_R = 6671$ meV and $\Delta E_R = 140$ meV). The DG scans are the three solid lines and the IG scans are the dashed lines. The dotted-dashed lines mark the maximum and the FWHM of $S(\mathbf{q}, \omega)$ for hydrogen in ZrH_2 which has a momentum distribution variance of 4.18 $Å^{-1}$.

Figure 2.10 The Electron Volt Spectrometer. Pulses of neutrons with a wide range of energies arrive from the moderator. Neutrons scattered into a specific energy defined by resonant foils around the sample are detected by fifty ^{3}He neutron detectors arranged symmetrically about the incident beam direction. Information on the momentum distribution of the target particles is deduced from the time-of-flight spectra measured with the resonant foils in and out of the scattered beam. The thirty detectors at lowest scattering angles are grouped together in three banks referred to in the text as banks A, B and C. These are marked in the figure.

Figure 2.11 A 'foil in' (+) and a 'foil out' (solid line) time-of-flight spectrum for a measurement on ZrH_2 at an angle of 36 °. The spectra are normalised so that they have the same integrated counts between 500 and 600 μs. The difference between the two is the difference time-of-flight spectrum.

Figure 2.12 Schematic diagram of an inverse geometry spectrometer.
L_0 = incident flight path
L_1 = scattered flight path
θ = scattering angle
E_0 = energy of incident neutron
E_1 = energy of detected neutrons

Figure 2.13 For the length calibration of eVS, a uranium foil is placed in the incident beam and the positions in time-of-flight of three uranium resonances at 6671, 20872 and 36680 meV are located for each detector. Shown is one such spectrum (detector 11 for which $2\theta = 35.96°$).

Figure 2.14 The calculated eVS resolution function in time-of-flight for scattering from H and for detector 11. For the purposes of 'can-subtraction' a resolution function is required in time-of-flight. For fitting to the measured neutron Compton profile in y-space, a resolution function is needed in y-space. Each function is calculated as a Voigt function with Gaussian and Lorentzian components determined from the uncertainties

in the five instrument parameters. Their compatability is demonstrated in this and the next figure.

Figure 2.15 The calculated eVS resolution function in y-space is a Voigt-function centred at $y = 0$. Shown is the resolution function for scattering from hydrogen (...). The Lorentzian component is determined from the calibrated HWHM of the analyser foil resonance. The variance of the Gaussian component is the sum (added in quadrature) of the individual y uncertainties corresponding to the uncertainties in the flight paths L_0 and L_1, uncertainty in the measurement of the time of flight, and the scattering angle 2θ. The continuous line is the y-transformed resolution function of figure 2.14.

Figure 2.16 The Lorentzian HWHM (determined by fitting) of the calculated Voigt resolution function in E_1 space as a function of momentum transfer (which increases with increasing scattering angle) for scattering from hydrogen ($\triangle$) and from deuterium ($\bigtriangledown$). The dashed line represents the Lorentzian contribution from the analyser foil.

Figure 2.17 The ratio of the fitted Lorentzian HWHM to the Voigt resolution function in y-space to the variance of the system being studied. The top line is for scattering from deuterium, whilst the lower curve is for scattering from hydrogen. This is the true criterion for the resolution of an eV spectrometer.

Figure 2.18 A calculation (circles) of the transmission $P_A(E)$ of neutrons by a gold analyser foil at 290K with a thickness of 10.59 μm. This is the measured thickness of the analyser foils used on the eVS spectrometer. The solid line is a Lorentzian fit to the calculation.

Figure 2.19 The fitted Lorentzian HWHM of the calculated transmission $P_A(E)$ of a gold analyser foil at 290K.

Figure 2.20 The time-of-flight difference for scattering from a sample of $ZrH_{1.96}$ at an angle of 35.96 ° – i.e. the difference resulting from the foil-in foil-out procedure applied to one ^{3}He detector. The fit to the quasi-elastic scattering from the zirconium

and aluminium in the sample-holder is shown (solid line). The scattering from Al and Zr is represented by the sum of two Voigt functions. Each Voigt function is centred at the time-of-flight recoil-peak position for scattering from the mass concerned.

Figure 2.21 As figure 2.20 except this is at a scattering angle of 53.67° and so the hydrogen peak is shifted to significantly lower times-of-flight, corresponding to higher energy and momentum transfers. Again, the line is the fit to the scattering from the Zr and Al.

Figure 2.22 The y-transformed data of the hydrogen signal in figure 2.21 (for a single detector at a scayttering angle of 53.67 °. The solid line is the fit to the data (see item 4 in section 2.7.4).

Figure 3.1 The neutron diffraction pattern of ϵ-ZrH_2 powder obtained from Goodfellow Metals Ltd (sample A). All peaks with d-spacings greater than 1 Å have been identified as being either aluminium Bragg peaks from the sample holder or from ϵ-phase ZrH_2.

Figure 3.2 The neutron diffraction pattern of ϵ-ZrH_2 powder manufactured at the University of Warwick (sample B). All peaks with d-spacings greater than 1 Å have been identified as being either aluminium Bragg peaks from the sample holder or from ϵ-phase ZrH_2.

Figure 3.3 The sample geometry for MARI run 659.

Figure 3.4 This is the sample arrangement used for MARI runs 1071 and 1072. The sample is contained between two concentric aluminium tubes, whose common axis is perpendicular to the incident beam. It is designed to make the scattering isotropic.

Figure 3.5 The raw $S(q,\omega)$ data of sample B (run 1071) collected on the MARI spectrometer. The sample had cylindrical geometry and the energy of the incident beam was 220 meV. The density of states of the hydrogen vibrations is extracted from the first optical peak, seen here centred at about 140 meV. The intense peak centred at zero meV and extending to high q is the elastic peak.

Figure 3.6 The raw $S(q,\omega)$ data of sample B (run 1072) collected with the MARI spectrometer. The energy of the incident beam was 450 meV. At this incident energy, the first, second and third optical peaks are visible.

Figure 3.7 The extrapolated function $g(q,\omega)$ as a function of momentum transfer and at $\omega = 146$ meV. The data points (+) are obtained from the first optical peak of $S(q,\omega)$ through equation 89.

Figure 3.8 The vibrational density of states of H in ZrH_2 obtained from MARI run 659 of slab geometry (circles) and run 1071 of cylindrical geometry (boxes). Both runs were made with an incident energy of 220 meV. The similarity of the derived density of states for these two different geometries indicates that multiple scattering effects are small.

Figure 3.9 The vibrational density of states of H in ZrH_2 obtained from MARI run 1072 (boxes) (with an incident energy of 440 meV) against those from run 659 (circles) and run 1071 (triangles). The energy resolution of run 1072 is poorer because of the higher energy.

Figure 3.10 The multiple Gaussian fit to the density of states determined from MARI run 659 (solid line) is compared to the data (+). The fit was performed with the FRILLS package [55]. See the text for the fit parameters.

Figure 3.11 Simulations of eVS time-of-flight spectra for scattering from hydrogen in ZrH_2. The simulations are based on the measurement of the vibrational density of states determined from MARI run 659 (shown in figure 3.8) and are an exact numerical simulation in the harmonic incoherent approximation. The simulations shown are for detectors 11 and 20 at scattering angles of 35.96 and 53.68 °. The individual multiphonon excitations are visible in the peak centred at about 310 μs. At the higher momentum transfers reached at 53.68 ° the individual excitations merge together. The data shown are not resolution convoluted.

Figure 3.12 A comparison of a measurement of $J_m(y)$ made at an average momentum

transfer of 40.8 $Å^{-1}$ on eVS (+) compared to an exact simulation of the data based on the density of states of the hydrogen vibrations measured with the MARI spectrometer (solid line). Also shown is the result obtained in the impulse approximation (dotted line) and the difference between this and the simulation (lower solid line). y-scaling has been used to convert from time-of-flight to momentum-space.

Figure 3.13 As figure 3.12 except made at an average momentum transfer of 57.6 $Å^{-1}$.

Figure 3.14 As figure 3.12 except made at an average momentum transfer of 91.2 $Å^{-1}$.

Figure 3.15 A comparison of a measurement of $J_m(y)$ made at an average momentum transfer of 40.8 $Å^{-1}$ on eVS (+) compared to an exact simulation of the data based on the density of states of the hydrogen vibrations measured with the MARI spectrometer (solid line). Also shown is the result obtained in the impulse approximation (dotted line) and the difference between this and the simulation (lower solid line). $y1$-scaling has been used to convert from time-of-flight to momentum-space.

Figure 3.16 As figure 3.15 except made at an average momentum transfer of 57.6 $Å^{-1}$.

Figure 3.17 As figure 3.15 except made at an average momentum transfer of 91.2 $Å^{-1}$.

Figure 3.18 The positions of the recoil peaks in y-space are shown for the sum of three eVS measurements (circles) as a function of the momentum transfer of the measurements. Also shown (dashed line) is the same for the numerical simulation.

Figure 3.19 The eVS σ valued determined from the sum of three eVS measurements (circles). They are plotted against the σ values determined from the numerical simulation from the density of states.

Figure 3.20 The density of states derived from MARI run 659 (triangles) and used to

simulate eVS measured neutron Compton profiles in chapters 3 and 4. It is compared to a previously (and erroneously) calculated density of states. The small difference in mean kinetic energy determined from these two similar densities of states demonstrates the weak dependence of the determined mean kinetic energy on the exact form of the density of states.

Figure 3.21 A detail of figure 3.18 in the range 20 to 120 $Å^{-1}$. The simulation (dashed line) clearly indicates the movement of the fitted peak position towards the impulse approximation result at higher q. The eVS data also show this tendency.

Figure 4.1 The broad Gaussian is the momentum distribution (n(p)) for a harmonic potential with ω=100 meV (the (100) mode in NbD) and mass $M = 2.014$ amu. With a 30 % x^4 perturbation, the perturbed momentum distribution (narrow Gaussian) can be fitted well by a Gaussian (+). The oscillating line at the bottom is the difference between the perturbed n(p) and the fit.

Figure 4.2 The ϵ-phase ZrH_2/ZrD_2 unit cell showing the bonds between one of the interstitial atoms and the nearest neighbour Zr atoms.

Figure 4.3 The β-phase NbH/NbD unit cell showing the bonds between one of the interstitial atoms and the nearest neighbour Nb atoms.

figure 4.4 The apparatus used for preparation of metal hydrides and deuterides.

Figure 4.5 The measured NCP (circles) and the numerical calculation of the measured NCP (solid line) for ϵ-phase $ZrH_{1.96}$ for the momentum transfer range 35.4 - 46.5 $Å^{-1}$.

Figure 4.6 The measured NCP (circles) and the numerical calculation of the measured NCP (solid line) for ϵ-phase $ZrH_{1.96}$ for the momentum transfer range 50.2 - 66.4 $Å^{-1}$.

Figure 4.7 The measured NCP (circles) and the numerical calculation of the measured NCP (solid line) for ϵ-phase $ZrH_{1.96}$ for the momentum transfer range 76.6 - 109.9 $Å^{-1}$.

Figure 4.8 The measured NCP (circles) and the numerical calculation of the measured NCP (solid line) for ϵ-phase $ZrH_{1.96}$ for the momentum transfer range 123.6 - 211.7 $Å^{-1}$.

Figure 4.9 The measured NCP (circles) and the numerical calculation of the measured NCP (solid line) for ϵ-phase $ZrD_{2.00}$ for the momentum transfer range 32.0 - 39.7 $Å^{-1}$.

Figure 4.10 The measured NCP (circles) and the numerical calculation of the measured NCP (solid line) for ϵ-phase $ZrD_{2.00}$ for the momentum transfer range 41.9 - 50.4 $Å^{-1}$.

Figure 4.11 The measured NCP (circles) and the numerical calculation of the measured NCP (solid line) for ϵ-phase $ZrD_{2.00}$ for the momentum transfer range 54.7 - 64.8 $Å^{-1}$.

Figure 4.12 The measured NCP (circles) and the numerical calculation of the measured NCP (solid line) for ϵ-phase $ZrD_{2.00}$ for the momentum transfer range 67.8 - 79.0 $Å^{-1}$.

Figure 4.13 The fitted peak position (circles) of the measured NCP, as a function of momentum transfer q in ϵ-phase $ZrH_{1.96}$ at 290 K. The horizontal line at $\sigma = 4.18$ is the result obtained from the numerical simulation.

Figure 4.14 σ (circles) as a function of momentum transfer q in ϵ-phase $ZrD_{2.00}$ at 290 K. The horizontal line at $\sigma = 4.96$ is the result obtained from the density of states.

Figure 4.15 The fitted peak position (circles) of the measured NCP, as a function of momentum transfer q in ϵ-phase $ZrD_{2.00}$ at 290 K.

Figure 4.16 σ (circles) as a function of momentum transfer q in ϵ-phase $ZrD_{2.00}$ at 290 K. The horizontal line at $\sigma = 4.96$ is the result obtained from the numerical simulation.

Figure 4.17 The measured NCP for $NbH_{0.95}$ in the momentum transfer range 35.4 - 66.4 $Å^{-1}$.

Figure 4.18 The measured NCP for $NbH_{0.95}$ in the momentum transfer range 76.6 - 109.9 $Å^{-1}$.

Figure 4.19 The measured NCP for $NbD_{0.98}$ in the momentum transfer range 32.0 -

using $\Theta_D = 400$ K. This figure shows the resulting σ values determined from these simulations against the Debye model fit to the back-scattering data (circles in figure 5.6).

Figure 5.8 A simulation of the eVS data for the summed data of the ten back-scattering detectors for the measurement at 260.5 K.

Figure 5.9 The crosses show the σ values determined from the symmetrised back-scattering data. The circles are the unsymmetrised data (figure 5.6). The upper solid line shows the Debye fit to the symmetrised data, and the lower solid line is the corresponding fit to the unsymmetrised data. The Debye temperature determined from the fit is 419$\pm$2.7 K as opposed to 401.3 $\pm$ 3.7 K for the unsymmetrised data.

TABLE CAPTIONS

Table 2.1a The instrument calibration parameters.

Table 2.1b The instrument calibration parameters.

Table 2.2 Resolution parameters in y-space for scattering from hydrogen in ZrH_2. The dependence on scattering angle is shown.

Table 2.3a The calibrated σ_E values, the half-width at half-maximum of the Lorentzian resolution contribution in y-space from the analyser foil.

Table 2.3b The calibrated values of ΔE_R, the half-width at half-maximum of the Lorentzian resolution contribution due to the analyser foil.

Table 4.1 The experimentally determined first optic mode energies of H/D in Nb-H and Nb-D systems along the crystallographically distinct (100) and (010) directions. Values of σ have been derived from these assuming that the modes are harmonic (σ_{Ha}) and taking the anharmonicity of these systems into account (σ_{Anh}).

Table 4.2 The H/D concentrations of the four hydride / deuteride samples manufactured at the University of Warwick determined by weight and pressure measurements (see text).

Table 4.3 The results of the analysis of the eVS measurements. The data were y-transformed and the measured neutron Compton profiles were not symmetrised.

Table 4.4 The results of the analysis of the eVS data. The data were y-transformed and the measured neutron Compton profiles were symmetrised to remove final-state effects of order q^{-1}.

Table 4.5 The results of the analysis of the numerical simulations of the Zr-H and Zr-D systems over the low and high angle banks.

DEFINITION OF UNITS

Considering a particle of mass M with a wavenumber k, the kinetic energy is given in Joules as

$$\frac{\hbar^2 k^2}{2M} \tag{1}$$

with $\hbar = 1.054494 \times 10^{-34}$. k is measured in m^{-1} and M is measured in Kg.

Expressing k in $Å^{-1}$ and M in atomic mass units (amu), where 1 amu$= 1.66043 \times 10^{-27}$ Kg it follows that the kinetic energy in meV is given by

$$\omega = \frac{\hbar^2 k^2}{2M} \tag{2}$$

with $\hbar = 2.04458(\text{meV amu})^{1/2} Å^{-1}$.

CHAPTER 1

Deep inelastic neutron scattering

1.1 INTRODUCTION

In the past two decades, the development of pulsed neutron sources, for example the ISIS spallation source [1, 2], has opened up new fields of research. The large flux of epithermal neutrons that has become available ($E > 500$meV) has made possible the direct measurement of atomic momentum distributions in condensed matter by deep inelastic neutron scattering (DINS). Pulsed neutron sources provide much greater flux at these energies than the available reactor-based sources [2] and so the dynamic structure factor $S(q,\omega)$ can be measured in regions of (q,ω) space unattainable with reactor-based sources. At high momentum transfers, the scattering of neutrons from nuclei in condensed matter systems becomes incoherent and approaches the impulse-approximation limit of free-atom scattering, Doppler-broadened by the distribution of initial atom velocities. In this scattering regime, DINS aims to determine the kinetic energy of the scatterer.

DINS is a technique, analogous in many ways to photon Compton scattering [3], that has arisen with the development of pulsed neutron sources. It is the only neutron scattering technique that takes full advantage of the epithermal neutrons available at such sources, and is not feasible with conventional reactor-based sources. The bulk of the theory behind DINS has been understood for some time. Indeed, DINS takes its name from high-energy physics. For example, the observation of Bjorken scaling, the asymptotic property

$$\lim_{q\to\infty} S(q,\omega) = \delta(\omega - \omega_r), \tag{3}$$

in deep inelastic lepton-nucleon scattering, is regarded as direct evidence for the existence of quarks ([4] and references 36-43 therein).

Deviations from the impulse approximation at finite momentum transfers need to be

considered in the interpretation of DINS data. The main aim of this thesis is to demonstrate for a number of systems that for the current statistical accuracy available on the Electron-volt Spectrometer (eVS), deviations from the impulse approximation at the momentum transfers available with the ISIS spallation source are small enough to be dealt with by a simple correction procedure.

1.2 GENERAL NEUTRON SCATTERING THEORY

This section introduces basic neutron scattering theory and the extension of this to DINS. A concise introduction to neutron scattering theory is given in the doctoral thesis by M. P. Paoli [21], from which equations 4 to 8 are borrowed. More detail on general neutron scattering theory can be found in books by Lovesey [5] and Squires [6].

1.2.1 The double-differential scattering cross-section

The basic quantity measured in a neutron scattering experiment is the partial differential scattering cross-section. This is defined as the number of neutrons, with a fixed incident energy, scattered per second into a small solid angle $d\Omega$ and with a final energy in a narrow band between ω and $\omega + d\omega$, divided by the incident neutron flux, solid angle $d\Omega$ and the energy range $d\omega$. From this definition,

$$\frac{d^2\sigma}{d\omega d\Omega} = \frac{1}{\Phi}\frac{1}{d\Omega}\delta(\omega_i - \omega_f + \omega_\lambda - \omega_{\lambda'})W_{\mathbf{k}_i\sigma_i\lambda\rightarrow\mathbf{k}_f\sigma_f\lambda'} \tag{4}$$

where Φ is the incident flux, $\mathbf{k}$ is the neutron wave-vector, ω is the neutron energy and σ denotes the spin state of the neutron with the subscripts i and f denoting initial and final states respectively. The δ-function ensures the conservation of energy.

The term $W_{\mathbf{k}_i\sigma_i\lambda\rightarrow\mathbf{k}_f\sigma_f\lambda'}$ is the transition rate per second from the state $\mathbf{k}_i\sigma_i\lambda$ to the state $\mathbf{k}_f\sigma_f\lambda'$, summed over all possible $\mathbf{k}_f$ values in $d\Omega$. It can be calculated from Fermi's Golden Rule,

$$W_{\mathbf{k}_i\sigma_i\lambda\rightarrow\mathbf{k}_f\sigma_f\lambda'} = \frac{2\pi}{\hbar}\rho\mathbf{k}_f|\langle\mathbf{k}_f\sigma_f\lambda'|V|\mathbf{k}_i\sigma_i\lambda\rangle|^2 \tag{5}$$

with

$$\langle\mathbf{k}_f\sigma_f\lambda'|V|\mathbf{k}_i\sigma_i\lambda\rangle = \int\int \phi^*_{\mathbf{k}_f}\chi^*_{\lambda'}V\phi_{\mathbf{k}_i}\chi_\lambda d\mathbf{R}d\mathbf{r} \tag{6}$$

and

$$d\mathbf{R} = d\mathbf{R}_1 d\mathbf{R}_2 ... d\mathbf{R}_N \tag{7}$$

where $\rho_{\mathbf{k}_f}$ is the number of momentum states in $d\Omega$ per unit energy range for the neutron in state $\mathbf{k}_f$,

$d\mathbf{R}_j$ is the element of volume for the jth nucleus,

$d\mathbf{r}$ is the element of volume for the neutron

V is the interaction potential between the neutron and the target nuclei,

$\phi_{\mathbf{k}}$ is the wave function for the neutron,

and χ_λ is the wave function of the target nuclei.

Substituting equation 5 into equation 4 gives

$$\frac{d^2\sigma}{d\omega d\Omega} = \frac{k_f}{k_i}\frac{m}{2\pi\hbar^2}|\langle \mathbf{k}_f \sigma_f \lambda' | V | \mathbf{k}_i \sigma_i \lambda \rangle|^2 \delta(\omega_i - \omega_f + \omega_\lambda - \omega_{\lambda'}) \tag{8}$$

Using the Fermi pseudopotential

$$V(\mathbf{r}) = \frac{2\pi\hbar^2}{m} b\delta(\mathbf{r} - \mathbf{R}) \tag{9}$$

where b is the scattering length for the nucleus which is dependent on the nuclear isotope and spin, equation 8 can be evaluated. In general, b is complex, with the imaginary part corresponding to absorption. For eVS, the incident beam is unpolarised, so both neutron spin states are equally probable, thus removing the dependence on spin in the above equations. Substituting equation 9 into equation 8, averaging over the initial target state and summing over all possible final states λ gives

$$\frac{d^2\sigma}{d\omega d\Omega} = \frac{\sigma_T}{4\pi}\frac{k_f}{k_i} S(q,\omega), \tag{10}$$

where σ_T is the total scattering cross-section, ω is the energy transfer and $S(q,\omega)$ is the dynamic structure factor given by

$$S(q,\omega) = \frac{1}{2\pi}\int_{-\infty}^{\infty} \exp(-i\omega t) F(q,t) dt \tag{11}$$

where the correlation function

$$F(q,t) = \frac{1}{N}\sum_{i,j=1}^{N} \langle \exp[-i\mathbf{q}\cdot\mathbf{r}_i(0)] \exp[i\mathbf{q}\cdot\mathbf{r}_j(t)] \rangle \tag{12}$$

$\mathbf{r}_j(t)$ is the Heisenberg position operator for the jth atom and the angular brackets denote a thermodynamic average.

1.2.2 Scattering from a harmonic oscillator

The scattering function for a quantum harmonic oscillator can be calculated from equations 10, 11 and 12, and is

$$S(q,\omega) = \sum_n \exp(-2W(\mathbf{q})) \exp\left(\frac{n\omega_0}{2T}\right) I_n(y)\delta(\omega - n\omega_0) \tag{13}$$

where $\exp(-2W(\mathbf{q}))$ is the Debye-Waller factor and $W(q)$ is given by

$$W(\mathbf{q}) = \frac{\hbar^2 q^2}{4M\omega} \coth\left(\frac{\omega}{2T}\right), \tag{14}$$

ω is the energy transfer and $n\omega_0$ is the energy transferred to the oscillator (positive if $n > 0$). $I_n(y)$ is a Bessel function of the first kind whose argument y is given by

$$y = \frac{\hbar^2 q^2}{2M\omega_0 \sinh(\frac{\omega_0}{2T})} \tag{15}$$

where ω_0 is the fundamental energy of the oscillator, M is the mass of the particle. For $\omega_0 \gg T$ and $y \ll 1$ the Bessel function can be approximated as

$$I_n(y) = \frac{1}{n!}\left(\frac{y}{2}\right)^n. \tag{16}$$

Later on, the expression above for the Debye-Waller factor will be used in a determination of the vibrational density of states of hydrogen in ZrH_2.

1.2.3 The incoherent approximation

The incoherent approximation can be applied to simplify the above two equations. In DINS, since $q \gg 2\pi/d$, where d is the interatomic spacing, the $i \neq j$ terms in equation 12 can be neglected and the correlation function is then given by

$$F(q,t) = \langle \exp[-i\mathbf{q}\cdot\mathbf{r}(0)] \exp[i\mathbf{q}\cdot\mathbf{r}(t)] \rangle. \tag{17}$$

where $\mathbf{r}(t)$ denotes the position of one particular atom. Equation 17 neglects interatomic interference effects and regards each atom as scattering independently of the

others. This is demonstrated in figure 1.1. Two atoms A and B are shown. At some time t atom B is at position $\mathbf{r}_j(t)$, but $\mathbf{r}_j(t) - \mathbf{r}_j(0)$ indicated by BC in the figure is much less than the separation between the two atoms. The term $\mathbf{q} \cdot (\mathbf{r}_j(t) - \mathbf{r}_i(0))$ will always be much greater than 2π. For example, for a typical q value of 100 Å^{-1}, and for neighbouring atoms say 3 Å apart, the value inside the exponential will be 300. Variations about the equilibrium position of atom j will cause this value to fluctuate and taking the thermodynamical average of the exponent will give zero. It is important to remember, however, that although $F(q,t)$ depends only on the position of the scattering atom, the interatomic forces due to the presence of the other atoms modify $F(q,t)$ and hence modify the dynamic structure factor $S(q,\omega)$.

1.2.4 The impulse approximation

The impulse approximation arises by neglecting interactions in the final state. Making the further assumption that the momentum transferred to the struck atom is so great that it recoils as a free particle, leads to the impulse approximation, a helpful derivation of which is given by Sears [4].

For a classical system, equation 17 can be expressed [4] as

$$F(q,t) = \langle \exp[i\mathbf{q} \cdot \{\mathbf{r}(t) - \mathbf{r}(0)\}] \rangle \tag{18}$$

$$= \langle \exp[i\mathbf{q} \cdot \int_0^t \mathbf{v}(t')dt'] \rangle \tag{19}$$

where $\mathbf{v} = d\mathbf{r}/dt$ is the velocity of the scattering atom. If the interatomic forces are velocity-independent [7], it can be expressed as

$$F(q,t) = \exp(i\omega_r t)\langle \mathcal{T} \exp[i\mathbf{q} \cdot \int_0^t \mathbf{v}(t')dt'] \rangle \tag{20}$$

where $\mathcal{T}$ is a time-ordering operator. Taking the limit as $q \to \infty$,

$$\lim_{q\to\infty} F(q,t) = \int_{-\infty}^{\infty} n(\mathbf{p}) \exp[i(\omega_r + \frac{\mathbf{q}}{M} \cdot \mathbf{p})t]d\mathbf{p} \tag{21}$$

and so

$$\lim_{q\to\infty} S(q,\omega) = \int_{-\infty}^{\infty} n(\mathbf{p})\delta(\omega - \omega_r - \frac{\mathbf{q}}{M} \cdot \mathbf{p})d\mathbf{p} = S_{IA}(q,\omega) \tag{22}$$

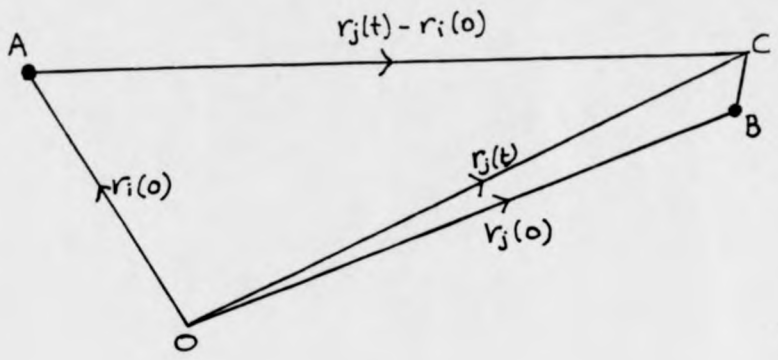

Figure 1.1 The incoherent approximation. The term $\mathbf{q} \cdot [\mathbf{r}_j(t) - \mathbf{r}_j(0)]$ will always be much greater than 2π (see text) and so $\langle \exp(\mathbf{q} \cdot [\mathbf{r}_j(t) - \mathbf{r}_j(0)]) \rangle$ will average out to zero. Hence terms with $i \neq j$ in equation 10 can be neglected.

where M is the atomic mass and $\mathbf{q}$ is the momentum transfer, ω is the energy transfer and ω_r is the energy transfer for recoil scattering. The impulse approximation is made by making the approximation $S(q,\omega) \simeq S_{IA}(q,\omega)$. Replacing ω and ω_r with the values for a classical system, equation 23 is obtained [8, 9, 5],

$$S_{IA}(\mathbf{q},\omega) = \int_{-\infty}^{\infty} n(\mathbf{p})\delta\left(\omega - \frac{(\mathbf{p}+\mathbf{q})^2}{2M} + \frac{p^2}{2M}\right) d\mathbf{p}. \tag{23}$$

Sears [10, 11, 12] and Weinstein et al [10] have both demonstrated that for a smooth scattering potential, the IA is reached asymptotically as the momentum transfer q tends to infinity. A number of criteria have been proposed for the minimum momentum transfer at which the IA is valid [8]. This is typically when the incident energy of a neutron is significantly greater than the maximum energy available within the response spectrum of the target. The momentum distribution, $n(\mathbf{p})$, can then be extracted [13] in a procedure analogous to that used in Compton scattering of photons by electrons [3].

Taking the z-axis along $\mathbf{q}$, equation 23 simplifies to

$$S_{IA}(\mathbf{q},\omega) = \frac{M}{q} J(y) \tag{24}$$

where

$$y = \frac{M}{q}\left(\omega - \frac{q^2}{2M}\right) \tag{25}$$

and

$$J(y) = \int_{-\infty}^{\infty} n(p_x, p_y, y) dp_x dp_y \tag{26}$$

is the neutron Compton profile (NCP), the one-dimensional projection of $n(\mathbf{p})$ along the direction of $\mathbf{q}$, also known as the longitudinal momentum distribution. Figure 1.2 shows how $J(y)$ is obtained from $n(\mathbf{p})$. $J(y)$ is an integration over a plane perpendicular to $\mathbf{q}$ at a distance y from the origin of momentum space. In the illustration, $n(\mathbf{p})$ is that of a collection of non-interacting fermions (chosen as an example), and is constant for $p < p_f$, zero for $p > p_f$, where p_f is the momentum of the maximum occupied state. The neutron Compton profile is then an inverted parabola centred at $y = 0$.

The properties of $S_{IA}(q,\omega)$ which follow from equations 24 to 26 are known as y-scaling, and y is sometimes referred to as the West scaling variable [14] who first

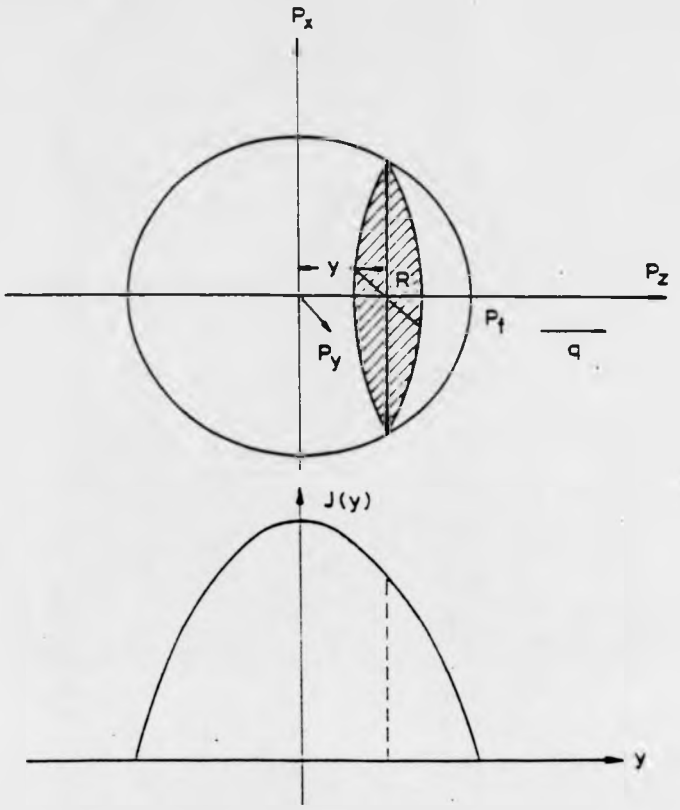

Figure 1.2 Illustration of how the neutron Compton profile $J(y)$ is calculated. $J(y)$ is an integration of $n(\mathbf{p})$ over a plane R perpendicular to $\mathbf{q}$ at a distance y from the origin of atomic momentum space (known as y-space). In the simple illustration, $n(\mathbf{p})$ is a solid sphere and $J(y)$ is the area of intersection of the sphere and the plane R.

emphasised y-scaling of the dynamic structure factor in electron scattering. For a spherically Gaussian momentum distribution $n(\mathrm{p})$, given by equation 34, it can be shown that $S_{IA}(q,\omega)$ is a Gaussian of variance σ_q centred about the recoil energy ω_r with its width scaling as q/M:

$$\sigma_q = \hbar^2 q\sigma/M. \tag{27}$$

The degree to which the measured $S(q,\omega)$ obeys this scaling law [4] is a measure of the validity of the IA.

1.2.5 $J(y)$ for an ideal gas

For an ideal gas of particles mass M at a temperature T (meV) the momentum distribution is given by

$$n(p) = \left(\frac{1}{2\pi MT}\right)^{3/2} \exp\left(\frac{-p^2}{2\pi MT}\right) \tag{28}$$

and so in the impulse approximation, the neutron Compton profile is

$$J(y) = \left(\frac{1}{2MT}\right)^{1/2} \exp\left(\frac{-y^2}{2MT}\right). \tag{29}$$

1.2.6 $J(y)$ in an isotropic harmonic system

The vibrational energy of a particle in a harmonic lattice is

$$E_{vib} = \int_0^\infty \omega \left[\frac{1}{2} + \frac{1}{\exp \omega/k_B T - 1}\right] g(\omega) d\omega \tag{30}$$

in meV where ω is the vibrational energy, k_B is Boltzmann's constant (0.08617 meVK^{-1}), T is the temperature in K and $g(\omega)$ the density of states. By making the substitution $g(\omega) = 3\omega^2/\omega_D^3$ for a Debye density of states, it is found that

$$E_{vib} = \frac{9}{8}\omega_D + 9\omega_D \left(\frac{T}{\Theta_D}\right)^4 \int_0^{\Theta_D/T} \frac{x^3}{\exp x - 1} dx, \tag{31}$$

$\Theta_D = \omega_D/k_B$ is the Debye characteristic temperature and ω_D is the cut-off energy. The mean kinetic energy is one-half of the total vibrational energy for a harmonic system, and using $E_{kin} = \hbar^2\sigma^2/2M$ and also the fact that the $0 \rightarrow 1$ transition energy is twice E_{vib} it follows that for the variance of the NCP

$$\sigma^2(T) = \frac{m}{\hbar^2}\left[\frac{3}{8}\omega_D + 3\omega_D \left(\frac{T}{\Theta_D}\right)^4 \int_0^{\Theta_D/T} \frac{x^3}{\exp x - 1}\right] \tag{32}$$

where $\hbar$ is 2.04458 (meV amu)$^{1/2}$Å^{-1} This can be expressed more succinctly as

$$\sigma^2(T) = \frac{m}{2\hbar^2}\int_0^{\omega_D}\frac{3x^3}{\omega_D^3}\coth\left(\frac{x}{2T}\right)dx. \tag{33}$$

For an isotropic harmonic system, $n(p)$ is of the form

$$n(p) = \frac{1}{(2\pi\sigma^2)^{3/2}}\exp\left(\frac{-p^2}{2\sigma^2}\right) \tag{34}$$

where $\sigma = MT^*$.

The atomic momentum distribution is identical to that of a free gas, except that the temperature is replaced by an effective temperature given by $\hbar^2\sigma^2 = MT^*$ and so from equation 26,

$$J(y) = \frac{1}{(2\pi MT^*)^{1/2}}\exp\left(\frac{-y^2}{2MT^*}\right) \tag{35}$$

where T^* is the effective temperature (in meV).

$$T^* = \frac{1}{2}\int_0^{\infty}\omega g(\omega)\coth\left(\frac{\omega}{2T}\right)d\omega \tag{36}$$

and $g(\omega)$ is the phonon density of states. E is simply

$$E = \frac{3}{2}T^*. \tag{37}$$

1.2.7 Final state effects

Deviations of the dynamic structure factor from $S_{IA}(q,\omega)$ occur at finite values of the momentum transfer q. Those arising as a consequence of the scattered neutron interacting with neighbouring atoms (deviating from plane-wave behaviour) are known as final-state effects [15]. The consequence of final-state effects is to introduce an asymmetry into the neutron Compton profile and to shift the peak position to a negative value of y in momentum space. It is important to measure the scale of these deviations, to determine whether they need to be taken into account in deriving σ from $J_m(y)$, the measured neutron Compton profile ($J_m(y)$ is defined in section 2.6.3.1). For example, the presence of final-state effects is believed to be the reason that the Bose condensate has not yet been observed in superfluid ^{4}He [16].

In order to take into account final state interactions, the dynamic structure factor at finite momentum transfers is commonly expressed as a convolution of $S_{IA}(q,\omega)$, the impulse approximation result, with a function $R(q,\omega)$. Sears [4] defines a quantity $\tilde{R}(q,t)$ where

$$F(q,\omega) = \tilde{R}(q,t)F_{\infty}(q,t) \tag{38}$$

and so from equation 11

$$S(q,\omega) = \int_{-\infty}^{\infty} R(q,\omega')S_{\infty}(q,\omega-\omega')d\omega' \tag{39}$$

where $R(q,\omega)$ is the Fourier transform of $\tilde{R}(q,t)$:

$$R(q,\omega) = \frac{1}{2\pi}\int_{\infty}^{\infty} \exp(-i\omega)\tilde{R}(q,t)dt. \tag{40}$$

In the limit $q \rightarrow \infty$, $R(q,\omega) = \delta(\omega)$ and so final state effects disappear, as expected in the IA. However, at finite momentum transfers, final state effects are present as a broadening of the neutron Compton profile $J(y)$. By expanding $S(q,\omega)$ in a Taylor series :

$$S(q,\omega) = \sum_{0}^{\infty} \frac{(-1)^n}{n!} R_n(q)\frac{\partial^n}{\partial\omega^n}S_{\infty}(q,\omega) \tag{41}$$

where

$$R_n(q) = \int_{-\infty}^{\infty} \omega^n R(q,\omega)d\omega. \tag{42}$$

This and equation 24 lead to the result

$$S(q,\omega) = \frac{m}{q}\sum_{n=0}^{\infty}(-1)^n A_n(q)\frac{d^n J(y)}{dy^n} \tag{43}$$

where

$$A_n(q) = \frac{1}{n!}(m/q)^n R_n(q). \tag{44}$$

$A_0(q) = 1$, $A_1(q) = 0$, $A_2(q) = 0$, and for $n = 3,5,7...$, $A_n(q)$ is of order $O(q^{-1})$, and for $n = 4,6,8...$, $A_n(q)$ is of order $O(q^{-2})$. Note especially that

$$A_3(q) = m\langle\Delta V\rangle/36\hbar^2 q \tag{45}$$

and

$$A_4(q) = m^2\langle \mathbf{F}^2\rangle/72\hbar^4 q \tag{46}$$

where $\langle \mathbf{F}^2 \rangle$ is the mean-square force on the target particle and V is the total potential energy of the system.

Expanding the first three terms of $S(q,\omega)$ gives

$$S(q,\omega) = \frac{m}{q}\left[J(y) - A_3(q)\frac{d^3J(y)}{dy^3} + A_4(q)\frac{d^4J(y)}{dy^4}\right] \tag{47}$$

The second term in the square brackets is asymmetric in y and is of order q^{-1}, and the third term is symmetric in y and of order q^{-2}.

1.2.8 Initial state effects and the Stringari formulation

Deviations from the impulse approximation have been predicted to arise due to the quantum nature of the initial state. In the impulse approximation, a classical picture is used and it is assumed that in the initial state the target atoms have a distribution of energies. In a quantum system, although a state will have a distribution of momenta, it will have one fixed energy, which is the eigenvalue of that state. The Stringari formulation of the impulse approximation arises naturally from this consideration [17, 8, 9], taking into account the bound state of the atom.

It has been shown by numerical calculation [9] that at temperatures below $T \sim 0.3\Theta_D$, where Θ_D is the Debye temperature of the system being studied, the Stringari form of the impulse approximation describes the neutron Compton profile better at finite q than does the impulse approximation.

The Stringari formulation [17] is obtained from the IA by replacing the $\mathbf{p}^2/2M$ term with the mean kinetic energy with the result

$$S_s(\mathbf{q},\omega) = \int_{-\infty}^{\infty} n(\mathbf{p})\delta\left(\omega - \frac{(\mathbf{p}+\mathbf{q})^2}{2M} + E_{kin}\right)d\mathbf{p}. \tag{48}$$

where E_{kin} is the mean kinetic energy. For an isotropic momentum distribution, it can be shown [17] that

$$qS_s(\mathbf{q},\omega) = 2\pi M\int_{|y_1|}^{\infty} pn(p)dp \tag{49}$$

where

$$y_1 = \sqrt{2M(\omega + E_{kin})} - q \tag{50}$$

is the scaling variable (c.f. the variable y for the IA). This predicts a negative shift of E in the peak energy of $S_s(q,\omega)$ from the IA value of $\hbar^2q^2/2M$ and $S_s(q,\omega)$ is asymmetrical in the variable $(\omega - \omega_R)$. It should be noted that both the West and the Stringari scaling variables lead to $J(y)$ which tend to the IA result at large q.

1.3 SUMMARY

In this chapter, an understanding of the way DINS reveals the momentum distribution of the system under study has been developed. The concepts of y and $y1$-scaling have been introduced. In the next chapter, the instrumental technique is discussed, and the calibration, resolution determination and data analysis on eVS are explained in detail. In chapter 3, eVS measurements of ZrH_2 are compared to exact numerical simulations based on the measured vibrational density of states with the aim of observing deviations from the impulse approximation. In chapter 4, eVS measurements of NbH, NbD, ZrH_2 and ZrD_2 are compared to inelastic neutron spectroscopy measurements and again to simulations based on the measured vibrational density of states. The isotope effects in the corresponding H/D systems are also studied. In chapter 5, measurements of ^{7}Li in natural Li metal are studied, whilst in chapter 6, further developments of the eVS are examined.

CHAPTER 2

Epithermal Neutron Spectroscopy

2.1 INTRODUCTION

This chapter introduces the technique of epithermal neutron spectroscopy and the operation and data analysis on the Electron-volt Spectrometer. Section 2.2 reviews the variety of systems that have been studied by DINS. Section 2.3 discusses neutron sources and the fact that only the new generation of pulsed neutron sources can provide the high flux of epithermal neutrons required to perform DINS experiments, whilst section 2.4 discusses the different experimental techniques of electron-volt neutron spectroscopy. The advantages of choosing to develop an inverse geometry spectrometer for high q studies is explained. In section 2.5, the resolution of inverse and direct geometry time-of-flight spectrometers is discussed, with nuclear resonant absorbers discussed in section 2.6. Section 2.7 introduces the eVS spectrometer in detail starting with the determination of the neutron Compton profile $J(y)$ from the experimental data, and then discussing the instrument calibration, instrument resolution and data analysis.

An example of the regions of q,ω space accessible with DINS on eVS, an inverse geometry spectrometer, is shown in figure 2.1. These calculations were performed for scattering from hydrogen and for a final scattered neutron energy of 4922 meV (gold analyser foil). The (q,ω) scans for the three banks of detectors are referred to as banks A (36 to 44 °), B (46 to 54 °) and C (57 to 66 °) and are represented by the three pairs of curves marked A, B and C in the figure. The left-hand curve of each pair corresponds to the (q,ω) scan for the lowest angle detector in the bank, and the right-hand curve corresponds to the highest angle detector. The central dashed line is the recoil line for hydrogen and the two either side mark where $S(q,\omega)$ is half of its maximum value; the system chosen for this demonstration is ZrH_2 for which $\sigma = 4.18$ Å, according to results presented in chapter 4. The minimum value of q for this set-

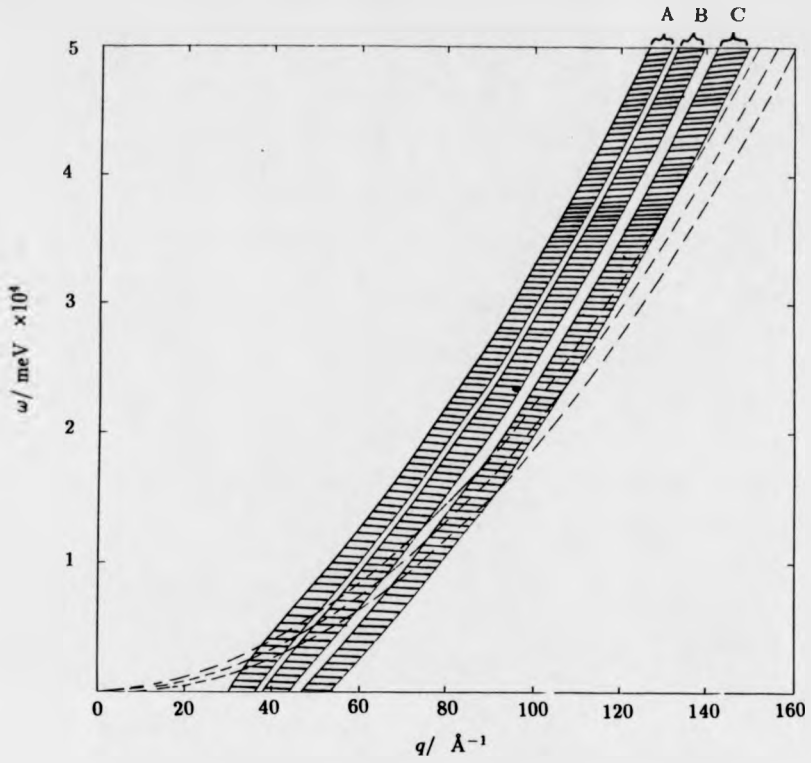

Figure 2.1 Detector scans on eVS through (q,ω) space. For the experiments described in this thesis, the eVS had forty detectors at forward scattering angles. Thirty of these were at angles useful for hydrogen scattering, which are considered for convenience grouped together in three banks of detectors 36° to 44° (bank A), 46° to 54° (bank B) and 57° to 66° (bank C). Each detector scan for each bank lies in the shaded region *A B* or *C* marked on the figure. The dashed curves represent the peak position and HWHM of $S(q,\omega)$ in the case of scattering from ZrH_2.

up is approximately 35 $Å^{-1}$. This diagram demonstrates how the constant θ scans through $S(q,\omega)$ spans broader energy-transfers as the scattering angle increases, and therefore becomes broader in time-of-flight. This improves the effective resolution with increasing scattering angle, as will be shown in section 2.7.

2.2 DINS APPLICATIONS

A review of measurements made in 1990 and 1991 on eVS has been made by Evans et al [18]. Some systems studied by DINS are discussed below as they demonstrate some of the important aspects of DINS.

2.2.1 $KHCO_3$

The hydrogen-bond potential parallel to the bond in $KHCO_3$ is believed to be a double-well potential, as is the potential for H trapped on substitutional Ti atoms in $Nb(TiH)_2$ [19]. Modelling the momentum distribution of a proton trapped in a potential of two splined parabola separated a distance $\pm$a from the origin gives a Gaussian of variance $M\omega_0$ modulated by a cosine function $\cos(2\pi x/a)$, as shown in figure 2.2. The origin in the figure is equidistant to the two minima. Two primary maxima exist at a distance $p/\hbar = \pi/a$ from the origin, with successive maxima further out. An experiment to look for this effect is currently planned for 1993.

2.2.2 Pyrolytic graphite

Pyrolytic graphite has a hexagonal layered structure. The bonding between carbon atoms within a layer is strong, but the bonding between atoms in adjacent layers is much weaker. This significant difference in bond strength results in a difference in the mean kinetic energy for vibrational motion parallel and perpendicular to the planes. Paoli et al [20] measured the mean kinetic energy parallel and perpendicular to the hexagonal layers using the eVS spectrometer at ISIS, and compared their results to mean kinetic energies derived from a phonon density-of-states model. The comparison was in agreement perpendicular to the layers but at variance parallel to

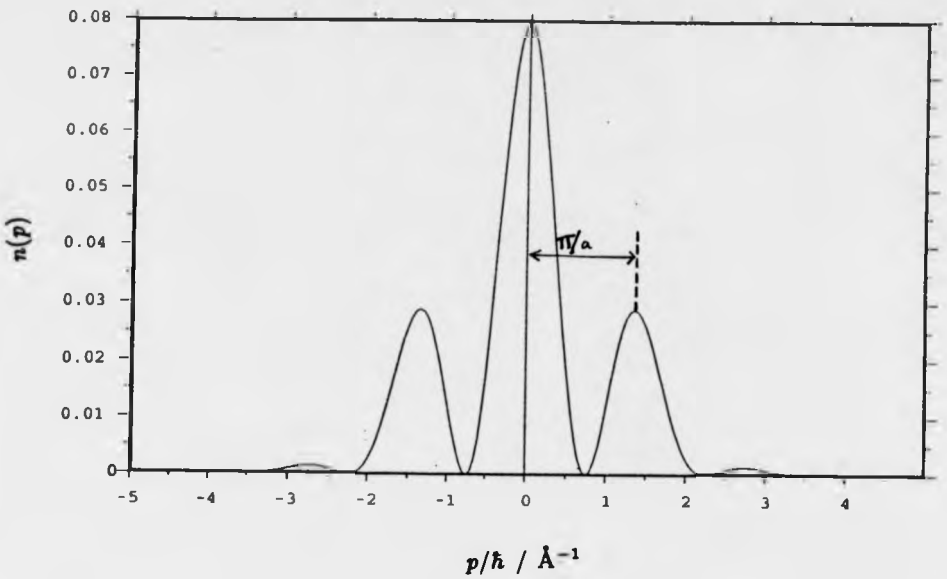

Figure 2.2 Momentum distribution for a particle in a one-dimensional double potential well. The potential is $V(x) \propto (x-a)^2 + (x+a)^2$. The first two maxima occur at $p/\hbar = \pi/a$. The momentum distribution shown is for $a = 1.8\mathring{A}$.

them, and suggested that the vibrational density of states in the hexagonal plane extends to higher energies than previously thought. The NCP is a directional measurement and so it is possible to measure anisotropy in the momentum distribution in single crystals. (the longitudinal momentum distribution is measured along the scattering vector q.) Pyrolytic graphite is one such system that exhibits strong vibrational anisotropy, and DINS measurements have been made on this system [20]. In principal, it is possible to reconstruct a three-dimensional momentum distribution from many one-dimensional distributions in different directions in a single crystal. Such reconstructions have been achieved with photon Compton scattering ([22] and references therein), and two-dimensional reconstructions have been carried out with DINS. This is obviously an interesting area for further development.

2.2.3 Liquid and solid helium

It was proposed by Hohenberg and Platzman in 1966 [23] that DINS could be used to measure the momentum distribution of helium atoms in liquid ^{4}He and to detect the presence of a zero-momentum condensate below the superfluid transition temperature T_λ. The condensate fraction appears as a δ-function in the momentum distribution centred on the non-condensate component. Since the development of pulsed neutron sources, many DINS studied have been made in an attempt to observe this in ^{4}He, ^{3}He and their mixtures ([24] and references therein) but the task is made difficult by final-state effects which broaden the measured neutron Compton profile $J_m(y)$. Final-state effects are strong in both superfluid and non-condensate helium because of the very repulsive hard-core He-He potential. The understanding of final-state effects is therefore vital in the interpretation of helium data even at large momentum transfers. A test of the theories of final-state effects is the experimental determination of a consistent value for the Bose condensate fraction in superfluid ^{4}He.

2.2.4 The noble gases

Much work has been done on the liquid and solid noble-gas systems, notably by Peek

and Simmons [25, 26, 27, 28]. For solids for which the amplitude of atomic vibrational motion is comparable to the interatomic spacing, the effects of vibrational anharmonicity may be expected to be large. It is known that Xe, Kr and Ar exhibit considerable differences in such properties as phonon anharmonicity and multi-body contribution to cohesion. Despite these differences, in a recent study [25] it has been shown that for all three solids near their respective triple points, the mean kinetic energy is close to the expected classical equipartition result $(3/2)kT$. This study confirmed the validity of the impulse approximation in determining the single particle kinetic energy from $S(q,\omega)$ for systems of mass as high as xenon.

Peek et al [27] have measured mean kinetic energies in liquid and solid neon over the momentum transfer range 20.0 to 28.0 Å^{-1}. Though they did not correct for final-state effects in their data, they performed some numerical calculations of the magnitude of the first symmetric and first asymmetric term in the Sears' expansion (see chapter 1) and were able to show that for the statistical accuracy of their data, final state effects were small enough to be neglected. It will be shown later in chapters 3 and 4 that for the measurement of momentum distributions of hydrogeneous systems on eVS at the time of the experiments that form the basis of this thesis, final-state effects may be dealt with by a simple correction procedure.

2.2.5 Hydride and deuteride systems

DINS is suited to measuring systems containing hydrogen because of its large incoherent neutron cross-section. Metal hydrides are also of theoretical interest; for example the form of the dynamic structure factor for an array of light particles embedded in a matrix of heavy particles has been calculated by Warner et al [29]. With DINS, signals from each isotopic species in a sample appear centred in time-of-flight at the recoil peak position for the mass concerned. For example, scattering from hydrogen and zirconium yields a hydrogen signal centred at a higher energy transfer than the zirconium peak. For a system like ZrH_2 where the two isotopes differ in mass greatly, the two signals are separated even at low momentum transfers. This is shown in figure 2.3. These are time-

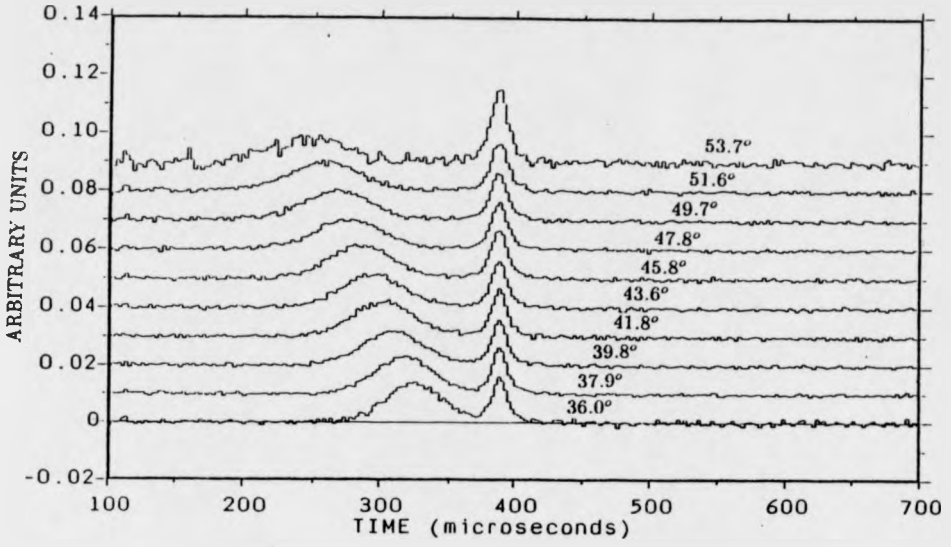

Figure 2.3 A series of time-of-flight difference measurements of ZrH_2 measured on one of the low-angle detector banks on eVS. The broad peak is scattering from hydrogen, while the narrow peak is scattering from aluminium (in the sample holder) and zirconium. Note how the separation of the two peaks and the width of the hydrogen peak both become larger at higher scattering angles.

of-flight spectra for scattering from ZrH_2 over the angular range from 36.0 to 53.7 ° on eVS. The narrow peak at about 390 μs is the signal from the Zr atoms. The hydrogen scattering is the broader signal at lower times of flight. At higher momentum transfers (corresponding to higher scattering angles) the hydrogen signal becomes broader and shifts further away from the Zr peak. This principal of kinematic mass separation is of great benefit in the preliminary data analysis because it aids the separation of the time-of-flight spectra into components corresponding to each isotope present at the sample position.

The isotope effect in metal hydrides and deuterides can be measured. The ratio of the mean kinetic energies of a proton and a deuteron bound by the same potential should be equal to the square-root of the ratio of their masses for a harmonic potential well (and for small x^3 and x^4 perturbations from a harmonic potential, as shall be shown in chapter 4). It is reasonable to expect that the potential binding the H/D atom to the metal lattice is independent of the mass of the bound atom. A deviation from this result would indicate a difference in the hydride and the deuteride potentials. Measurements of this kind therefore provide a useful check on the validity of the IA and on the data analysis.

2.3 NEUTRON SOURCES

The early experiments with neutron sources, soon after the discovery of the neutron sixty-one years ago by Chadwick, were aimed at understanding how the neutron interacted with matter on the nuclear and atomic scales. With the development of Fermi's fission reactor in the forties, and the consequential large increase in neutron flux, instruments could be developed to use neutrons as a probe of condensed matter. Wollan et al [30] demonstrated in the late 1940s that crystallographic techniques could be applied to neutron scattering in the determination of atomic and magnetic structures in condensed matter. Carter et al [31] showed that slow neutrons could be used to study lattice vibrations in condensed matter. They used a filtered beam technique to provide 5 Å neutrons, and examined the energy distribution of the scattered neutrons using a

mechanical chopper. The development of a triple-axis spectrometer by Brockhouse [32] then made possible the study of dispersion relations of crystal vibrations by inelastic neutron scattering.

In the fifties and sixties, thermal neutron fluxes available from reactors improved by several orders of magnitude, as shown in figure 2.4 (from [2]). The available thermal neutron flux from reactor sources leveled off with the building of the ILL source. Neutrons in a reactor are created by fission and must be moderated to thermal energies in order for the reactor to work. This gives a Maxwellian intensity distribution which peaks typically at 25 meV. By changing the temperature of the moderator, the distribution can be shifted to higher or lower energies. By allowing a moderator to come into thermal equilibrium close to the core of a reactor, it can reach temperatures as high as 2000 K and can give operational flux at energies as high as 500 meV. It is prohibitively expensive to build fission reactors to produce higher neutron fluxes because of the heat removal problem. Therefore, accelerator-based neutron spallation sources are necessary if useable neutron flux at epithermal energies are required.

The pulsed neutron source overcomes the problem of heat removal by creating intense but very brief pulses of neutrons, and is therefore only operating typically 1/500th of the time, thus solving the heat removal problem. Negative hydrogen ions are accelerated in a linear accelerator and stripped of their electrons by being passed through a thin foil. The resulting proton pulses are then accelerated further in a synchrotron before being fired into a uranium or tungsten target at energies approaching 1 GeV. Each proton strips off 10 or 20 neutrons in a spallation reaction. The target is surrounded by moderators which converts the short intense pulse of high-energy neutrons into a broader pulse of lower energy neutrons. The moderators used are relatively thin in order to keep the pulse restricted to a timescale of microseconds, and consequently the neutrons are undermoderated which results in a significant epithermal content remaining. Moderators of different temperatures and composition are used according to the requirements of the experiments. The neutron pulses are transmitted down the beam-lines radiating from the target assembly to the experimental areas.

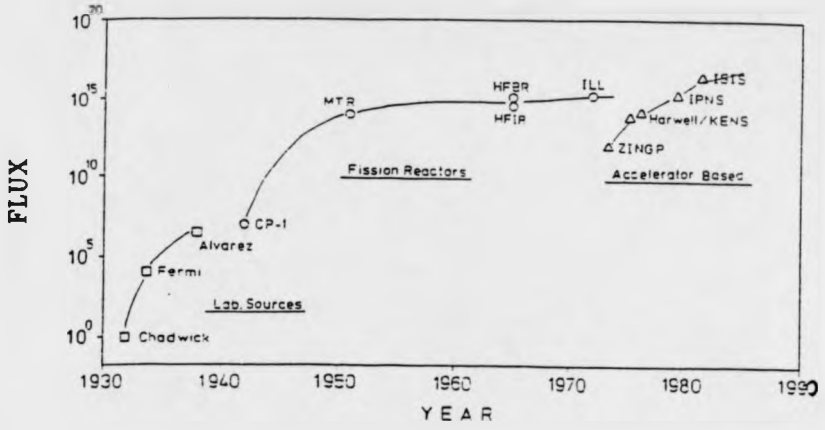

Figure 2.4 The effective thermal neutron flux from laboratory (□), reactor (○) and accelerator based neutron sources (△) (from [2]).

Though the pulsed neutron source is 'on' for only a small fraction of the time, for experiments using thermal neutrons, pulsed sources are comparable to steady-state sources because with a time-of-flight technique a wide range of neutron energies is usually used. The continuous beam of 'white' neutrons available from steady-state fission reactor sources must be monochromated for most experiments, either by using a suitable crystal and selecting a Bragg peak, or by using a mechanical chopper device. Most of the intensity is therefore lost straight away. Figure 2.5 (from [2]) shows the effective neutron fluxes for the cold, thermal and hot sources at the ILL reactor at Grenoble, and the liquid H_2, liquid CH_4 and ambient water (AP) moderators on the pulsed neutron source ISIS at the Rutherford Appleton Laboratory. It is clear that for hot and epithermal neutrons ISIS offers the better fluxes. Pulsed sources are much superior to steady-state reactor sources at providing a high flux of epithermal neutrons.

2.4 EXPERIMENTAL TECHNIQUES IN ELECTRON-VOLT NEUTRON SPECTROSCOPY

The first inelastic scattering measurement of epithermal neutrons was performed in 1968 by Samosvat et al [33] at the IBR-30 pulsed reactor at Dubna. Gold resonant foils were used in the scattered beam to define the final energy of the neutrons; this is an example of an inverse geometry technique that will be described in more detail later. The purpose of this experiment was to test the validity of the IA, but was limited by the low flux of epithermal neutrons available. Since that time, with the development of pulsed neutron sources, the DINS technique has been explored at pulsed neutron sources at the Weapons Nuclear Research (WNR) pulsed neutron facility, Los Alamos, at KENS, Tsukuba, at the Intense Pulsed Neutron Source (IPNS), Argonne National Laboratory, Illinois, and at the Harwell and Rutherford Appleton laboratories in the UK. Work has concentrated on testing the two basic geometries for DINS - direct geometry (DG) and inverse geometry (IG), and on assessing the two detection methods employed. These are the filtered beam spectrometer (FBS) where neutrons of a given energy are detected indirectly by a thin analyser foil made of a material possessing a strong nuclear resonance at that energy, and the resonance detection spectrometer

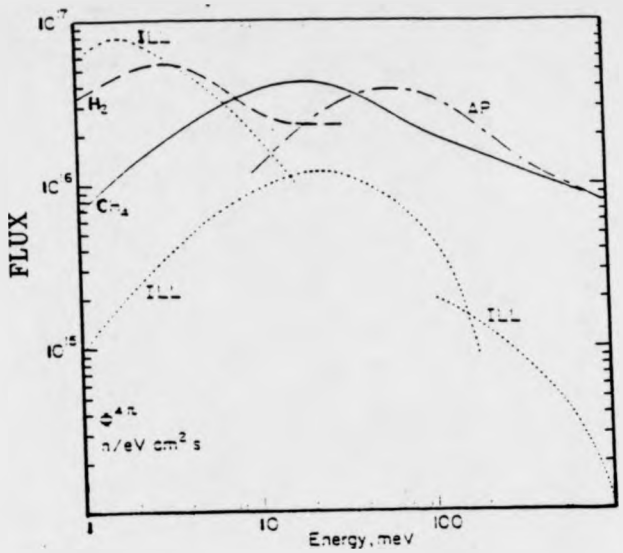

Figure 2.5 The effective neutron flux for the cold, thermal and hot sources on the ILL reactor at Grenoble, (...), and the liquid H_2, liquid methane and ambient water (AP) moderators on the pulsed neutron source ISIS at the Rutherford Appleton Laboratory (from [2]).

(RDS) where scattered neutrons with energies in the region of the resonance are absorbed by an analyser foil in front of a scintillation detector which detects the resulting γ-cascade.

The filtered beam spectrometer has been tested in a series of developmental experiments using a test FBS at the WNR pulsed neutron facility at Los Alamos The results of these experiments are discussed by Newport et al [34] and Brugger et al [35]. The experience gained was of benefit in designing the current FBS at the ISIS spallation source - the electron-volt spectrometer. The RDS (resonance detection system) has been used at the spallation neutron source KENS [36, 37] and at the Harwell laboratory in a collaboration with Oxford University [38].

2.4.1 Direct geometry techniques

In the case of direct geometry, two methods are employed. With both methods, the final energies of the scattered neutrons are calculated from their times-of-flight. The first is an example of a filtered beam method, shown in figures 2.6a and 2.6b. In 2.6a a resonant absorber is placed in the incident beam, and absorbs neutrons within a narrow energy range about the resonant energy E_R. A second measurement is performed, figure 2.6b, with the resonant foil removed from the incident beam. The difference neutron time-of-flight spectra collected with and without the resonant absorber give the sample's response to neutrons of the energy of the resonance. The second method, figure 2.7a, uses a mechanical chopper to monochromate the incident beam. This is the method that has been adopted with HRMECS (High Resolution Medium Energy Chopper Spectrometer) at IPNS. One disadvantage with this technique is that the maximum energy (and hence the maximum momentum transfer for scattering from a given mass) of the incident beam is limited by the rotational speed of the chopper. The chopper must also be phased accurately to the burst-time of the source. HRMECS has very good resolution, and this technique therefore offers some advantages when the limitation on the incident energy and therefore momentum transfer is not a problem.

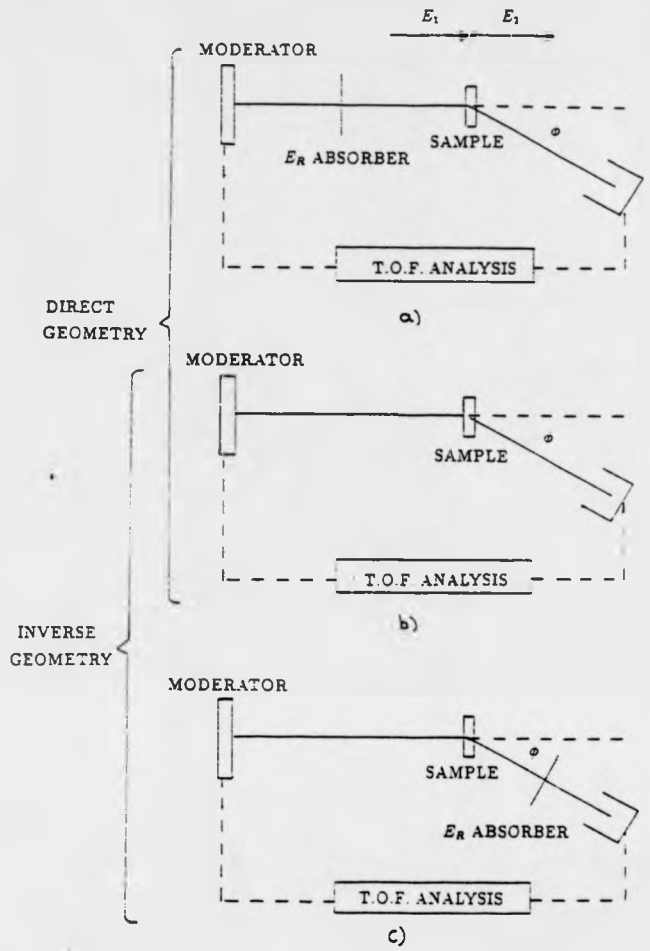

Figure 2.6 Principle of the filtered beam spectrometer in direct (2.6a and 2.6b) and inverse (2.6b and 2.6c) geometries.

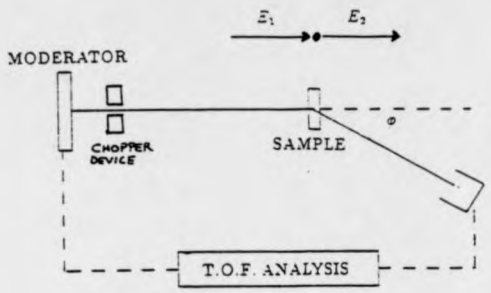

Figure 2.7a Principle of the chopper spectrometer.

2.4.2 Inverse Geometry Techniques

In the inverse geometry case, the final scattered energy of the detected neutrons is fixed and their initial energies are calculated from their times-of-flight. Figures 2.6b and 2.6c show the filtered beam method where a resonant absorber is used in the scattered beam to define the final scattered energy of the neutrons. Figure 2.11 demonstrates this principle on the eVS spectrometer with a sample of ZrH_2. The dashed line is a time-of-flight spectrum at a forward scattering angle with the resonance analyser foil (Au in this case) in the scattered beam spectrum with the foil in the beam. The gold foil absorbs neutrons with an energy in the region of 4922 meV. The solid line is the foil-out spectrum. The normalised difference time-of-flight spectrum shows those neutrons scattered to the foil's resonance energy. The number of neutrons detected in a time bin is the difference of two large numbers, and so the statistical quality of the difference spectra is not as good as when a direct detection system (RDS) is used. A significant advantage, however, is that a first-order background correction is performed in taking the difference.

The principle of the RDS is shown in figure 2.7b. RDS operates in inverse geometry but the FBS detection method can be used in both geometries.

2.5 RESOLUTION OF INVERSE AND DIRECT GEOMETRY SPECTROMETERS

Newport et al [39] state simplified expressions for the component of the resolution of the direct geometry (DG) and inverse geometry (IG) spectrometers arising from the resonance width of the analyser foil as being

$$\left[\frac{\Delta\hbar\omega}{\hbar\omega}\right]_{IG} = \frac{\Delta E_R}{\hbar\omega}\left[1 + \frac{L_{2I}}{L_{1I}}\left(\frac{E_1}{E_R}\right)^{1.5}\right] \tag{51}$$

and

$$\left[\frac{\Delta\hbar\omega}{\hbar\omega}\right]_{DG} = \frac{\Delta E_R}{\hbar\omega}\left[1 + \frac{L_{1D}}{L_{2D}}\left(\frac{E_2}{E_R}\right)^{1.5}\right] \tag{52}$$

where E_R is the resonance energy of the foil, E_1 and E_2 are the incident and scattered neutron energies, and L_1 and L_2 are the primary and secondary flight-paths, with the

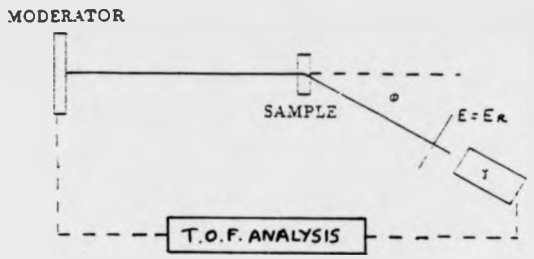

Figure 2.7b Principle of the resonance detector spectrometer. This operates in inverse geometry and uses a scintillation detector (n+γ) to observe the gamma-ray cascade that results when a neutron is absorbed in the vicinity of the strong resonance at $E = E_R$ possessed by the analyser foil.

subscripts I and D referring to the inverse geometry and direct geometry techniques respectively. This is usually the dominant contribution. They also state that equivalent count rates are obtained for IG and DG spectrometers when

$$L_{1D}L_{2D} = L_{1I}L_{2I}. \tag{53}$$

These expressions are useful in comparing the resolutions of the two geometries. Full examinations of resolution functions have been made by a number of authors for direct geometry [35, 38, 40] and for inverse geometry [35, 37]

To have good energy resolution on pulsed neutron sources, it is necessary that in the case of IG, $L_{1I} \gg L_{2I}$ and in the case of DG, $L_{1D} \ll L_{2D}$. The condition for IG is easily satisfied on a pulsed source, but the condition for DG is not so easily satisfied. The minimum value for L_{1D} is constrained to about 6 metres at ISIS by the need for biological shielding around the target, thereby preventing optimisation of resolution. In the IG case, L_{2I} can be minimised. Following the procedure used in reference [39] for comparing the resolution of IG and DG spectrometers, the resolution for eVS has been calculated as a function of energy transfer $\hbar\omega$ and is compared to the resolution of a hypothetical DG machine with an equivalent count rate. The calculation was performed for the case of a gold resonant absorber (E_R = 4922 meV and ΔE_R = 140 meV) and for L_{1I} = 11 m, L_{2I} = 1 m, L_{1D} = 6 m and L_{2D} = 3 m, L_{2D} being determined by the maximum probable distance permitted by the biological shielding about the instrument. These functions are shown in figure 2.8, showing clearly the superior resolution of the IG technique for this given set of conditions. The continuous line represents the resolution for the IG machine, and the dashed line that for the DG machine. Note that the DG resolution function terminates at $\omega = E_R$, indicating this as the maximum energy transfer available for DG. The maximum energy transfer possible with the direct geometry technique is restricted to the resonance energy of the foil but over the range of energy transfer common to both IG and DG methods for each foil, the resolution in the IG case is typically one half that of the direct geometry case. This is a specific example but highlights the problem with the DG technique that the presence of biological shielding around the target imposes on L_{1D}.

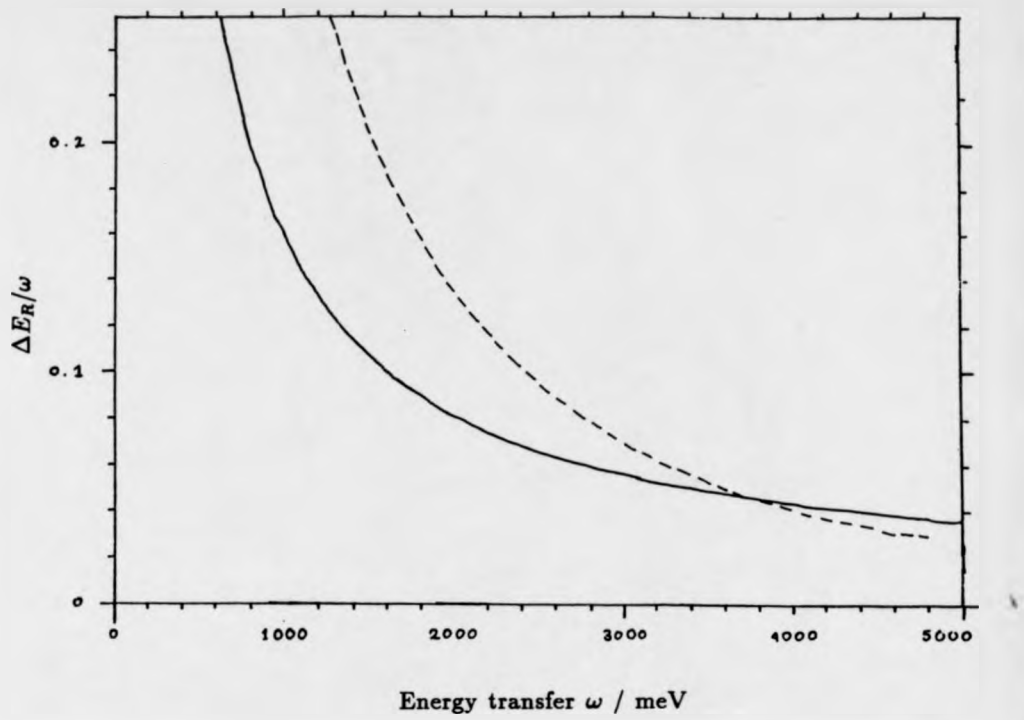

Figure 2.8 The resolution of direct and indirect geometry spectrometers. The solid line is $\Delta E_R/\omega$ for an inverse geometry machine that uses a gold analyser foil ($\Delta E_R \simeq 140$ meV) and has primary and secondary flight paths of 11m and 1m respectively. The broken line is $\Delta E_R/\omega$ for a direct geometry machine with primary and secondary flight paths of 6m and 3m respectively.

In their report, Newport et al [39] discuss the relative sensitivity of the FBS and the RDS and conclude that under certain circumstances the relative statistical errors associated with FBS and RDS measurements can in some circumstances be the same.

Another advantage of the IG spectrometer is that an array of detectors covers q,ω space more effectively than the DG spectrometer. Each point in the time-of-flight spectrum measured with each detector samples q,ω space at a point on a curve defined by the spectrometer geometry, the scattering angle, the primary and secondary flight path lengths, and the resonance energy of the resonant absorber used. There is a set of such curves that characterise the instrument, each one corresponding to a particular detector. The flexibility of the instrument is determined to a large extent by the area of q,ω space that these curves cover. Figures 2.9a and 2.9b show such q,ω scans for the 4922 meV resonance in gold and the 6671 meV resonance in ^{238}U respectively for scattering from hydrogen in ZrH_2 at angles of 20, 40 and 60 degrees for inverse geometry (dashed lines) and direct geometry (solid lines). The three dotted dashed lines in each figure mark the maximum and half-maximum of $S(q,\omega)$ assuming $\sigma = 4.18\text{Å}^{-1}$. The figures demonstrate clearly that for the same scattering angles, inverse geometry reaches higher energy and momentum transfers than direct geometry, and that the discrepancy increases at higher scattering angles. For the study of high-q effects, it is preferable to use the IG technique.

2.6 NUCLEAR RESONANCE ANALYSERS

In the FBS detection system, the nuclear resonance analyser determines the largest contribution to the resolution function. In this section, the form of the transmission of a resonance analyser and how it is effected by variation in thickness and temperature is examined closely. According to the theory of Breit and Wigner, the cross-section for absorption of a neutron by an isolated nucleus at rest is a Lorentzian function of the neutron energy:

$$\sigma(E) = \frac{\sigma_0 \Gamma^2}{\Gamma^2 + (E - E_R)^2} \tag{54}$$

where Γ is the half-width at half-maximum of $\sigma(E)$, E is the energy of the neutron and

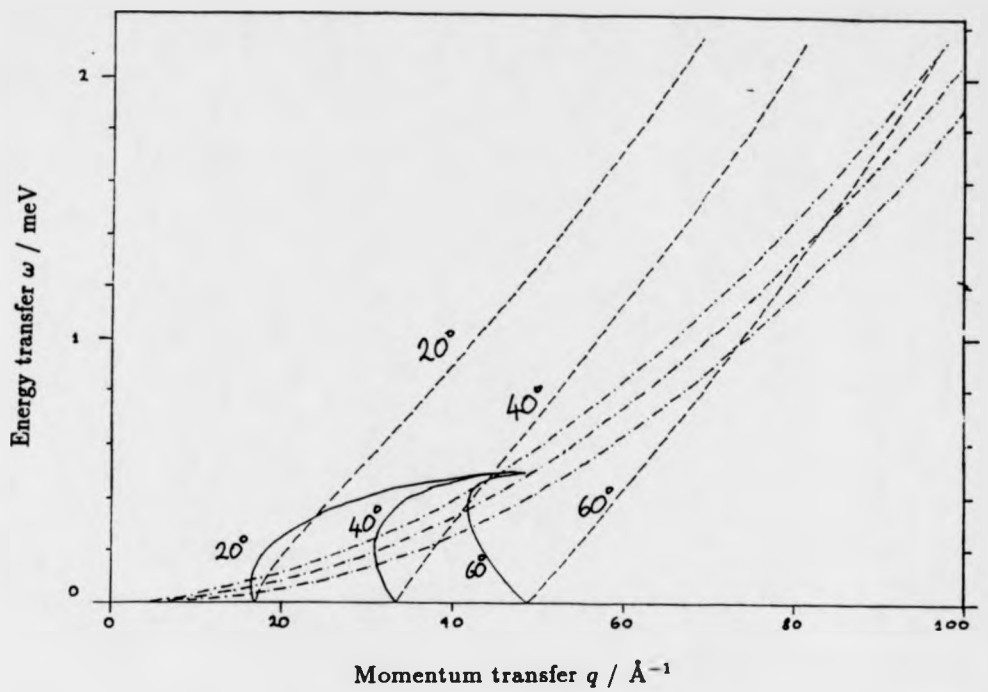

Figure 2.9a Detector scans through (q,ω) space for angles of 20, 40 and 60 ° for scattering from hydrogen and for inverse and direct geometry. The calculations are performed for a gold analyser foil (E_R = 4922 meV and ΔE_R = 140 meV). The DG scans are the three solid lines and the IG scans are the dashed lines. The dotted-dashed lines mark the maximum and the FWHM of $S(\mathbf{q},\omega)$ for hydrogen in ZrH_2 which has a momentum distribution variance of 4.18 Å^{-1}.

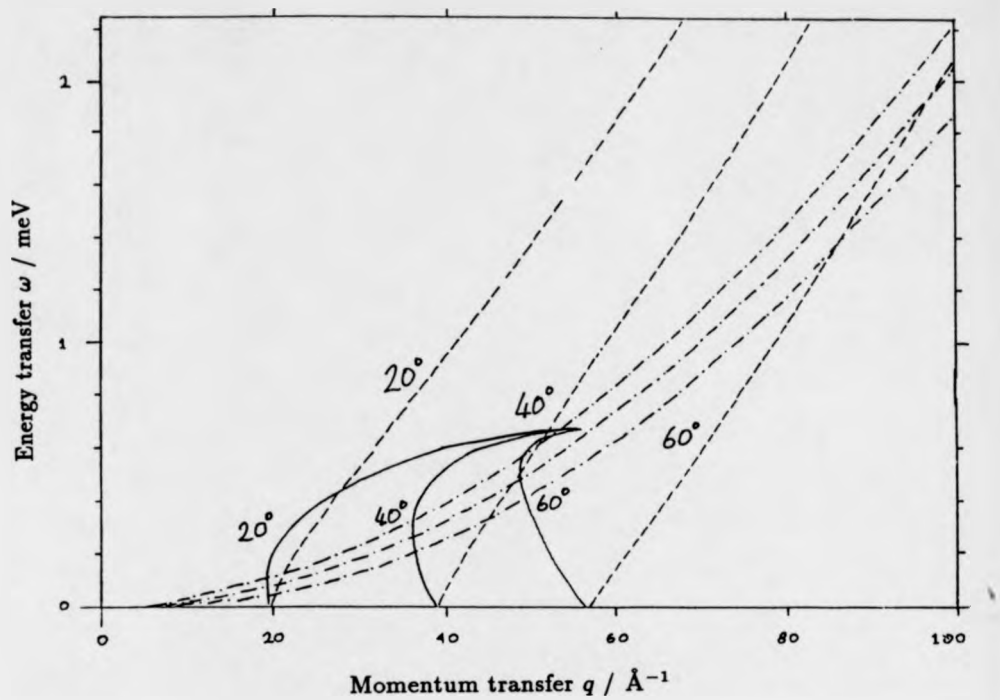

Figure 2.9b Detector scans through (q,ω) space for angles of 20, 40 and 60 ° for scattering from hydrogen and for inverse and direct geometry. The calculations are performed for a uranium analyser foil (E_R = 6671 meV and ΔE_R = 140 meV). The DG scans are the three solid lines and the IG scans are the dashed lines. The dotted-dashed lines mark the maximum and the FWHM of $S(\mathbf{q},\omega)$ for hydrogen in ZrH_2 which has a momentum distribution variance of 4.18 Å^{-1}.

E_R is the resonance energy. Equation 54 is the intrinsic cross-section of the nucleus. The absorption cross-section of the nucleus embedded in a solid is broadened from the isolated nucleus result and becomes less Lorentzian in nature [41] due to the presence of interatomic forces. The Doppler-broadened cross-section has been calculated by Lamb [42] and Nelkin and Parks [43]. For weak binding between atoms, the absorption cross-section is given by

$$\sigma = \sigma_0 \Phi(\zeta, x) \tag{55}$$

where

$$\Phi(\zeta, x) = \frac{\zeta}{2\sqrt{\pi}} \int_{-\infty}^{\infty} dy \frac{\exp -(\zeta/2)^2 (x-y)^2}{1+y^2}, \tag{56}$$

$$x = (E - E_R - R)/\Gamma, \tag{57}$$

$\zeta = 2\Gamma/\Delta$, $\Delta = 2\sqrt{R k_B T_{eff}}$, σ_0 is the peak neutron cross-section and R is the recoil energy of the resonant nucleus. T^* is an effective temperature (measured in Kelvin) and is given by

$$k_B T_{eff} = \frac{3}{2} \int_0^{\infty} d\omega \omega g(\omega) \coth \frac{\omega}{2T k_B}. \tag{58}$$

T is the temperature, also measured in K. The finite thickness of the foil leads to further broadening of the absorption cross-section, and the probability for neutron absorption is given by

$$P_A(E) = 1 - \exp\left(-Nt\sigma_0 \Phi(\zeta, x)\right) \tag{59}$$

where N is the number density of resonant atoms perpendicular to the neutron beam, and t is the thickness.

These expressions have been used to calculate the energy resolution due to the gold analyser foils on eVS for a range of foil thicknesses at 290 K. The half-widths of the calculations are compared to half-widths derived from calibration measurements on eVS. The selection of the thickness of the foil is a compromise between intensity and resolution. As the thickness of the foil is reduced, clearly the difference count-rate will decrease, but also $1 - \exp(-\sigma Nt)$ tends to σNt, and the half-width of $\sigma(E)$ tends to the half-width of $\phi(\zeta, x)$. As the thickness d increases, the probability of absorbing a neutron in the region of the cross-section energy increases at the expense of a degradation in the resolution. The choice of the foil and the foil thickness depends

to a certain extent on what systems are being studied. However, a simple criterion is [41] $Nt\sigma_0 = 1$. This gives for gold an optimum foil thickness of 5.6 μm. For systems with broad neutron Compton profiles it is desirable to choose a thicker foil, giving better count-rates.

Other points regarding the selection and characteristics of the resonance analyser are discussed below.

1. The material used must be obtainable and easily handled. The peak cross-section σ_0 should be large compared to the off-resonance cross-section.
2. The resonance must be at a useable energy and well separated from other resonances in order to avoid overlap effects where neutrons captured by neighbouring resonances arrive with the same time-of-flight.
3. The width of the Doppler-broadened resonance should be consistent with the resolution requirements for the measurement being undertaken.

For a survey of resonance analyser foils (^{198}Au, ^{238}U, etc.) for epithermal neutrons see reference [44].

2.7 THE ELECTRON-VOLT SPECTROMETER (eVS)

A schematic diagram of the eVS (from [45]) is shown in figure 2.10. eVS is an inverse geometry machine and uses resonant foils in the scattered beam to define the energy of the scattered neutrons. At the time of the experimental results reported in this thesis, the spectrometer had six banks of 10 atmosphere ^{3}He neutron detectors covering angles in the ranges 35° to 53° degrees, 57° to 76° degrees and 125° to 137° respectively. In total this arrangement comprised fifty detectors arranged symmetrically about the incident beam direction as shown. Each neutron detector is 2.5 cm in diameter and 30 cm in length. The detectors are arranged with their axes vertical and with their centres at the height of the beam. There were forty detectors arranged at forward-scattering angles ($\theta < 90°$) and ten at backward-scattering angles at the time of the taking of the

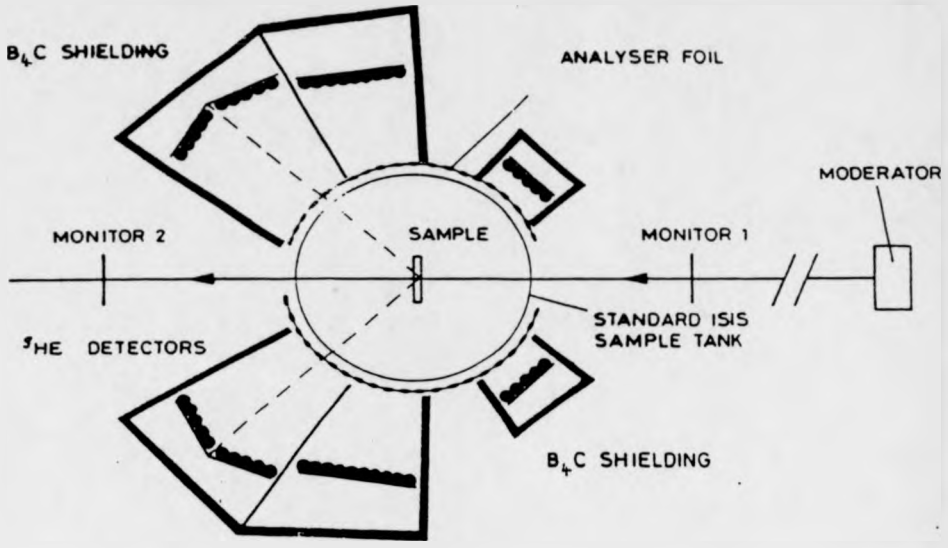

Figure 2.10 The Electron Volt Spectrometer. Pulses of neutrons with a wide range of energies arrive from the moderator. Neutrons scattered into a specific energy defined by resonant foils around the sample are detected by fifty ^{3}He neutron detectors arranged symmetrically about the incident beam direction. Information on the momentum distribution of the target particles is deduced from the time-of-flight spectra measured with the resonant foils in and out of the scattered beam. The thirty detectors at lowest scattering angles are grouped together in three banks referred to in the text as banks A, B and C. These are marked in the figure.

measurements presented in this thesis. The ratio of incident to scattered velocity for a free particle of mass m scattering from a particle of mass M is

$$\alpha = \frac{V_1}{V_0} = \frac{\cos\theta + [(\frac{M}{m})^2 - \sin^2\theta]^{\frac{1}{2}}}{\frac{M}{m} + 1} \qquad (60)$$

where V_0 is the incident velocity, V_1 is the scattering velocity, M is the mass of the scatterer, m is the neutron's mass and θ is the scattering angle. For neutron scattering from hydrogen nuclei, $m = M$ to a very good approximation and therefore the scattering angle is restricted to $\theta < 90°$. The detectors at forward-scattering angles are therefore used primarily for the study of systems containing hydrogen. Glass scintillation detectors are in the incident beam before and after the sample position, and enable the normalisation of spectra to the incident beam and for the calculation of scattering powers. The beam tubes and the sample chamber are evacuated during normal operation of the instrument. A rotary pump located outside the eVS blockhouse is used for this purpose. The sample holder used is a plane square slab placed perpendicular to the beam mounted on the end of an aluminium stick which rests on top of the sample chamber. The resonant foils are mounted on a cylindrical aluminium holder which surrounds the sample chamber. It is necessary to minimise the effects of changes in the relative efficiency of the detectors to neutrons at different energies. These changes occur slowly on a time-scale of hours, so are effectively removed by cycling the resonant foils in and out of the beam every five minutes. They can be removed from the beam by the activation of pneumatic pistons to which the holder is attached. The collection of the time-of-flight spectra is performed by the data acquisition electronics (DAE). The upper and lower limits of the measured time-of-flight spectrum and the widths of the time-bins, are defined by the user. The source pulses at a frequency of 50 Hz and so the collection of data over the whole time-of-flight region occurs fifty times each second.

Two types of measurement are made: one with the resonant foils in and one with the resonant foils out of the scattered beam. In figure 2.11 is shown the time of flight spectrum for scattering from ZrH_2 collected at a scattering angle of 36° with the foil out of the scattered beam, for zirconium hydride, together with a time of flight spectrum

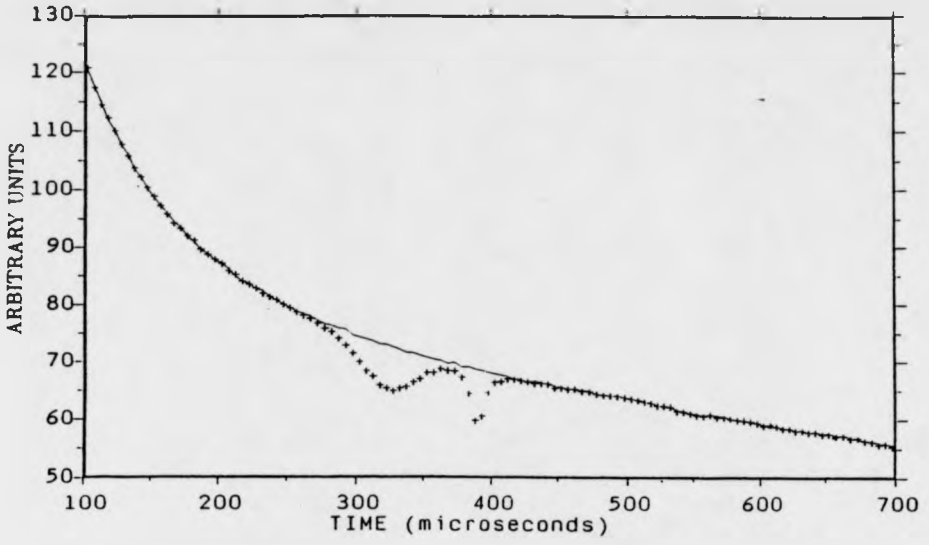

Figure 2.11 A 'foil in' (+) and a 'foil out' (solid line) time-of-flight spectrum for a measurement on ZrH_2 at an angle of 36 °. The spectra are normalised so that they have the same integrated counts between 500 and 600 μs. The difference between the two is the difference time-of-flight spectrum.

measured with the foil in. Each is normalised to have the same integrated intensity between 500 and 600 μs. The difference gives the difference time-of-flight spectrum. The time-of-flight spectra for the 'foil in' and 'foil out' case are collected in separate areas of memory by the instrument computer. The 'raw' data are then in the form of 100 time-of-flight spectra, two for each detector.

2.7.1 Determination of $J(y)$ from eVS data

A schematic diagram of an inverse geometry spectrometer is shown in figure 2.12. The energy E_1 and therefore velocity V_1 of the detected neutrons is fixed by the resonant energy of the analyser foil. The velocity V_0 and energy E_0 of the incident neutron can be determined from the measured time of flight t

$$t = \frac{L_0}{V_0} + \frac{L_1}{V_1} + t_0 \tag{61}$$

where L_0 is the primary flight path from moderator to sample, L_1 is the secondary flight path from sample to detector, and t_0 is the delay time in measuring t. The electronics for measuring the time-of-flight of detected neutrons begins counting when the pulse of 'white' neutrons leaves the moderator. Upon detection, the time registered for each neutron is the time taken for it to leave the moderator, scatter from the sample and reach the detector plus an electronic delay in processing, t_0, which is assumed constant. The energy of the neutron is related to its velocity by

$$E = 5.2276 \times 10^{-6} V^2 \tag{62}$$

where E is measured in meV and V is measured in ms^{-1}. The wavenumber, k, of the neutron in Å^{-1} is related to the energy in meV through the equation

$$k = \left(\frac{E}{2.0717}\right)^{\frac{1}{2}}. \tag{63}$$

The energy transferred from the neutron to the target is

$$\omega = E_0 - E_1 \tag{64}$$

and the momentum transfer q is given by

$$q = (k_i^2 + k_f^2 - 2k_0k_1\cos\theta)^{1/2} \tag{65}$$

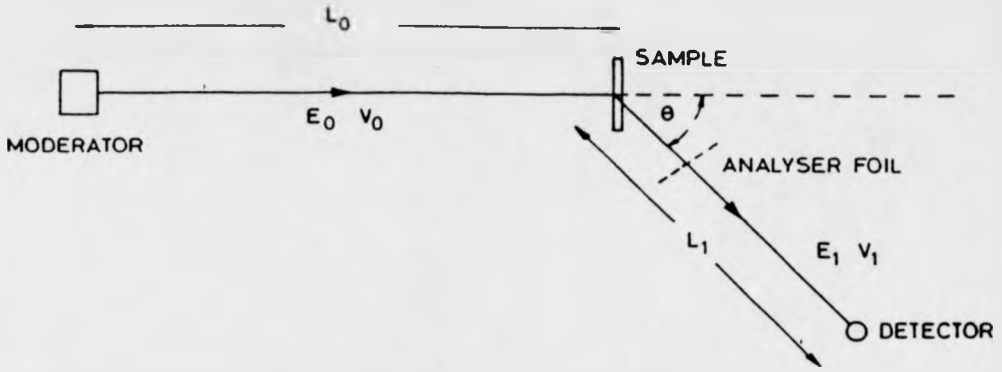

Figure 2.12 Schematic diagram of an inverse geometry spectrometer.

L_0 = incident flight path

L_1 = scattered flight path

θ = scattering angle

E_0 = energy of incident neutron

E_1 = energy of detected neutrons

where θ is the scattering angle.

The values of q and ω defined by equations 61 to 65 define the locus of points in q, ω space that each detector scans. They uniquely relate each value of y to a point in the TOF spectrum via equation 25. They are easily calculated via the above equations once L_0, L_1, θ, t_0 and E_1 have been determined.

The counts $C(t)$ observed in a time bin are now related to $J(y)$. This has been done in work by Mayers et al [45], but is reiterated here for completeness. The number of counts collected in a time channel of width Δt centred at t is [46],

$$C(t)\Delta t = I(E_0)\frac{dE_0}{dt}\Delta t N \frac{d^2\sigma}{d\Omega dE_1}\eta(E_1)\Delta\Omega\Delta E_R \tag{66}$$

where $I(E_0)\frac{dE_0}{dt}\Delta t$ is the number of incident neutrons/cm^2 corresponding to the time channel, N is the number of scattering atoms, $\Delta\Omega$ is the detector solid angle, ΔE_R is the energy resolution of the analyser, $\eta(E_1)$ is the efficiency of the detector and $d^2\sigma/d\Omega dE_1$ is the partial differential neutron scattering cross-section. The latter quantity is related to the dynamic structure factor $S(q,\omega)$ via equation 10 [5]. Equations 66 and 10 lead to the result

$$C(t)dt = \left[\frac{N\Delta\Omega\eta(E_1)k_f\Delta E_R\sigma M}{4\pi}\right]\left(\frac{I(E_0)\frac{dE_0}{dt}\Delta t J(y)}{k_i q}\right) \tag{67}$$

The bracket [ ] contains all factors which are independent of t. It can be shown that $I(E_0) \propto E^{-0.9}$. Furthermore $k_i \propto {E_0}^{0.5}$ and it is possible to show that for a fixed final energy E_1, $dE_0/dt \propto E_0^{1.5}$. Thus

$$J(y) = A\frac{qC(t)}{E_0^{0.1}} \tag{68}$$

where A is the product of all parameters which are independent of t. The value of A can be determined from

$$\int_{-\infty}^{\infty} J(y)dy = 1 \tag{69}$$

which is required since $J(y)$ is a probability distribution.

2.7.2 Instrument calibration

The five instrument parameters L_0, L_1, E_1, θ and t_0 defined by equations 61 to 65 need to be determined for each detector by a careful calibration of the instrument. The eVS calibration procedures have been described fully in a previous work (reference [45], sections 4 and 5). The eVS is calibrated at least once each ISIS cycle. Slight movements of the detectors, adjustments in the position of the beam between cycles, and changes in the data acquisition electronics all affect the calibration.

Below, the calibration procedures for each of the five instrument parameters and their uncertainties are explained. The relationship between the uncertainties in these parameters and the corresponding contributions to the resolution function is shown.

2.7.2.1 Length calibration

The primary and secondary flight-paths L_0 and L_1 were determined for each detector in the following manner. The distances L_1 for each detector was measured with a metre rule. The total distance $L_0 + L_1$ and the time-delay t_0 were determined for each detector by measuring the positions of uranium resonance absorption lines in the time-of-flight spectrum with a 1mm thick lead sample at the sample position. A thin uranium foil was placed fully covering the incident beam, close to the moderator (about half-way between the target station and the sample position). Uranium has four strong well-defined neutron resonances at 6671, 20872, 36680 and 66020 meV which appear in time of flight on eVS over the time-range used for recoil scattering. The foil was well separated from the detectors in order not to be a source of additional noise. For elastic scattering, the positions the resonance lines are observed to occur at time-of-flights given by

$$t = \frac{L_0 + L_1}{V_R} + t_0 \tag{70}$$

where V_R is the neutron velocity corresponding to the resonance energy. For recoil scattering a correction needs to be made, since $V_1 < V_0$. From equation 60, equation

70 therefore becomes

$$t = \frac{L_0}{V_R} + \frac{L_1}{\alpha V_R} + t_0. \tag{71}$$

For scattering from lead and for $\theta = 90°$, $\alpha = 0.9951$. so taking the recoil into account affects L to about 0.05 %.

The uranium resonances appear as dips in the spectrum. The resonance peak positions were located visually using the computer graphics package GENIE [48]. Figure 2.13 shows for example the time-of-flight spectrum for a detector at 35.96 ° with the uranium foil in the incident beam. By plotting the times of flight of the absorption lines for the three lowest resonances against $1/V_R$ and performing a least squares fit, the gradient obtained is $L_0 + \frac{L_1}{\alpha}$. L_0 can therefore be obtained if L_1 and α are known. Obviously, in a first calibration, θ and therefore α will not be known precisely. The values for θ obtained in the angles calibration described in the next section may then be used again to obtain new values for L_0. If these deviate significantly from the initial set of values, then the angle calibration can be repeated in a self-consistent procedure.

The calibration of the detector configuration used for the data presented in this thesis gave a value of $L_0 = 11.055 \pm 0.019$ where 0.019 is the standard deviation of the L_0 values obtained for the fifty detectors. This standard deviation represents the uncertainty in the initial flight-path due to the finite size of the sample and the moderator. This value is used in calculating the variance of the Gaussian contribution to the resolution function from the uncertainty in the initial flight paths (see section 2.7.3). The delay time t_0 is also determined for each detector. The origin of this delay time is in the data acquisition electronics. This was determined to be -5.63 ± 1.45 μs for detectors 11 to 30 and -5.76±1.45 for detectors 31 to 50. The uncertainty 1.45 in the delay time is taken to be the measure of the fluctuation in the measured time-of-flight of a neutron. The uncertainty in the final scattered flight path was determined to be 0.009 m.

2.7.2.2 Angle calibration

The scattering angles were determined from the positions in time-of-flight of the diffrac-

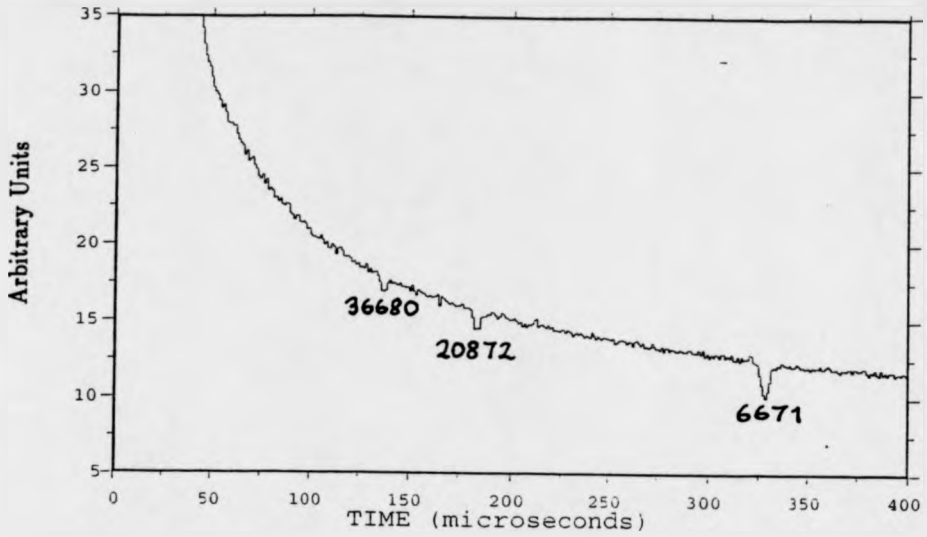

Figure 2.13 For the length calibration of eVS, a uranium foil is placed in the incident beam and the positions in time-of-flight of three uranium resonances at 6671, 20872 and 36680 meV are located for each detector. Shown is one such spectrum (detector 11 for which $2\theta = 35.96°$).

tion peaks of a powdered silicon sample. Bragg's law gives

$$2d_{hkl}\sin\left(\frac{\theta}{2}\right) = \lambda = \left(\frac{t - t_0}{L}\right) \times 3.9554 \times 10^{-3} \qquad (72)$$

where θ is the angle the neutron is scattered through, d_{hkl} is the spacing measured in Å of the planes giving the Bragg reflection (hkl), λ is the neutron wavelength in Å, and t and t_0 are measured in microseconds. Silicon is fcc with a lattice parameter of 5.43 Å. The times-of-flight of the six largest d_{hkl} - the (111), (220), (311), (400), (331), and (422) peaks - were determined using the GENIE graphics package and a value for $L\sin(\theta/2)$ determined for each peak using the values for t_0 obtained from the procedure with the uranium foil described in the previous section.

The scattering angles and other parameters used in the processing of the data in this thesis are shown in tables 2.1a and 2.1b.

The uncertainty in the angle is taken to be due to the finite width of the ^{3}He detectors. These have an effective diameter of 1.8 cm so the error in the angle of a detector is taken to be $0.5 \times 1.8/L_1$ where L_1 is the measured final flight path in centimetres.

2.7.2.3 Energy of analyser foil

A gold foil was used in the experimental work reported in this thesis. The energy of the resonance used (4922 meV) and the half-width at half maximum was determined by a calibration procedure. For recoil scattering, once the instrument parameters are known, the final energy of the scattered neutron can be calculated from the time-of-flight. From equations 71 and 62,

$$E_1 = 5.2276 \times 10^{-6}\left(\frac{L_0 + L_1/\alpha}{t - t_0}\right)^2 \qquad (73)$$

By transforming from time-of-flight to final energy in this way measurements of recoil scattering from lead, values of E_1 for the gold resonance from the fitted peak position can be obtained. It is sufficient to fit a Lorentzian function to the data in E_1 in order to obtain the peak position. One recent measurement of this kind gave a value of 4918.5 ± 0.6 meV for the resonance in ^{198}Au used for these DINS measurements. This

Detector	θ/°	t_0/μ s	L_0/m	L_1/m
1	139.8400	-6.3000	11.0550	0.4940
2	136.5267	-6.3000	11.0550	0.4940
3	133.1767	-6.3000	11.0550	0.4940
4	130.0200	-6.3000	11.0550	0.4940
7	136.6533	-6.3000	11.0550	0.4940
8	133.3333	-6.3000	11.0550	0.4940
9	130.0567	-6.3000	11.0550	0.4940
10	126.5533	-6.3000	11.0550	0.4940
11	-35.9607	-5.6300	11.0550	0.8820
12	-37.9330	-5.6300	11.0550	0.8820
13	-39.7997	-5.6300	11.0550	0.8820
14	-41.7933	-5.6300	11.0550	0.8820
15	-43.6493	-5.6300	11.0550	0.8820
16	-45.8243	-5.6300	11.0550	0.8820
17	-47.7767	-5.6300	11.0550	0.8820
18	-49.7333	-5.6300	11.0550	0.8820
19	-51.5710	-5.6300	11.0550	0.8820
20	-53.6827	-5.6300	11.0550	0.8820
21	36.0270	-5.6300	11.0550	0.8820
22	38.1433	-5.6300	11.0550	0.8820
23	39.9253	-5.6300	11.0550	0.8820
24	41.9127	-5.6300	11.0550	0.8820
25	43.8150	-5.6300	11.0550	0.8820
26	45.9407	-5.6300	11.0550	0.8820
27	47.8017	-5.6300	11.0550	0.8820
28	49.7390	-5.6300	11.0550	0.8820
29	51.7103	-5.6300	11.0550	0.8820
30	53.6673	-5.6300	11.0550	0.8820

Table 2.1a The instrument calibration parameters.

Detector	θ / °	t_0 / μs	L_0 / m	L_1 / m
31	-57.4787	-5.7600	11.0550	0.7970
32	-59.7150	-5.7600	11.0550	0.7970
33	-61.8783	-5.7600	11.0550	0.7970
34	-63.9797	-5.7600	11.0550	0.7970
35	-66.0010	-5.7600	11.0550	0.7970
36	-68.3850	-5.7600	11.0550	0.7970
37	-70.4660	-5.7600	11.0550	0.7970
38	-72.5960	-5.7600	11.0550	0.7970
39	-74.7100	-5.7600	11.0550	0.7970
40	-76.8700	-5.7600	11.0550	0.7970
41	57.7577	-5.7600	11.0550	0.7970
42	59.9433	-5.7600	11.0550	0.7970
43	62.0170	-5.7600	11.0550	0.7970
44	64.2013	-5.7600	11.0550	0.7970
45	66.2487	-5.7600	11.0550	0.7970
46	68.4807	-5.7600	11.0550	0.7970
47	70.5137	-5.7600	11.0550	0.7970
48	72.7517	-5.7600	11.0550	0.7970
49	74.7803	-5.7600	11.0550	0.7970
50	76.9787	-5.7600	11.0550	0.7970
51	0.0001	-9.3000	11.0550	2.3820
52	0.0001	-9.4100	11.0550	-2.4600

Table 2.1b The instrument calibration parameters.

is close to the value of 4922 meV used in the analysis and simulation of data in this thesis.

2.7.2.4 Incident beam intensity

The incident beam intensity as a function of energy, $I(E_0)$, is required for calculating $J(y)$ from the time-of-flight spectra via equation 67. This has been done in reference [45]. A least-squares fit to

$$I(E_0) = \frac{A}{E_0^n} \tag{74}$$

was performed to determine the parameter n, found to be close to 0.4. The form of equation 74 was found to fit the incident energy spectrum well. A correction was made for the efficiency of the monitor in the incident beam ($\propto E^{-\frac{1}{2}}$), with the result that $I(E_0) \propto E^{-0.9}$. This agrees with the predicted incident spectrum [2].

2.7.3 Instrument resolution

The analysis of the difference spectra in time-of-flight leads to a measured neutron Compton profile $J_m(y)$ for each detector used. A value of σ can be deduced from each $J_m(y)$ by knowing the resolution function in y-space for each detector. This section describes the origin of the resolution function, its form (in terms of a Voigt function), and the determination of each of the components for each detector from the uncertainties in the instrument parameters.

The resolution of the instrument is determined primarily by the width of the resonance used. Analytical expressions for the components of the instrument resolution have been dealt with in a previous paper [47]. The five independent contributions to the resolution in y space originate from the uncertainties in the five instrument parameters. The way in which each contribution is determined is outlined below.

1. The energy width ΔE_R of the resonant absorber is the largest contribution to the resolution function in the case of gold resonant absorbers, which are generally used for hydrogeneous scattering. This is calculated using the expressions in sec-

tion 2.6 and compared to a measurement of the resolution function by scattering from heavy systems such as Pb.

2. The angular resolution contribution is small except for scattering from hydrogeneous systems. It was determined for all the detectors from the peak shape of powder diffraction peaks.

3. There is a distribution of L_0 values caused by the finite sample width and depth of the neutron moderator. This contribution is always small compared to that from ΔE_R and is known from the calibration of the instrument lengths described in section 2.7.2.1.

4. There is a distribution of L_1 values due to the finite sample width and detector depth. The uncertainty in the flight paths can be estimated from the length calibration described in 2.7.2.1.

5. The uncertainty in the TOF due to the finite width of the time bins, Δt. Δt is chosen so that this effect is negligible. At very short times, the error in measuring the time-of-flight increases significantly, but for most systems measured on eVS, this is not a problem because the region of interest is at longer times. There is, however, a fluctuation in the measured time-of-flight of a neutron of about 1.5 μs which arises in the DAE.

2.7.3.1 The measured neutron Compton profile

The measured neutron Compton profile $J_m(y)$ for a given detector is a convolution of the intrinsic momentum distribution with the resolution contributions.

$$J_m(y) = J(y) * R_\theta(y) * R_{L_1}(y) * R_{L_2}(y) * R_T(y) * R_E(y) \qquad (75)$$

where $R_\theta(y)$ is the angular, $R_{L_0}(y)$ the L_0, $R_{L_1}(y)$ the L_1, $R_T(y)$ the time and $R_E(y)$ the energy component of the resolution in y space. The components $R_\theta(y)$, $R_{L_0}(y)$, $R_{L_1}(y)$ and $R_T(y)$ are empirically Gaussian with variances of σ_θ, σ_{L_0}, σ_{L_1} and σ_T respectively, and the component $R_E(y)$ Lorentzian in form, with a half-width at half-maximum of

σ_E. It is assumed that $J(y)$ is Gaussian with a variance σ, and the total resolution function is therefore represented by

$$R(y) = J_b(y) * R_E(y) \tag{76}$$

where $J_b(y) = R_\theta(y) * R_{L_0}(y) * R_{L_1}(y) * R_T(y)$ is a Gaussian of variance

$$\sigma_b = \sqrt{\sigma_\theta^2 + \sigma_{L_0}^2 + \sigma_{L_1}^2 + \sigma_T^2}. \tag{77}$$

The measured neutron Compton profile obtained from one detector is then $J_m(y) = R(y) * J(y)$ with $\int R(y)dy = 1$.

These parameters σ_θ, σ_{L_0}, σ_{L_1}, σ_T and σ_E introduced above vary from detector to detector. They need to be known for each detector in order to extract the variance of $J(y)$ measured by that detector. The analysis is restricted to determining the variance of $J(y)$ measured by each detector. No lineshape analysis is done for measurements in this thesis since the statistical accuracy of these measurements does not merit it.

2.7.3.2 Determination of the components of $R(y)$

The components to the resolution function for a given detector can be calculated in time-of-flight or y-space from the calibrated uncertainties in the five instrument parameters. These are $\Delta\theta$, ΔL_0, ΔL_1, ΔE_R and Δt_0. It has been shown in section 2.7.1 how y is calculated from these five parameters. It is assumed that a Gaussian distribution of θ, L_0, L_1, or t results in a Gaussian distribution in y space. This follows if the higher order terms in equation 78 are neglected. The solid line in figure 2.14 shows the resolution calculated in this way in y-space for a detector at 35.96°. The uncertainties that have been used to calculate this function are those given above. The flight-path uncertainties σ_{L_0} and σ_{L_1} are not strictly independent because they both depend on the position of the scattering event, but these terms are relatively small so no significant error results from neglecting this interdependence.

For example, the change in y due to a change in L_0 of ΔL_0 is given by

$$y(t, \theta, E_1, L_0 + \Delta L_0, L_1, t_0, M) = y(t, \theta, E_1, L_0, L_1, t_0, M) + \sum_{n=1}^{\infty} \frac{1}{n!} \frac{\partial^n y}{\partial {L_0}^n} \Delta L_0^n. \tag{78}$$

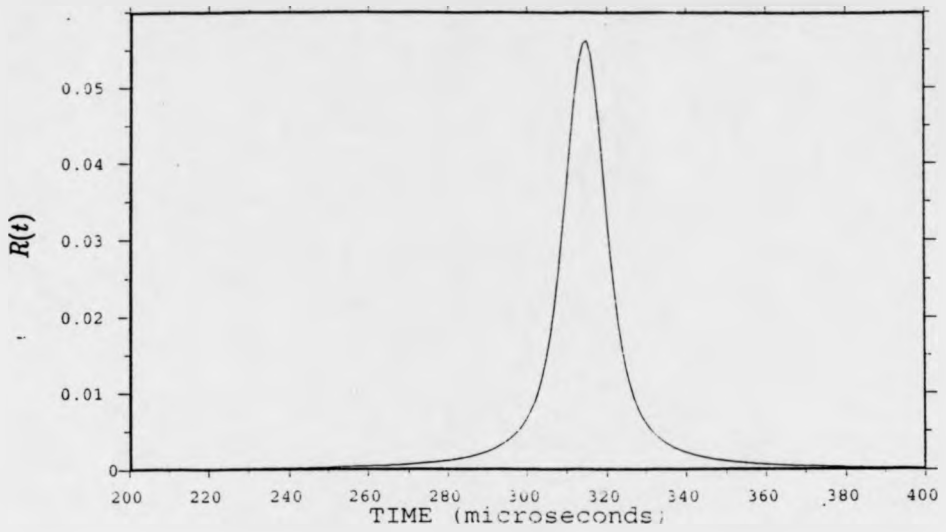

Figure 2.14 The calculated eVS resolution function in time-of-flight for scattering from H and for detector 11. For the purposes of 'can-subtraction' a resolution function is required in time-of-flight. For fitting to the measured neutron Compton profile in y-space, a resolution function is needed in y-space. Each function is calculated as a Voigt function with Gaussian and Lorentzian components determined from the uncertainties in the five instrument parameters. Their compatability is demonstrated in this and the next figure.

So long as terms of higher order are small, the change in y can be determined from the derivatives of first order only. Analytical expressions for the partial derivative of y with respect to each of the instrument parameters are presented in the appendix of reference [45]. For scattering neutrons from hydrogen, $M = m$ to a very good approximation and [45]

$$\frac{\partial y}{\partial E_1} = -\frac{M}{k_1 \sin\theta}\left[\cos\theta + \frac{L_1}{L_0}\right] \quad (79)$$

$$\frac{\partial y}{\partial \theta} = -k_1 \quad (80)$$

$$\frac{\partial y}{\partial L_0} = \frac{k_0}{L_0 \tan\theta} \quad (81)$$

$$\frac{\partial y}{\partial L_1} = \frac{k_1}{L_0 \sin\theta} \quad (82)$$

For example, $\sigma_{L_0} = \frac{\partial y}{\partial L_0}\Delta L_0$. This is calculated numerically. If the determined uncertainty in L_0 is ± 0.005 m then the full width at half-maximum (FWHM) uncertainty in y is given by $|y(t,\theta,L_0 - 0.005, L_1, E_1, t_0) - y(t,\theta,L_0 + 0.005, L_1, E_1, t_0)|$.

The resolution parameters that determine the calculated resolution function in y-space are given in table 2.2 for scattering from hydrogen in ZrH_2.

det. no.	σ_E	σ_θ	σ_{L_0}	σ_{L_1}	σ_T
11	1.048	0.497	0.115	0.068	0.334
15	0.805	0.497	0.088	0.057	0.284
20	0.577	0.497	0.061	0.049	0.243
31	0.500	0.550	0.053	0.047	0.232
35	0.362	0.550	0.037	0.043	0.214
40	0.210	0.550	0.019	0.040	0.200

Table 2.2 Resolution parameters in y-space for scattering from hydrogen in ZrH_2. The dependence on scattering angle is shown. All parameters are in units of $Å^{-1}$. A gold analyser foil is assumed in the calculations, with $E_R = 4922meV$ and $\Delta E_R = 140$ meV.

A similar procedure can be used to calculate the components to the resolution function in time-of-flight from equations 61 and 62. This can then be transformed to y-space

and the two normalised resolution functions can be compared for consistency. The resolution needs to be known in time-of-flight as well as in y-space for the modelling and subtraction of sample container scattering. This function is referred to as $R(t)$. it has components $R_\theta(t)$, $R_{L_0}(t)$, $R_{L_1}(t)$, $R_T(t)$ and $R_E(t)$ c.f. equation 75. Figure 2.14 shows this function in time-of-flight. The circles in figure 2.15 is this transformed resolution function and deviates slightly from the calculated resolution function in y-space. The difference, however, is small. The eVS resolution function has been calculated in this way taking into account the uncertainties in the instrument parameters and in order to compare the relative contributions from the foil transmission half-width at half-maximum (HWHM) and the uncertainties in the other parameters the resolution function has been transformed to E_1 space via equation 73 and a Lorentzian function has been fitted. The resulting HWHM are shown in figure 2.16 for scattering from hydrogen (filled triangles) and deuterium (open triangles) as a function of momentum transfer (i.e. for the different scattering angles). The result can be compared to figure 2.8.

It is perhaps misleading to see the fitted width ΔE_{tot} increasing with momentum transfer. The real criterion of the resolution of the instrument at high momentum transfer is the ratio of the y-space fitted HWHM to σ, or the variance of the neutron Compton profile being measured. This is shown in figure 2.17. The discontinuities in the line for H scattering in between 60 and 100 Å^{-1} is due to the Lorentzian fitting program used, which gives a result dependent to a certain extent on the bounds used on the data when fitting (the more so the more the data deviate from a Lorentzian).

The HWHM of the analyser foil absorption probability ΔE_R ($P_A(E)$ in section 2.6) is required to calculate the HWHM of the Lorentzian contribution to the resolution function in y-space. This is done both empirically and by numerical calculation using the expressions in section 2.6 for the probability of neutron absorption in the vicinity of a resonance. The probability distribution for a neutron being absorbed was calculated numerically for the 4922 meV resonance in gold (used on eVS for experimental data presented in this thesis). A value of $\sigma_0 = 30603$ barns for gold at 295 K was used [49]

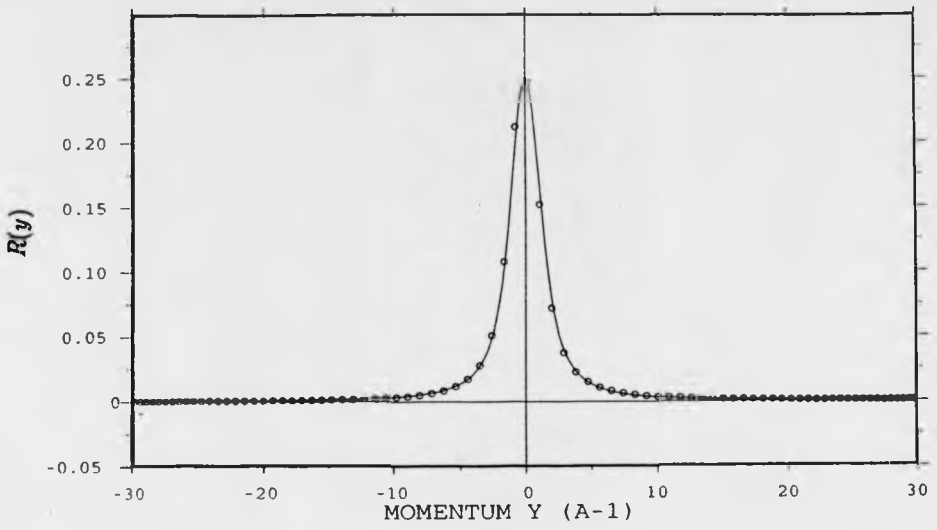

Figure 2.15 The calculated eVS resolution function in y-space is a Voigt-function centred at $y = 0$. Shown is the resolution function for scattering from hydrogen (...). The Lorentzian component is determined from the calibrated HWHM of the analyser foil resonance. The variance of the Gaussian component is the sum (added in quadrature) of the individual y uncertainties corresponding to the uncertainties in the flight paths L_0 and L_1, uncertainty in the measurement of the time of flight, and the scattering angle 2θ. The continuous line is the y-transformed resolution function of figure 2.14.

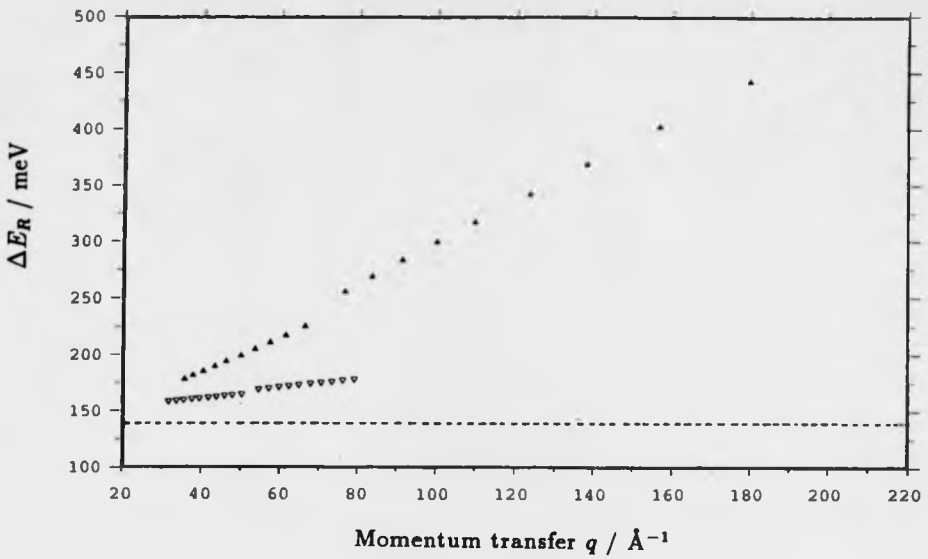

Figure 2.16 The Lorentzian HWHM (determined by fitting) of the calculated Voigt resolution function in E_1 space as a function of momentum transfer (which increases with increasing scattering angle) for scattering from hydrogen (▲) and from deuterium (▽). The dashed line represents the Lorentzian contribution from the analyser foil.

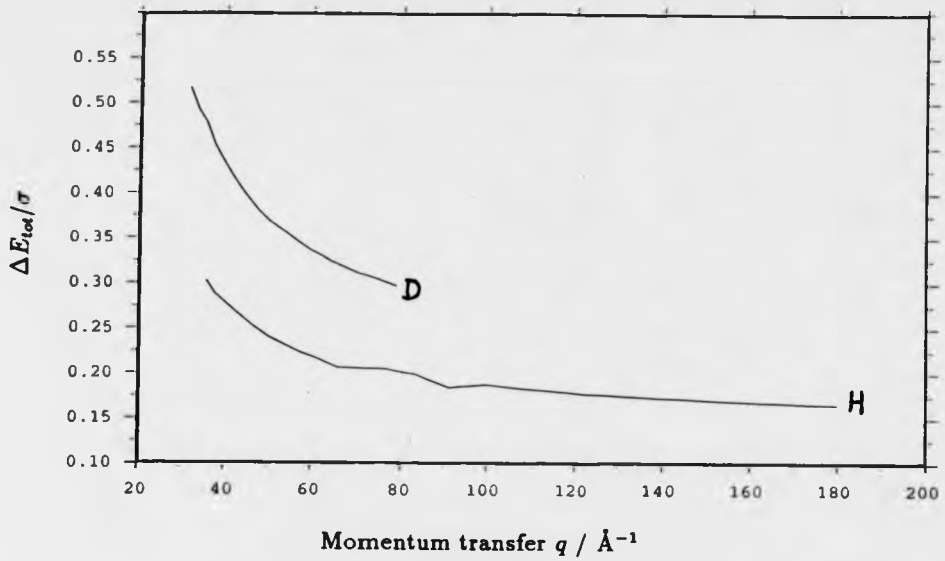

Figure 2.17 The ratio of the fitted Lorentzian HWHM to the Voigt resolution function in y-space to the variance of the system being studied. The top line is for scattering from deuterium, whilst the lower curve is for scattering from hydrogen. This is the true criterion for the resolution of an eV spectrometer.

and $P_A(E)$ was calculated for a range of thicknesses, at room temperature, using the expressions in section 2.6. The thickness of the gold analyser foils used on eVS was determined to be 10.59 μm. Figure 2.18 shows $P_A(E)$ for a gold foil of this thickness and at 290 K. A Lorentzian fit to these data gives a half-width at half-maximum of 127.4 meV at 290K. A Lorentzian was fitted for a series of $P_A(E)$ calculated in the range $0 < d < 20\mu$m and was a good approximation over this range of d. The goodness of the fit confirms that the expected form of $P_A(E)$ is Lorentzian to a good approximation. The Lorentzian half-width at half-maxima thus obtained are shown as a function of thickness in figure 2.19 for a temperature of 290K. It is worth considering the temperature dependence of ΔE_R. Because of the relatively low Debye temperature of Gold (170 K), the temperature dependence is weak. The foils operate at room temperature. A possible temperature change of 20 K from 280 K to 300 K only increases ΔE_R from 126.8 meV to 128.0 meV, a change of less than one percent.

The empirically determined value for ΔE_R was determined from recoil scattering from heavy nuclei : Pb - 207.2 amu, V - 50.9 amu, and Sn - 118.7 amu. The momentum distribution of such a high scattering mass, and hence σ is close to a δ-function compared to the resolution function. This can be understood from the fact that the constant q width of $S(\mathbf{q},\omega)$ scales as $1/M$. By estimating the variance of $J(y)$ from the Debye temperature (equation 33) and when the other Gaussian components to the measured neutron Compton profile are known, σ_b is known and the Lorentzian component σ_E can be determined by fitting a Voigt function with σ_E as a free parameter. Five measurements, three of Sn, one of Pb and one of V were made with the same detector configuration as were the measurements presented in this thesis, so these were used to calibrate σ_E. Table 2.3a shows the fitted values of σ_E for these five measurements for three banks of detectors: at back-scattering, 1-10, and at forward scattering, 11-30 and 31-50. σ_E relates to a width in energy via equation 79 and these values are given in meV in energies is given at the bottom of each energy column.

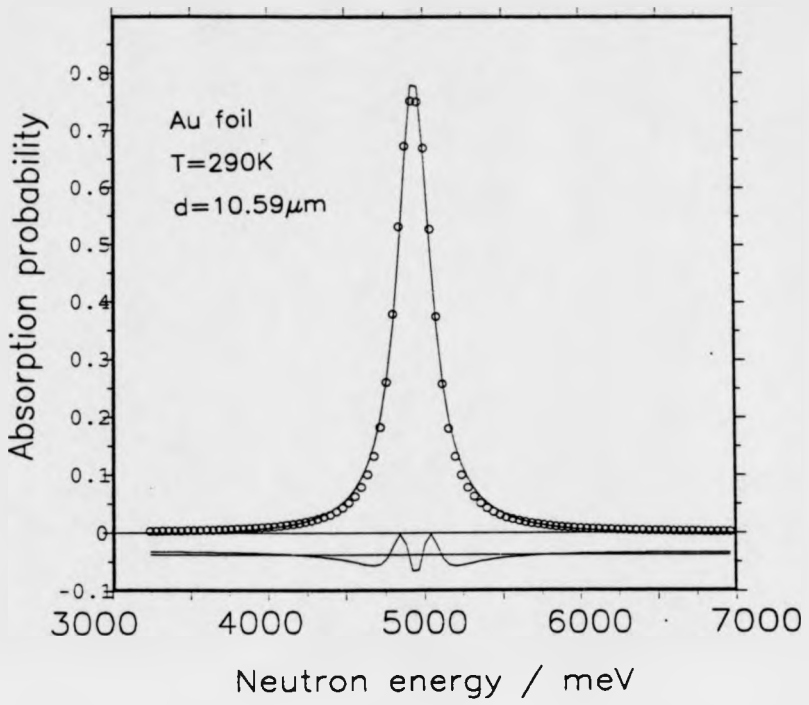

Figure 2.18 A calculation (circles) of the transmission $P_A(E)$ of neutrons by a gold analyser foil at 290K with a thickness of 10.59 μm. This is the measured thickness of the analyser foils used on the eVS spectrometer. The solid line is a Lorentzian fit to the calculation.

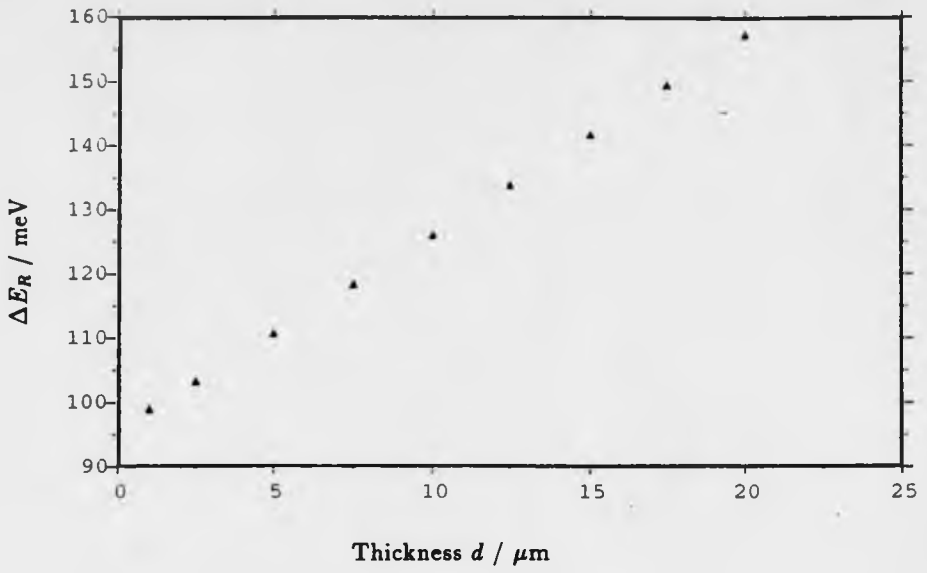

Figure 2.19 The fitted Lorentzian HWHM of the calculated transmission $P_A(E)$ of a gold analyser foil at 290K.

Sample	Run no.	σ_E/Å^{-1} (1-10)	σ_E/Å^{-1} (11-30)	σ_E/Å^{-1} (31-50)
Pb	1112	70.96±0.48	186.4±1.3	125.9±0.9
Sn	1114	39.0±0.4	104.3±1.0	72.0±0.7
Sn	1115	39.2±0.3	105.5±0.6	72.0±0.4

Table 2.3a The calibrated σ_E values, the half-width at half-maximum of the Lorentzian resolution contribution in y-space from the analyser foil.

Sample	Run no.	ΔE_R/meV (1-10)	ΔE_R/meV (11-30)	ΔE_R/meV (31-50)
Pb	1112	122.0±0.8	129.9±0.9	128.3±0.9
Sn	1114	116.6±1.3	126.8±1.2	127.5±1.2
Sn	1115	117.3±0.8	128.1±0.7	127.9±0.7
mean		121.3±4.3	127.7±0.5	125.8±1.9

Table 2.3b The calibrated values of ΔE_R, the half-width at half-maximum of the Lorentzian resolution contribution due to the analyser foil.

The widths obtained at forward scattering angles agree closely with the value of 127.4 meV given above for the numerical calculation of ΔE_R for a gold foil.

2.7.4 Data analysis

The data analysis procedure is outlined below for samples in which there is no strong anisotropy in the momentum distribution. The programming was done in FORTRAN [50]. At this stage, the assumption is that $J(y)$ is gaussian and the object of the analysis is to determine the Variance of that Gaussian for each of the detectors being used. A weighted sum is then made of the set of variances obtained.

1. The first process is the calculation of the difference time-of-flight spectra from the time-of-flight spectra collected with ('foil in') and without ('foil out') the resonant foils in the scattered beam. The 'foil in' and 'foil out' time-of-flight spectra are normalised to the incident beam monitor so that they have the same integrated intensity between 500 and 600 μs. In this region, the time-of-flight spectrum is

assumed to be of the same form for both foil in and foil out measurements since it is removed from the region where recoil scattering occurs.

2. Recoil scattering from nuclei of masses other than that of interest in the sample is subtracted. This is done by fitting a sum of Voigt functions to each time-of-flight spectrum. A Voigt function is fitted to the scattering from each mass present, with its centre constrained to the position in time of flight for recoil scattering from the mass concerned. As an example, figures 2.20 and 2.21 show such fits to ZrH_2 data presented in chapter 3. Figure 2.20 shows the time-of-flight spectrum for scattering at an angle of 35.96 °. The ZrH_2 sample was in an aluminium holder so the fit is to three masses: H, Al and Zr. The difference of the 'foil-in' and 'foil out' data are shown by the circles. The line is the fit to the scattering from the Al and the Zr. The fit takes into account the resolution function, which is calculated according to section 2.7.3. Figure 2.21 shows the difference spectrum for the same experiment but for a detector at a scattering angle of 53.67 °. The constrained positions of the centres of the fitted Voigt functions are shown in the insets in each figure.

   As a starting point for the fit, the Gaussian components of the resolution function in time-of-flight are obtained as explained in section 2.7.3.2. σ is estimated from the expression for σ for the ground state in a Debye solid $\sigma = \sqrt{\frac{3m\omega_D}{8\hbar^2}}$ where ω_D is the Debye energy. The Gaussian component of the Voigt function is then the sum added in quadrature of these widths. The Lorentzian contribution $R_E(y)$, is already known from the calibration procedure described in section 2.5.2.3. Each Voigt function is centred in time-of-flight at the recoil time given by equation 71. The unrequired contributions are subtracted leaving the time-of-flight spectrum of scattering from the mass of interest.

3. The next process is the transformation of the time-of-flight spectra to y-space through the IA result $y = \frac{M}{q}(\omega - \frac{q^2}{2M})$. A correction is made for the energy dependence of the time-of-flight spectrum, as described in section 2.7.1. The result is the measured Compton profile $J_m(y)$.

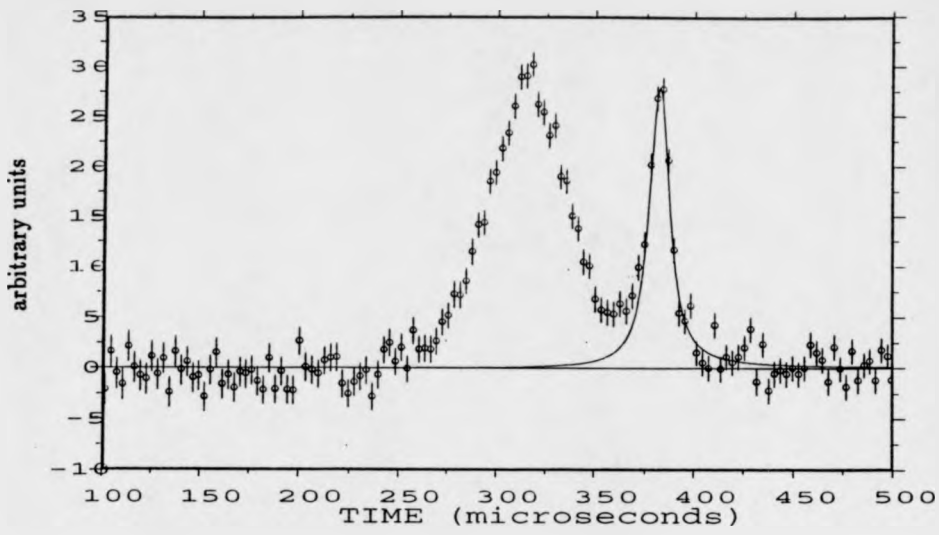

Figure 2.20 The time-of-flight difference for scattering from a sample of $ZrH_{1.96}$ at an angle of 35.96 ° – i.e. the difference resulting from the foil-in foil-out procedure applied to one ^3He detector. The fit to the quasi-elastic scattering from the zirconium and aluminium in the sample-holder is shown (solid line). The scattering from Al and Zr is represented by the sum of two Voigt functions. Each Voigt function is centred at the time-of-flight recoil-peak position for scattering from the mass concerned.

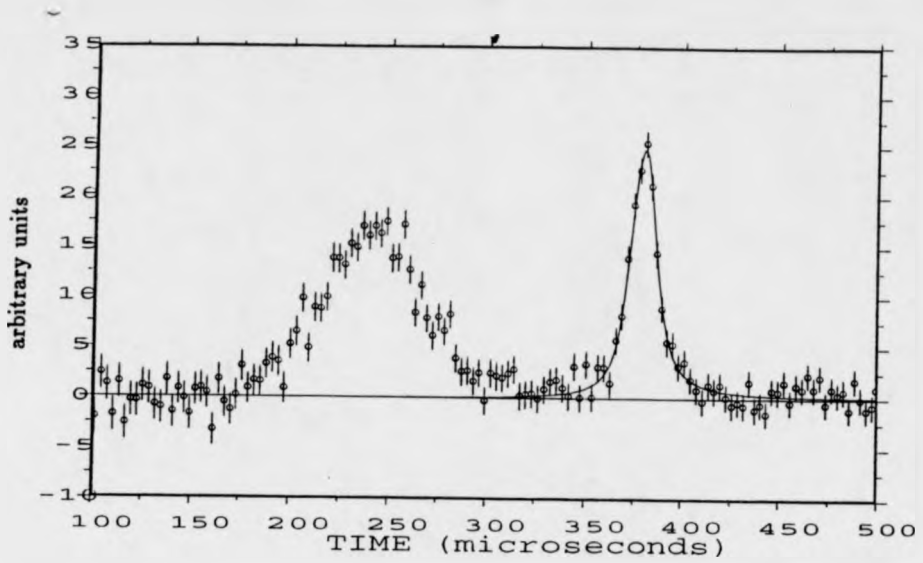

Figure 2.21 As figure 2.20 except this is at a scattering angle of 53.67° and so the hydrogen peak is shifted to significantly lower times-of-flight, corresponding to higher energy and momentum transfers. Again, the line is the fit to the scattering from the Zr and Al.

4. The next step is the fitting of a Voigt function to $J_m(y)$ to determine the variance σ of the neutron Compton profile $J(y)$, which is Gaussian in the harmonic approximation. The HWHM of the Lorentzian component to the resolution function, $R_E(y)$, is already known from the calibration procedure described in 2.5.2.3. This is used as the fixed parameter, and σ_b is therefore obtained from the fit. σ is then obtained from equation 77. The detector number, and fit parameters (peak height, position in y-space, variance, errors in these quantities, and χ-squared) are written to file. An example of such a fit is given in figure 2.22. The data of figure 2.20 has had the can-scattering subtracted, and has been converted to y-space. The data points are the transformed data, and the solid line is the fit. The fit parameters in this case were : peak height $2.009 \times 10^{-3} \pm 3.229 \times 10^{-5}$, peak position $-1.127 \times 10^{-1} \pm 9.040 \times 10^{-2}$, σ $4.192 \pm 1.031 \times 10^{-1}$ and χ^2 0.8747.

5. The neutron Compton profile is a probability distribution and so $J_m(y)$ is normalised to unity. It is important to normalise within limits that include the whole NCP so that differences in two NCPs, for example, are not affected by normalisation errors.

6. A sum of $J_m(y)$ is calculated for specified combinations of detectors.

The final value of σ is obtained from a weighted sum of the σ values obtained from each fit. As a test of the impulse approximation, q_R^2 is plotted against ω_R

2.8 SUMMARY

This chapter has described epithermal neutron spectroscopy techniques, the characterisation of the eVS resolution function and the eVS data analysis. In the next three chapters, results on three systems are presented and comparisons are made to other measurements.

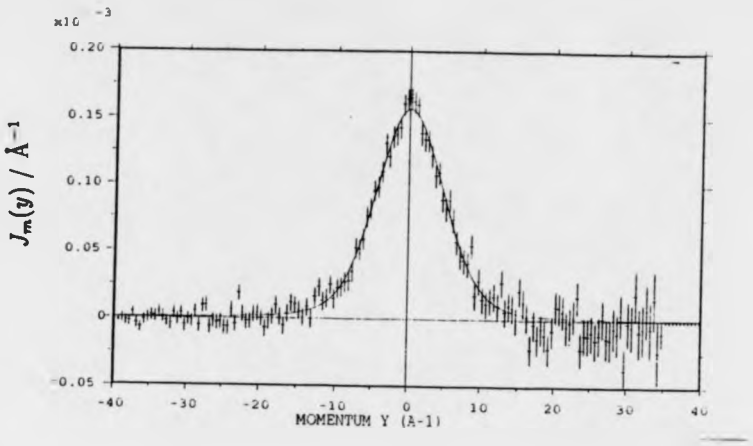

Figure 2.22 The y-transformed data of the hydrogen signal in figure 2.21 (for a single detector at a scayttering angle of 53.67 °. The solid line is the fit to the data (see item 4 in section 2.7.4).

CHAPTER 3

The validity of the impulse approximation in metal hydride systems

3.1 INTRODUCTION

In this chapter, measured neutron Compton profiles of ZrH_2 are compared to simulations based on the measured vibrational density of states of ZrH_2. Simulations of $S(q,\omega)$ are performed in the isotropic harmonic approximation using an analytic expression which is valid at all temperatures. The purpose of the simulations is to assess the scale of final-state effects and to see if those observed compare to those predicted from the model. An additional benefit in performing these simulations is to test the accuracy of the calibrations. Time-of-flight spectra for each eVS detector are calculated from the simulated $S(q,\omega)$, transformed to momentum space through the IA or the SIA, and compared to the similarly transformed eVS data over a range of momentum transfers. The procedure used for the simulation of $S(q,\omega)$ from the density of states has been used before in a paper examining initial state effects in DINS [9]. Deviations from the IA are looked for in both simulated and measured neutron Compton profiles. The IA consistently gives a more symmetrical and physically plausible neutron Compton profile than the Stringari Impulse Approximation (SIA) and leads to mean kinetic energies closer to that predicted from the measurement of the density of states over a range of momentum transfers.

Below, the procedure for determining $S(q,\omega)$ from the density of states is explained. The starting point is the density of states itself and the Debye-Waller factor. The density of states is derived from measurements performed on the MARI spectrometer, which is designed to measure $S(q,\omega)$ accurately over the kinematically limited region in q,ω space defined by the instrument geometry, incident energy and scattering mass. The density of states can, in principle, be obtained from the one-phonon contribution to $S(q,\omega)$ which dominates the scattering at low q. With the density of states known, the

next step is to construct $S(q,\omega)$ over a sufficiently wide range of energy and momentum transfer so that simulated eVS time-of-flight spectra can be calculated. In chapter 2 the detector scans through $S(q,\omega)$, which depend on the instrument parameters, were discussed in detail. The simulation of the time-of-flight spectra involves calculating $S(q,\omega)$ along these scans through q,ω space for each detector. These data in time-of-flight are then convoluted with the calculated instrument resolution function (whose parameters are determined from calibration measurements of the instrument). The eVS data analysis procedures described in the previous chapter are then used to simulated measured neutron Compton profiles from these spectra. The simulations are fitted to in the same way as 'real' eVS data to give the mean kinetic energy and other fit parameters such as the fitted peak position of the neutron Compton profile, which is an indicator for deviations from the impulse approximation.

The sample used in the measurements presented here was polycrystalline ϵ-phase ZrH_2. Its structure is shown in figure 4.2 (chapter 4). It is a completely ordered stoichiometric metal hydride, with hydrogen atoms occupying tetrahedral interstitial sites in the tetragonally distorted zirconium fcc sublattice. It is stable in the dihydride form from 0 K to greater than 800 K. The isotropic nature of the sample meant that eVS data from groups of detectors at similar scattering angles could be added to increase the statistical accuracy of the data. By summing data over 'banks' of detectors with similar scattering angles, measured neutron Compton profiles of high statistical accuracy were obtained, each corresponding to different ranges of momentum transfer. The high Debye temperature for hydrogen in ZrH_2 means that it is effectively in the ground state at room temperature. Therefore the proton can always be assumed to be scattered from the ground-state.

3.2 MEASUREMENTS OF $S(q,\omega)$ ON THE MARI SPECTROMETER

MARI is a direct geometry chopper spectrometer operating in time-of-flight. It has a very large array of detectors which permit the measurement of the dynamic structure factor $S(q,\omega)$ over a range of values in q,ω space, and resolution which is typically 1 to

2 % of the incident energy. The energy of the incident pulses of neutrons is determined by the rotational speed of the Fermi chopper, phased to the neutron burst time. This energy sets the maximum energy of the region of q, ω space to be observed.

Three experiments were performed, all at 20 K, the first (run 659) using a sample of slab geometry (sample A) at an incident energy of 220 meV, and the second and third (runs 1071,1072) using a cylindrical geometry sample (sample B) at incident energies of 220 and 450 meV respectively. Sample A was supplied by Goodfellow metals at Cambridge. Sample B was manufactured at the University of Warwick (see chapter 4 for details) and its composition was determined to be ZrH_x, $x = 1.96 \pm 0.04$. As with the sample used for the eVS measurements, the presence of the single ϵ-phase in each sample was confirmed by studying the diffraction part of the time-of-flight spectra. Figures 3.1 and 3.2 show respectively the diffraction spectra for samples A and B. Diffraction peaks corresponding to d-spacings of greater than 1 Å have been identified. Aluminium diffraction peaks (from the sample holder) are marked as such; the other indices refer to the diffraction peaks of ZrH_2. The (002) peak is solely due to the presence of ϵ-phase ZrH_2.

Figure 3.3 shows the arrangement of the slab sample with respect to the incident beam. The sample was mounted in an aluminium sample holder, and had approximate dimensions of 50 × 50 × 1 mm. It was mounted with the plane of the sample inclined at 45 degrees to the incident beam. The arrangement of sample B used for runs 1071 and 1072 is shown in figure 3.4. The sample weighed 4.632 grams, and was placed in a rectangular aluminium sachet which was rolled into a cylinder of length 4 cm. This was placed centrally inside an aluminium foil cylinder which was capped at both ends with aluminium end-pieces, attached to a bracket by which the sample was suspended in the beam. Cadmium shielding was used to lessen the scattering from the aluminium sample holder. The axis of the sample was perpendicular to the incident beam direction and in the horizontal plane. The analysis and results of these experiments are detailed below.

It is important to ensure that in the derivation of the vibrational density of states,

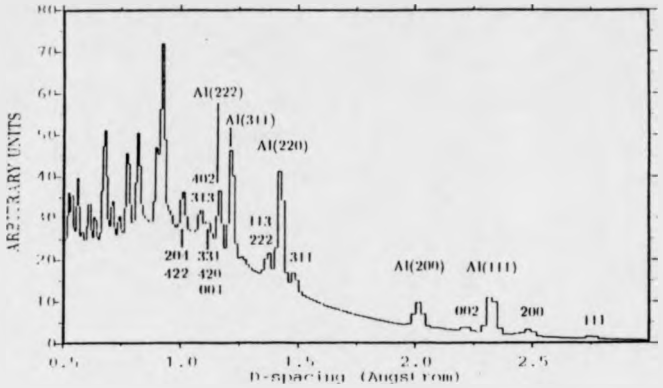

Figure 3.1 The neutron diffraction pattern of ϵ-ZrH_2 powder obtained from Goodfellow Metals Ltd (sample A). All peaks with d-spacings greater than 1 Å have been identified as being either aluminium Bragg peaks from the sample holder or from ϵ-phase ZrH_2.

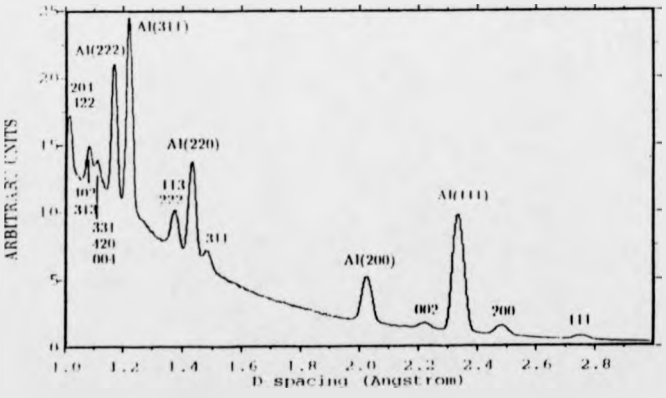

Figure 3.2 The neutron diffraction pattern of ϵ-ZrH_2 powder manufactured at the University of Warwick (sample B). All peaks with d-spacings greater than 1 Å have been identified as being either aluminium Bragg peaks from the sample holder or from ϵ-phase ZrH_2.

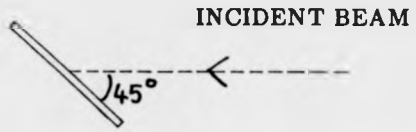

Figure 3.3 The sample geometry for MARI run 659.

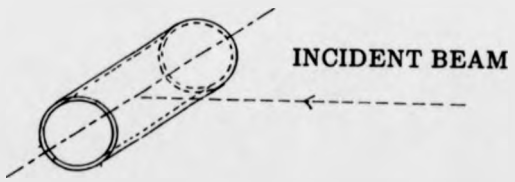

Figure 3.4 This is the sample arrangement used for MARI runs 1071 and 1072. The sample is contained between two concentric aluminium tubes, whose common axis is perpendicular to the incident beam. It is designed to make the scattering isotropic.

multiple scattering does not adversely affect the data at low q. The choice of a cylindrical geometry for the sample reduces self-shielding effects of the sample. Cadmium was used to reduce scattering from the end-caps of the aluminium sample holder. Use of the MSCAT code of Copley [51] was considered to correct for multiple scattering, but this was not done. Peek et al [27] have done so for HRMECS at the Argonne National Laboratory (a direct geometry time-of-flight spectrometer) and found qualitative agreement between the MSCAT calculations and their data (on liquid neon) in that both show a small extra scattering contribution at large energy transfers. They also made the point that MSCAT is most suitable for reactor sources, and maybe not suitable for time-of-flight sources where the spatial dimensions of the sample could affect the final flight time and hence the apparent calculated final energy. There is the advantage, however, that the exact form of the density of states does not affect the form of the neutron Compton profile at large q. The width of the neutron Compton profile should only depend on the mean kinetic energy of the system, and therefore on the density of states via the effective temperature, equation 36. Therefore, so long as any multiple scattering present in these measurements are small, the simulations from the density of states should be representative of the ZrH_2 system.

In figure 3.5, the measurement of $S(q,\omega)$ with sample B for an incident energy of $E_i = 220$ meV is shown. These data are uncorrected for multiple scattering. The region of (q,ω) space accessible by MARI is kinematically limited. The intense feature spread around $\omega = 0$ is the peak due to elastic incoherent scattering. The broad feature at low values of energy transfer, ω , extending out of the range of (q,ω) space is due to the acoustic modes of the sample, the vibrations of the Zr atoms. This feature peaks at around 30 $Å^{-1}$ because of the high mass of Zr (91 amu), so only the low-q tail is observable. The first optical peak due to the vibration of the hydrogen is located at around 140 meV and is highly structured. It is from this feature that the density of states is calculated. Figure 3.6 shows the measurement with sample B for $E_i = 450$ meV. For incident neutrons of this energy, the first, second and third excited states are reached, so the first, second and third optical peaks are visible.

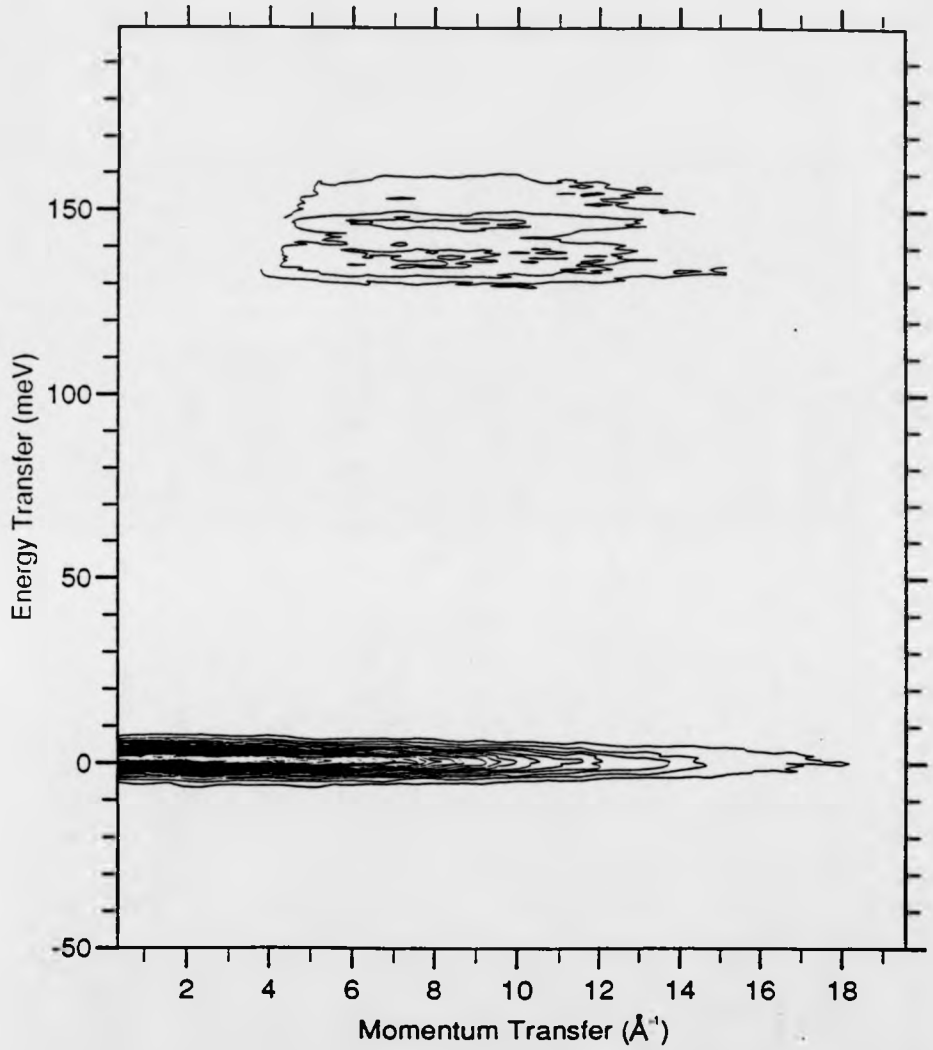

Figure 3.5 The raw $S(q,\omega)$ data of sample B (run 1071) collected on the MARI spectrometer. The sample had cylindrical geometry and the energy of the incident beam was 220 meV. The density of states of the hydrogen vibrations is extracted from the first optical peak, seen here centred at about 140 meV. The intense peak centred at zero meV and extending to high q is the elastic peak.

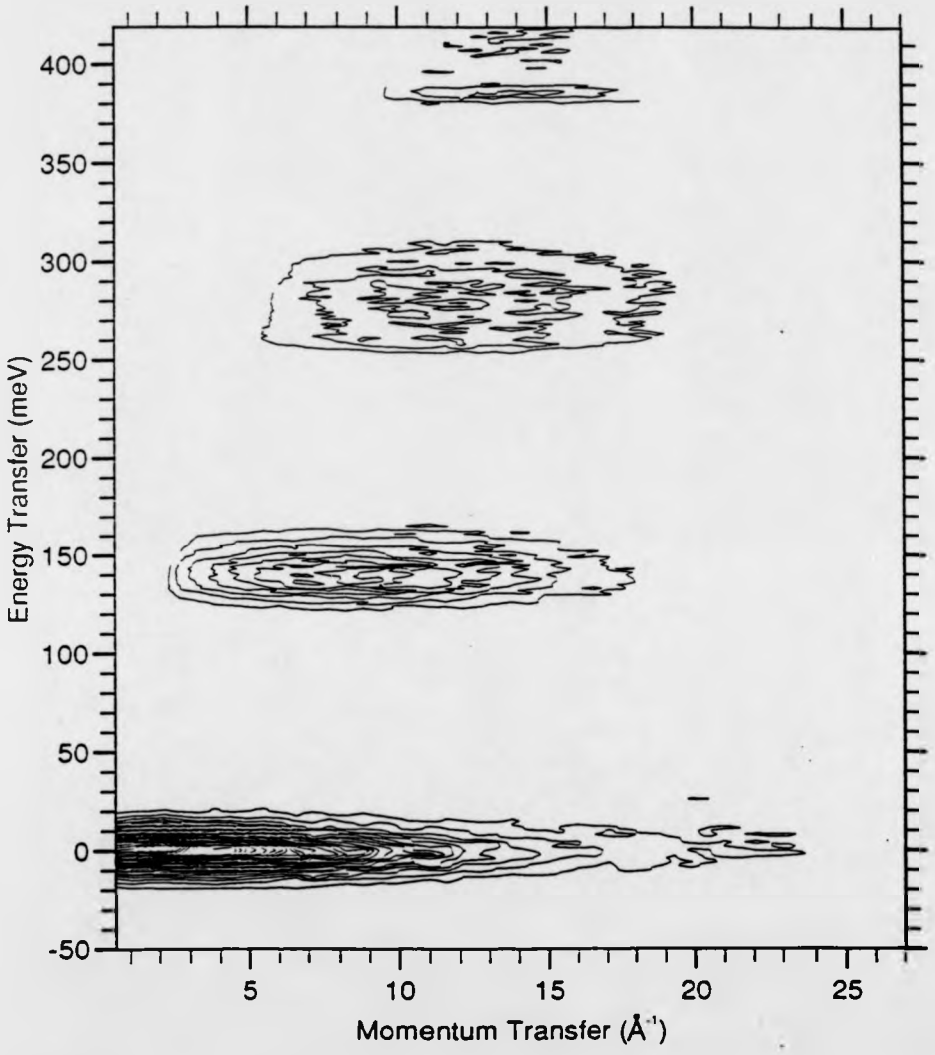

Figure 3.6 The raw $S(q,\omega)$ data of sample B (run 1072) collected with the MARI spectrometer. The energy of the incident beam was 450 meV. At this incident energy, the first, second and third optical peaks are visible.

3.3 DERIVATION OF THE VIBRATIONAL DENSITY OF STATES

For an isotropic system, the single particle incoherent scattering in the harmonic approximation is given by [5]

$$S_H(\mathbf{q},\omega) = [1/(2\pi\hbar)]\int_{-\infty}^{\infty} dt \exp(-i\omega t)\exp(\hbar q^2/2M)[\gamma(t)-\gamma(0)] \tag{83}$$

where

$$\gamma(t) = \int_{-\infty}^{\infty} d\omega[g(\omega)/\omega]n(\omega)\exp(-i\omega t). \tag{84}$$

The one-phonon contribution to $S_H(q,\omega)$ can be obtained from equation 83 by expanding the exponential term $\exp(-i\omega t)$ and is given by [5]

$$S_{H,+1}(\mathbf{q},\omega) = \frac{1}{2M}q^2\exp[-2W(\mathbf{q})]\frac{g(\omega)}{\omega}[n(\omega)+1] \tag{85}$$

where the subscript $+1$ refers to one-phonon scattering and $\exp(-2W(\mathbf{q}))$ is the Debye-Waller factor. For a cubic Bravais lattice, $W(\mathbf{q})$ is given by

$$W(\mathbf{q}) = \frac{\hbar^2 q^2}{4M\omega_0}\coth\left(\frac{\omega_0}{2T}\right). \tag{86}$$

At $T = 0$ this leads to the result

$$2W(\mathbf{q}) = \frac{q^2}{4\sigma^2} \tag{87}$$

$g(\omega)$ is the normalised phonon density of states and $n(\omega)$ is the Bose-Einstein occupation factor

$$n(\omega) = [exp(\hbar\omega/k_BT)-1]^{-1} \tag{88}$$

where k_B is Boltzmann's constant.

At low q, $S(q,\omega)$ is dominated by one-phonon scattering. This means that equation 85 can be used to derive the density of states. Following the method used by Andreani et al [52] for a polycrystalline sample, the density of states $g(\omega)$ is given by

$$g(\omega) = \lim_{q\to 0} g'(q,\omega) = \frac{S_{H,+1}(q,\omega)}{q^2}2M\omega\frac{\exp 2W(\mathbf{q})}{[n(w)+1]} \tag{89}$$

The value for $W(\mathbf{q})$ was determined via equation 87 using a value of $\sigma = 4.18$ Å determined by the eVS measurement presented in chapter 4. The data provided from

the MARI analysis give a rectangular grid of values of $S(q,\omega)$. A series of constant-ω cuts were made at intervals of between 0.5 and 1.0 meV. Each of the data sets so obtained was converted to a value defined here as $g'(\omega,q)$. By extrapolating $g'(\omega,q)$ to $q = 0$ for each value of ω, and normalising to unity, $g(\omega)$ was obtained. A weighted least-squares straight-line fit was used to perform the extrapolation. An example of an extrapolation is shown in figure 3.7. The crosses in the figure are the transformed data at ω = 146 meV. The extrapolated value is the intercept of the fitted straight line. Once the extrapolated values were obtained in the region 100 to 200 meV, they were normalised to unity. Figure 3.8 shows the derived density of states, corresponding to MARI runs 659 (circles) and 1071 (boxes). The density of states in figure 3.9 has poorer resolution than those in figure 3.8 because the measurement was performed for a high incident energy. It is compared (boxes) to the other two density of states measurements (lines). The run 659 measurement has the best counting statistics and it is this density of states that has been used for the calculations of the simulations of eVS data. As noted by Andreani et al [53], if the q-range of the data does not extend sufficiently close to zero, and large multi-phonon terms are present, the extrapolation may introduce errors.

3.3.1 Interpretation of the density of states

The localised H vibrations are split according to the symmetry of the tetrahedral interstitial site, the lower one being doubly degenerate. The latter is due to the vibration of the bound proton in the [100] and [010] directions (see figure 4.2) and the non-degenerate mode is due to the vibration along the [001] direction. Since $c < a$, the double-degenerate modes occur at a lower frequency (energy) than the [001] mode. This is in agreement with elementary considerations: if the force constant for a harmonic displacement of the bound proton is inversely proportional to the separation of neighbouring Zr atoms then the optic splitting is given by [54]

$$\left(\frac{c}{a}\right)^{\frac{1}{2}} = \frac{\omega_E}{\omega_A} \qquad (90)$$

where c and a are the usual structural lattice parameters and the oscillator transi-

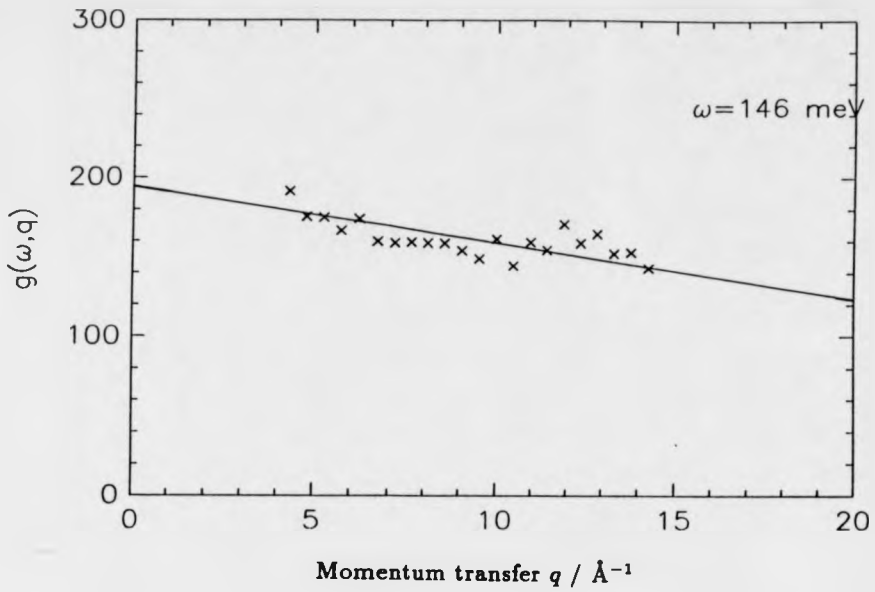

Figure 3.7 The extrapolated function $g(q,\omega)$ as a function of momentum transfer and at $\omega = 146$ meV. The data points $(+)$ are obtained from the first optical peak of $S(q,\omega)$ through equation 89.

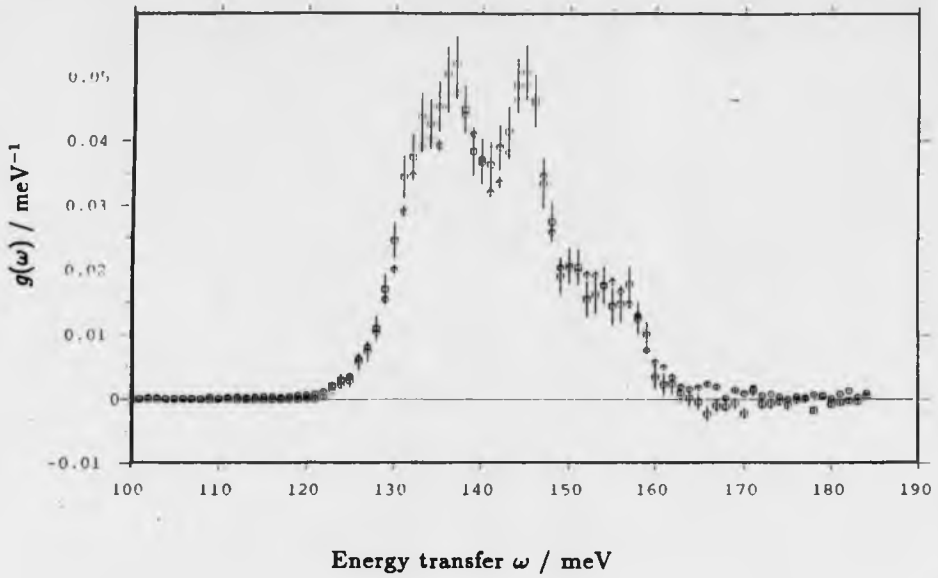

Figure 3.8 The vibrational density of states of H in ZrH_2 obtained from MARI run 659 of slab geometry (circles) and run 1071 of cylindrical geometry (boxes). Both runs were made with an incident energy of 220 meV. The similarity of the derived density of states for these two different geometries indicates that multiple scattering effects are small.

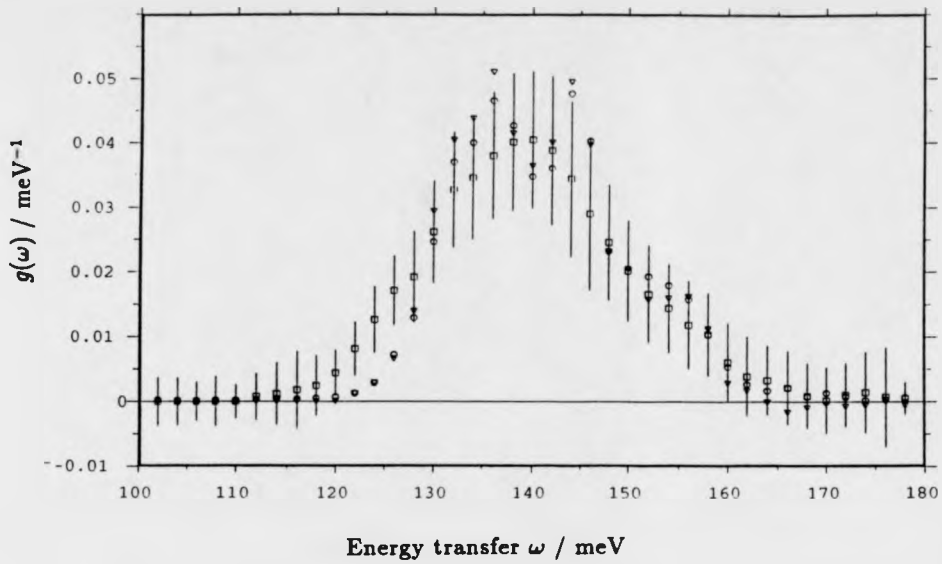

Figure 3.9 The vibrational density of states of H in ZrH_2 obtained from MARI run 1072 (boxes) (with an incident energy of 440 meV) against those from run 659 (circles) and run 1071 (triangles). The energy resolution of run 1072 is poorer because of the higher energy.

tions occur at $\omega_{A,E}$. A and E indicate non-degenerate and doubly-degenerate states respectively.

The density of states determined from run 659 has peaks at 136.81 ± 0.16 meV, 145.67 ± 0.12 meV, and a broad feature centred at 153.13 ± 0.40 meV. The peak positions were located by using a multiple-Gaussian fitting package FRILLS [55]. The fit is shown in figure 3.10. An attempt to fit to the fine structure in the 137 meV double peak was unsuccessful. Using the values for c (4.45 ± 0.01 Å) and a (4.98 ± 0.01 Å) from reference [56], the ratio ω_E/ω_A is 0.945 ± 0.002, compared to 0.939 ± 0.002 from the fitted peak positions. The 0.6% difference in these values may be due to the splitting of the doubly-degenerate peak at 137.0 meV into two peaks. The splitting may be due to hydrogen-hydrogen interactions. The ratio of the intensity of the double peak at 137 meV to the intensity of the 146 meV peak should be 2.0. The simple Gaussian fit gives a value of 3.7. This may be because of the poor fit to the broad feature at 153 meV, which could steal intensity away from the middle peak in this simple fit.

3.4 NUMERICAL CALCULATION OF $S(q,\omega)$

The eVS data were simulated using a modification of a FORTRAN program [9] written to calculate the dynamic structure factor for neutron scattering from a harmonic system $S_H(q,\omega)$ exactly from the density of states using equations 83 and 84. Three banks of detectors are identified in figure 2.10 as 'bank A', 'bank B' and 'bank C', and contain 10 detectors each, with scattering angles between 36° to 44°, 46° to 54° and 57° to 66° respectively. Three measured neutron Compton profiles were created by adding the data in each of these banks, each one sampling the recoil peak over a different range of momentum transfers. The time-of-flight difference spectra were simulated for each eVS detector using the calibration parameters introduced in chapter 2 to relate a point in $S(q,\omega)$ to a point in time-of-flight. The data were then convoluted with the resolution function, as explained in chapter 2, and converted to momentum space. The data were analysed in the same way as the 'real' eVS data, the only difference being that the calculated time-of-flight spectrum was not divided through by $E_0^{0.1}$ since the

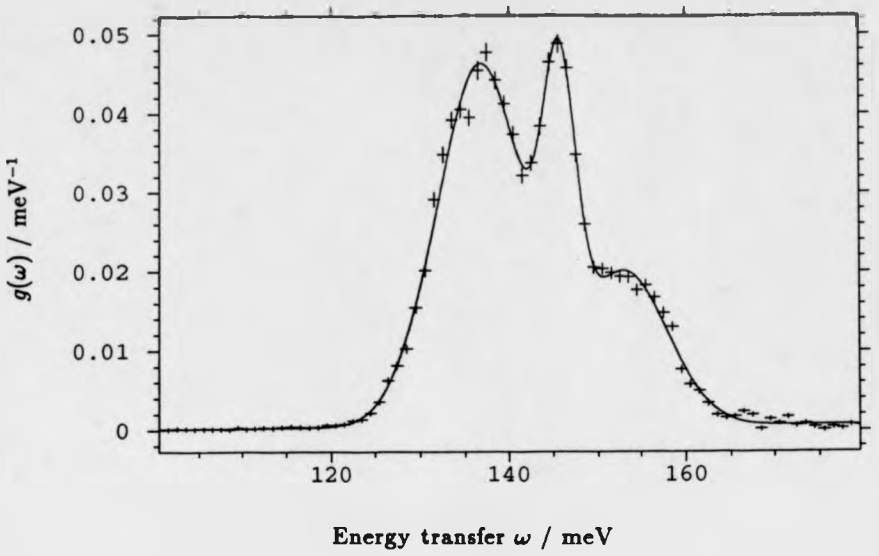

Figure 3.10 The multiple Gaussian fit to the density of states determined from MARI run 659 (solid line) is compared to the data (+). The fit was performed with the FRILLS package [54]. See the text for the fit parameters.

starting point was a theoretical $S(q,\omega)$ and not some physical measurement. A value of 140 meV was used for the full-width at half maximum of the empirically Lorentzian resolution contribution from the analyser foil. Figure 2.1 shows the regions of (q,ω) space scanned by the three banks. Simulations for detectors 11 and 20 are shown in figure 3.11, at scattering angles of 35.96 and 53.68 ° respectively. The individual multiphonon excitations are visible. At the higher momentum transfers reached at 53.68 ° the individual excitations merge together. The data shown are not resolution convoluted. As shall be seen, even for the lowest scattering angle, there is no sign of the individual excitations after convolution with the resolution function.

3.5 COMPARISON OF MARI AND eVS RESULTS

Many measurements on the ZrH_2 system have been made on eVS. The eVS measurements used in this study were performed at both 20 and 290 K. The hydrogen atoms are nearly always in the ground state at both these temperatures and so data at the two temperatures can be added together. There is confirmation of this from simulations that have been performed at both temperatures. Furthermore, ZrH_2 exists in the ϵ-phase at both these temperatures. In these measurements, the powdered sample was contained inside an aluminium sample holder of slab geometry, and this was placed perpendicular to the incident beam. To ensure that the neutron detectors were not saturated, the total scattering was limited to approximately 5 % of the incident beam.

The results of the simulations over the three ranges of momentum transfer are compared to eVS measurements in figures 3.12 to 3.14. y-scaling was used to convert the time-of-flight data to momentum space. In figure 3.12, the measured neutron Compton profiles of the ten eVS neutron detectors in bank A have been summed and normalised to unity. These detectors sample the recoil peak at momentum transfers between 35.3 and 46.6 $Å^{-1}$ and at a mean momentum transfer of 40.8 $Å^{-1}$. The simulation based on the measured vibrational density of states of figure 3.8 (circles) is shown as a continuous line. Also shown (dotted line) is the result expected in the IA, which is centred at $y = 0$.

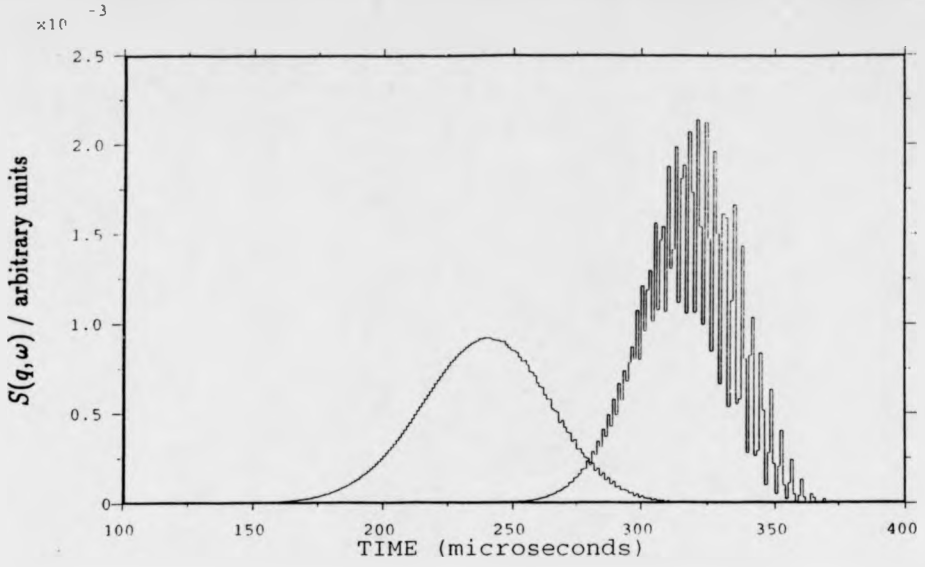

Figure 3.11 Simulations of eVS time-of-flight spectra for scattering from hydrogen in ZrH_2. The simulations are based on the measurement of the vibrational density of states determined from MARI run 659 (shown in figure 3.8) and are an exact numerical simulation in the harmonic incoherent approximation. The simulations shown are for detectors 11 and 20 at scattering angles of 35.96 and 53.68 °. The individual multiphonon excitations are visible in the peak centred at about 310 μs. At the higher momentum transfers reached at 53.68 ° the individual excitations merge together. The data shown are not resolution convoluted.

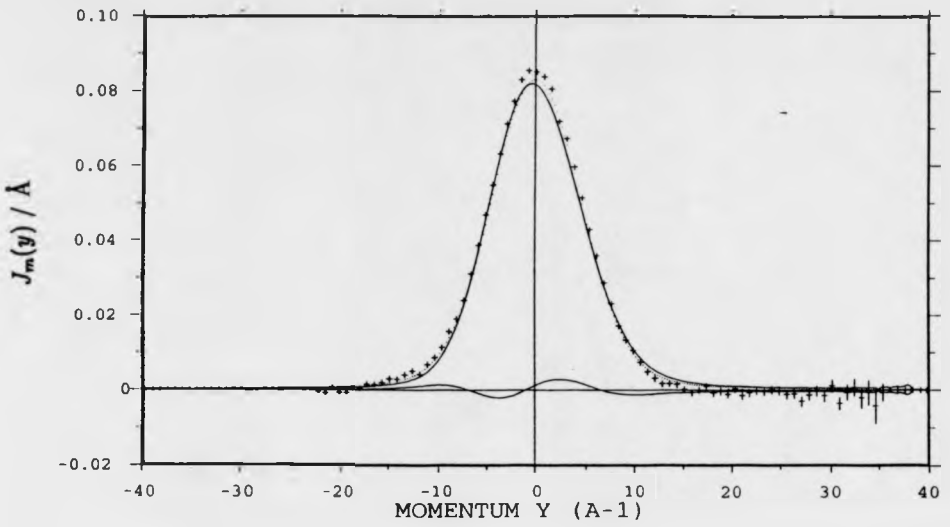

Figure 3.12 A comparison of a measurement of $J_m(y)$ made at an average momentum transfer of 40.8 $Å^{-1}$ on eVS (+) compared to an exact simulation of the data based on the density of states of the hydrogen vibrations measured with the MARI spectrometer (solid line). Also shown is the result obtained in the impulse approximation (dotted line) and the difference between this and the simulation (lower solid line). y-scaling has been used to convert from time-of-flight to momentum-space.

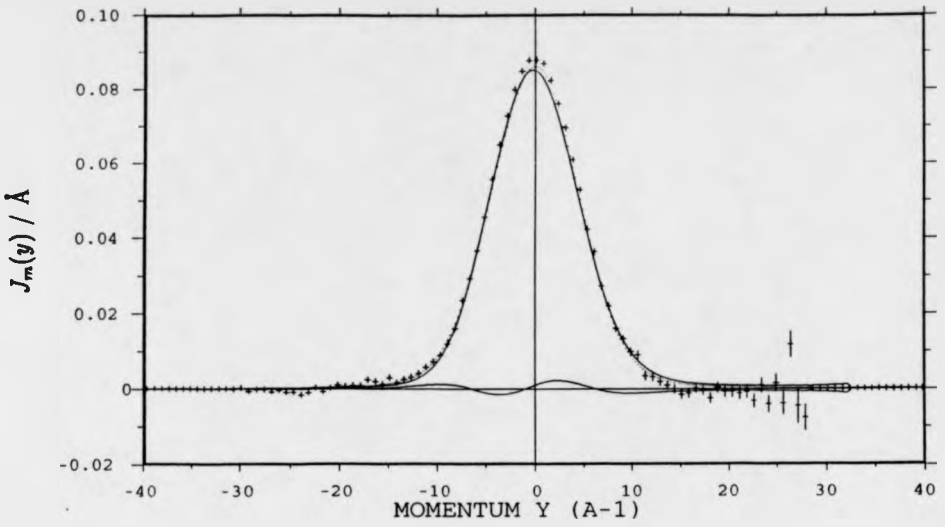

Figure 3.13 As figure 3.12 except made at an average momentum transfer of 57.6 $Å^{-1}$.

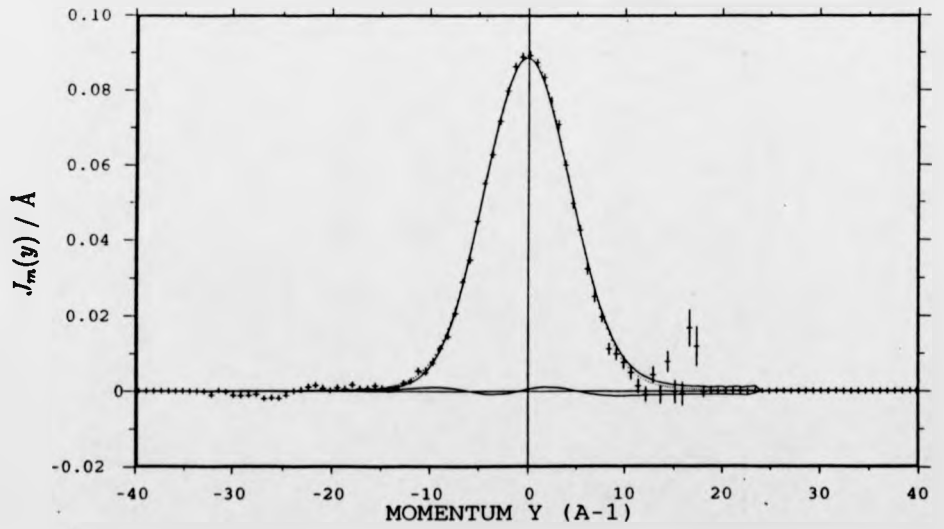

Figure 3.14 As figure 3.12 except made at an average momentum transfer of 91.2 $Å^{-1}$.

Three measurements of the Goodfellow metal ZrH_2 sample have been added together and are represented by the crosses (+). The difference between the simulation and the IA result is shown as the lower solid line, and is due to final-state effects. Both the simulation and the eVS data show an asymmetry. The peak position of the simulation is shifted to negative values of momentum space, as expected at finite values of q and can be attributed to final-state effects. Figure 3.13 for bank B samples the recoil peak at momentum transfers between 50.0 and 65.8 $Å^{-1}$ and a mean momentum transfer of 57.6 $Å^{-1}$. Figure 3.14 is for eVS detectors in bank C and sample the recoil peak at momentum transfers between 75.7 and 108.6 $Å^{-1}$ and at a mean momentum transfer of 91.2 $Å^{-1}$.

Figures 3.15 to 3.17 correspond to figures 3.12 to 3.14 except that the Stringari $y1$-scaling variable has been used to convert from time-of-flight to momentum space. The difference is clear. The measured neutron Compton profiles are distinctly more asymmetric than the y-transformed data.

To demonstrate the approach to the IA, the peak position of the measured neutron Compton profile of each detector is determined. The resulting values cover a range of q. The peak position of the measured neutron Compton profile coincides with the neutron Compton profile because of the empirically symmetric resolution function. Figure 3.18 shows the peak shifts in the y-scaled eVS data plotted against a dashed line showing the derived peak shifts of the simulated data.

Figure 3.19 shows the fitted values for σ, the mean kinetic energy, as a function of q for the eVS data (circles), and the results obtained from the simulation (dashed line).

3.6 DISCUSSION

Run 659 was measured with a sample of slab geometry, whilst run 1071 was made with a sample of cylindrical geometry. The similarity between the density of states derived from MARI runs 659 and 1071, shown in figure 3.8, indicates that multiple scattering effects are small. The dependence of σ on the form of the density of states is

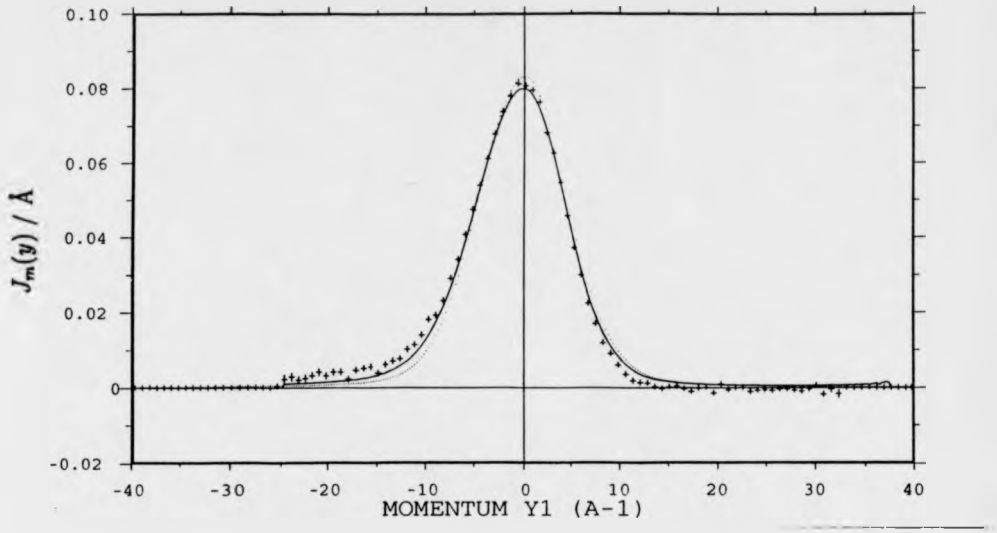

Figure 3.15 A comparison of a measurement of $J_m(y)$ made at an average momentum transfer of 40.8 $Å^{-1}$ on eVS (+) compared to an exact simulation of the data based on the density of states of the hydrogen vibrations measured with the MARI spectrometer (solid line). Also shown is the result obtained in the impulse approximation (dotted line) and the difference between this and the simulation (lower solid line). $y1$-scaling has been used to convert from time-of-flight to momentum-space.

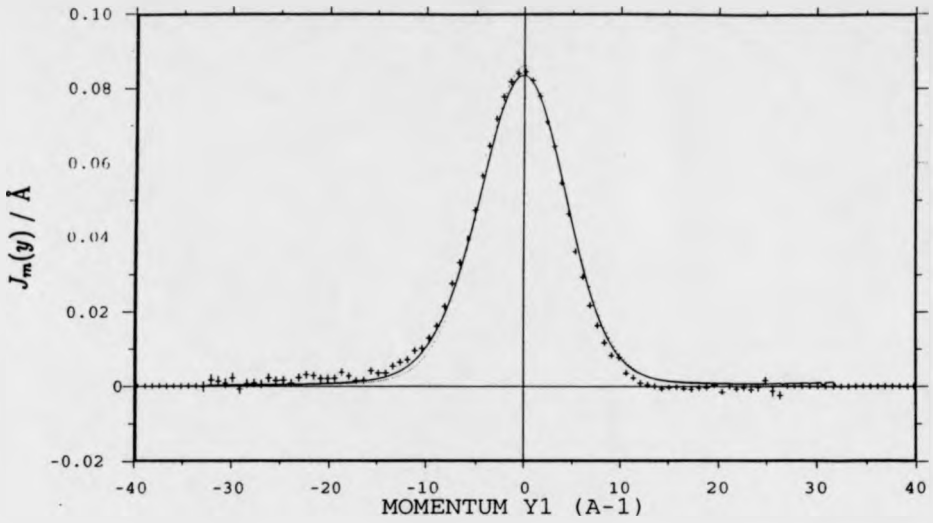

Figure 3.16 As figure 3.15 except made at an average momentum transfer of 57.6 Å^{-1}.

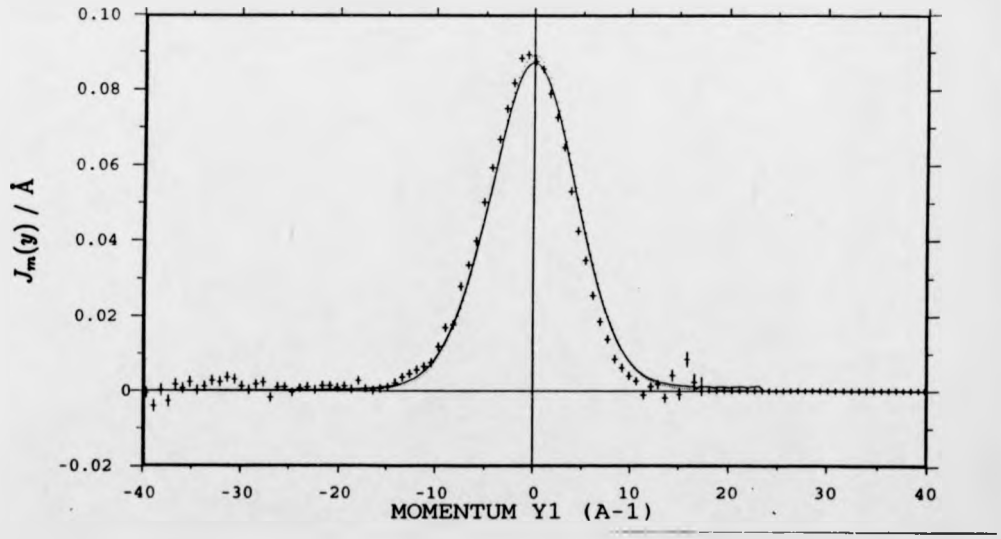

Figure 3.17 As figure 3.15 except made at an average momentum transfer of 91.2 Å^{-1}.

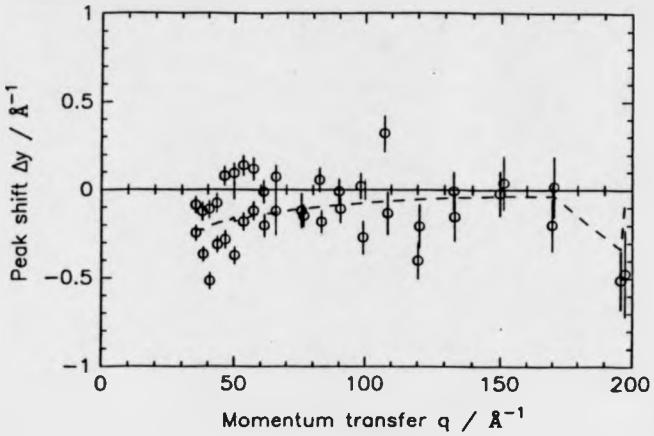

Figure 3.18 The positions of the recoil peaks in y-space are shown for the sum of three eVS measurements (circles) as a function of the momentum transfer of the measurements. Also shown (dashed line) is the same for the numerical simulation.

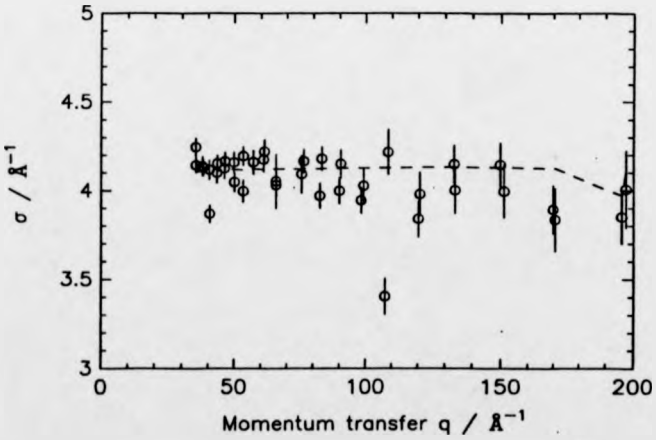

Figure 3.19 The eVS σ valued determined from the sum of three eVS measurements (circles). They are plotted against the σ values determined from the numerical simulation from the density of states.

demonstrated by repeating the simulations for ZrH_2 using a slightly different density of states. Figure 3.20 shows the density of states used to perform the above simulations (triangles) compared to a similar density of states (circles) obtained in a preliminary analysis of the MARI data. Using equation 33, values of 4.14 $Å^{-1}$ and 4.17 $Å^{-1}$ respectively are obtained. From the unsymmetrised y-transformed simulations (figures 3.12 to 3.14) a mean value of 4.1235±0.0018 is obtained from the 'correct' density of states, whilst from the similar density of states, a value of 4.141 ± 0.0019 is obtained. The difference in these values (1 %) indicates the sensitivity of the derived σ value to the mean value of the density of states used in the simulations. The precise form of the density of states, however, has little bearing on the simulations.

The sensitivity of the determined σ values on the half-width at half-maximum of the Lorentzian contribution to the resolution function was determined by repeating the y-transformed simulations using values of $\Delta E = 126$ and $\Delta E = 140$ meV. For the hydrogen simulations, the two analyses gave values of 4.1464±0.0018 and 4.1235±0.0018 respectively, a difference of about 0.75 % or just under 1.44 % in the mean kinetic energy. This is comparable to the statistical accuracy of the measurement, and so is not of great significance. In these analyses, a value of $E_R = 140$ meV is used consistently. The uncertainty in this parameter is indicated by the values given in table 2.3b.

The peak shifts of the y-transformed simulations and eVS data, figures 3.14 to 3.16, become smaller as the momentum transfer is increased, in accordance with the limiting behaviour of the IA. This can be seen visually in figures 3.14 to 3.16. The solid line at the bottom of each plot is the difference between the result in the IA and the simulation. It becomes flatter from figure 3.14 to 3.15 and again from figure 3.15 to 3.16. Figure 3.18 demonstrates this more clearly, and shows the difference in peak shift between the simulations and the eVS data. Figure 3.21 shows the low momentum transfer data shown in figure 3.18. At high momentum transfers, the high energy tail of the neutron Compton profile corresponds to very short times of flight where the neutron detectors seemed to be noisy. This region is typically below 100 μs. This means that for detectors 36 to 40 and detectors 46 to 50, the analysis gives unreliable

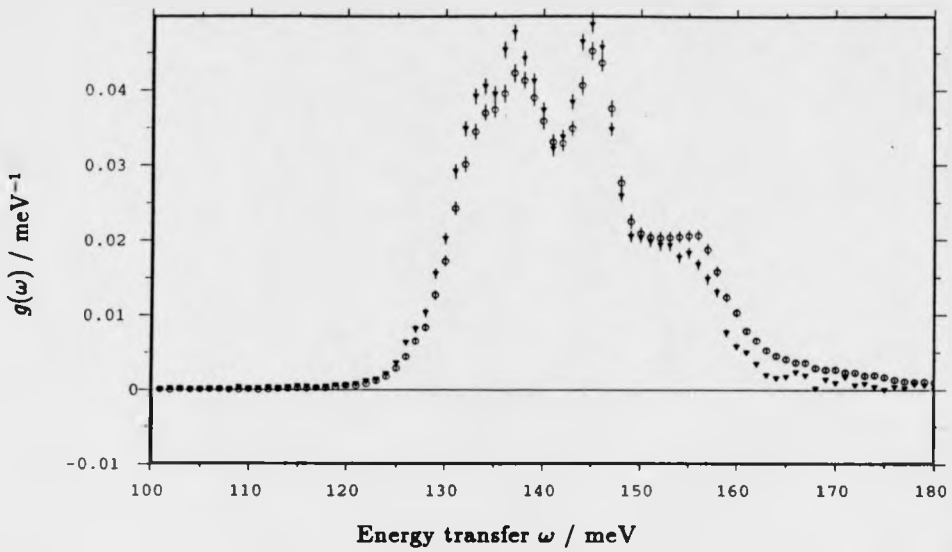

Figure 3.20 The density of states derived from MARI run 659 (triangles) and used to simulate eVS measured neutron Compton profiles in chapters 3 and 4. It is compared to a previously (and erroneously) calculated density of states. The small difference in mean kinetic energy determined from these two similar densities of states demonstrates the weak dependence of the determined mean kinetic energy on the exact form of the density of states.

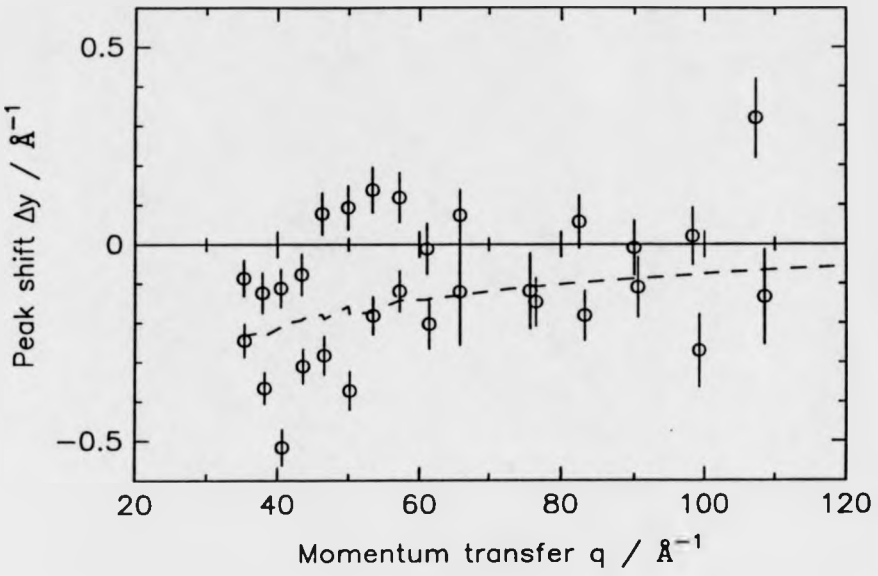

Figure 3.21 A detail of figure 3.18 in the range 20 to 120 Å^{-1}. The simulation (dashed line) clearly indicates the movement of the fitted peak position towards the impulse approximation result at higher q. The eVS data also show this tendency.

values for σ. These detectors correspond to points with $q > 110$ Å^{-1} in figure 3.18. Both the simulation and the eVS data in this region show some systematic deviation in the fitted peak shift. The presence of a systematic error in the simulated peak shift over this range is due to problems in calculating the time-of-flight spectra at very short times of flight. This is visible in figure 3.14 for example, at $y > 20$ Å^{-1}.

3.7 SUMMARY

The presence of final-state effects introduces an asymmetry into the measured neutron Compton profile and leads to a value of σ smaller than predicted from the density of states. The solution is to symmetrise the measured neutron Compton profile. There are good physical arguments for this procedure. The momentum distribution must be symmetric. The particle would otherwise be moving through the solid. Furthermore, symmetrisation removes final-state effects of order q^{-1}, as explained in chapter 2. Chapter 4 explains that final-state effects in these eVS data are sufficiently small to be dealt with effectively in this way. This procedure was carried out with the simulated measured neutron Compton profiles and the eVS measured neutron Compton profiles. The σ values obtained are typically 1 % larger than the unsymmetrised data. For the simulations, the extracted values of σ agree within error with the σ values determined from the measured density of states, indicating that the symmetrisation procedure is a worthwhile procedure to follow.

The $y1$-transformed data leads to an overestimate of the mean kinetic energy. Mayers [8] makes the point that the procedure violates the second sum rule for incoherent scattering. It is nevertheless useful to know that the y-scaling scheme leads to a significantly more acceptable measured neutron Compton profile in terms of asymmetry.

For a deeper understanding of final state effects, it is desirable to look for directional dependence in single crystals. A previous DINS study of the impulse approximation in single-crystal beryllium [57] has suggested that final-state effects were more significant in the basal plane of the beryllium, where the atoms are closer together. Currently, eVS has a greatly improved count-rate (with the introduction of Li-glass scintillation

detectors to replace the ^{3}He neutron detectors). Such an experiment should now be feasible.

CHAPTER 4

The neutron Compton profiles of polycrystalline $ZrH_{1.96}$, $ZrD_{2.00}$, $NbH_{0.95}$ and $NbD_{0.98}$

This chapter presents the measured neutron Compton profiles $J_m(y)$ of interstitial hydrogen (deuterium) in the ordered phases of the hydrides and deuterides of niobium and zirconium. Samples of polycrystalline $ZrH_{1.96}$ and $ZrD_{2.00}$ in the ordered ϵ-phase, and polycrystalline $NbH_{0.95}$ and $NbD_{0.98}$ in the ordered β-phase were manufactured at the University of Warwick, and their neutron Compton profiles were measured on the Electron Volt Spectrometer (eVS) at room temperature and pressure. The vibrational density of states of the $ZrH_{1.96}$ system presented in chapter 3 was used to perform exact numerical calculations of the measured neutron Compton profile $J_m(y)$ for this system. The calculation works in the incoherent harmonic approximation. Numerical calculations of the $ZrD_{2.00}$ system were made from the vibrational density of states for the deuteride system. The deuteride density of states was calculated from the hydride vibrational density of states with the assumption that the interstitial atoms in each system are bound by the same potential. The calculated measured neutron Compton profiles of the hydride systems are compared to the measured neutron Compton profiles for four ranges of momentum transfer between 35.4 $Å^{-1}$ and 213.6 $Å^{-1}$ and the $J_m(y)$ for the deuterides are compared for four ranges between 36.0 and 76.9 $Å^{-1}$. In the case of the niobium systems, the data are compared to inelastic neutron spectroscopy measurements. It is shown that for x^3 and x^4 perturbations to a harmonic oscillator, the procedure used in the eVS analysis of considering $J(y)$ to be Gaussian is valid. The relationship between the $0 \rightarrow 1$ transition energy ω and σ, the variance of $J(y)$ is determined for this potential and working within the impulse approximation, the exact form for the neutron Compton profile is determined. A summary of some of the relevant work on metal hydride systems is given below.

4.1 INTRODUCTION

Metal hydrides and deuterides have been the subject of many investigations for two reasons. First, they are of technological importance. The penetration and embrittlement of metals by hydrogen and its isotopes is a serious problem in industry, and hydrides and deuterides can store these two gases efficiently, and this is useful for technical systems using hydrogen as a chemical fuel. Second, metal hydrides are useful systems for the study of the behaviour of interstitials in metals, fundamental aspects of phase transitions, diffusion, electronic and other properties of metals. (For a compilation of a variety of studies of hydrogen in metals, see Hydrogen in Metals I [58].) The ability to measure directly momentum distributions of nuclei offers exciting prospects for many areas of physics. For example, until recently inelastic neutron spectroscopy (INS) was the only tool available for the study of the vibrations of hydrogen or deuterium absorbed in heavy metals ([58] chapter 4). The dynamics of hydrogen or deuterium is of great interest as it is linked to the physical properties of such systems, for example superconductivity, electronic properties and hydrogen diffusion and there is much experimental work in this field.

Neutron scattering has been used extensively to study metal hydrides and deuterides. As long ago as 1968, Somenkov [59] used neutron diffraction to determine the structure and phase transitions in the Nb-H and Nb-D systems and demonstrated that interstitial H/D atoms in the low temperature β-phase form a sublattice and occupy tetrahedral interstitial sites. Inelastic neutron spectroscopy offers a way of measuring the energies of the vibrational modes of interstitial hydrogen in metal hydride systems (see chapter 4 of [58], and for studies of the Nb-H/D systems, references [60, 61, 62], for studies of the Zr-H/D system, references [63, 64]), and has provided a great deal of information about the hydrogen potential, which is strongly dependent on the chemical and topological environment around the hydrogen atom. Richter and Shapiro [63] used inelastic neutron scattering to study the energy levels of interstitial hydrogen and deuterium in β-phase $NbH_{0.85}/NbD_{0.85}$. They identified a higher harmonic of an H/D vibration in a bcc metal for the first time, demonstrating that the diffusive process is not simply the

motion over a barrier provided by the vibrational potential. There have been several other recent studies where INS has been used to investigate the local H/D potential in metal hydride/deuteride systems [19, 65]. However, the momentum distribution, or the mean kinetic energy cannot be directly observed by inelastic neutron spectroscopy. In the case of solid neon, the problem of determining the vibrational density of states (and therefore the mean kinetic energy) from such data has been discussed by Peek et al [27]. To deduce a vibrational density of states, a Born von Karman model of the lattice dynamics is applied, involving assigning force-constants to the nth nearest neighbour atoms. Peek et al state that in such work on solid neon that they have reviewed, the force-constants are not assigned in a rigorous manner, and so the mean kinetic energy may be dependent on the model used. DINS does not suffer from this weakness of model dependence.

DINS offers a way of directly observing the momentum distribution. For DINS from metal hydrides and deuterides, the signals from the metal component and from the aluminium sample can are easily distinguished from the scattering from hydrogen and deuterium, allowing for easier interpretation of the data. In the case of scattering from hydrogen, the scattering cross-section is very large ($\sim$ 80 barns for a proton) and the H and D signals are generally well separated from the signals of the heavier components in the TOF spectra.

The motivation for this study is to demonstrate that neutron Compton scattering is a reliable way of observing the mean kinetic energy in metal hydrides and deuterides and the assumption that the momentum distribution is Gaussian is a valid one, even for strongly anharmonic vibrations. The mean kinetic energy for the four systems is compared in a rigorous way to inelastic neutron spectroscopy measurements using two different methods.

$J_m(y)$ and σ are presented for polycrystalline metal hydrides and deuterides, and compare the results to values determined from inelastic neutron spectroscopy measurements. In the case of the Nb-H/D systems, the ground-state vibrational energies are split into two distinct modes, one doubly degenerate and one non-degenerate mode.

A polycrystalline value from these data is calculated working within the impulse approximation. In the case of the Zr-D and Zr-H systems, a different approach is used working from the ZrH_2 vibrational density of states, the derivation of which is presented in chapter 3. $J_m(y)$ are calculated for a harmonic scatterer in the incoherent approximation and the eVS analysis procedures are used to obtain σ as for experimental data. In this method, the impulse approximation is not used.

4.1.1 The neutron Compton profile in polycrystalline materials

Warner, Lovesey and Smith have performed exact theoretical studies of the dynamic scattering function $S(q,\omega)$ for the case of a mixed harmonic solid containing two masses M and m [29]. They show that for $m \ll M$, (light atoms in a heavy lattice) the vibrational density of states of the system splits into two distinct parts. At low energy, there is a broad spectrum that is proportional to ω^2 for $\omega \rightarrow 0$ and arises from the vibration of the heavy lattice particles. The second component arises from the vibrations of the light particles and is centred at an energy large compared with the Debye cut-off energy ω_D of the lattice with a width small compared to ω_D. This is the oscillator band. The light atoms are allowed to oscillate with frequencies in a very narrow range, i.e. this is a localised state. The vibrations of the light atoms can therefore be considered to arise from the confinement of the light atom in a harmonic potential. In the case of well separated bands, the oscillator band can then be used to calculate the incoherent dynamic scattering function, from which the neutron Compton profile is derived directly.

This is the justification for the separation of the vibrations of interstitial hydrogen into three independent local harmonic modes. Then, σ for a polycrystalline sample will be an average of the ground-state values σ_i, where $i = 1,2,3$ for the three principal directions in the lattice:

$$\sigma^2 = \frac{1}{3}(\sigma_1^2 + \sigma_2^2 + \sigma_3^2). \qquad (91)$$

and $\sigma_i = \left(\frac{M\omega_{0i}}{2\hbar^2}\right)^{\frac{1}{2}}$ for a one dimensional harmonic oscillator. Here, ω_{0i} is the 0→1 transition energy of the vibrational mode, $\hbar$ is Planck's constant (2.04458 (meV amu)$^{1/2}$

Å), M is the mass of the particle in the well, and it is assumed that the particle is confined to the ground-state. This is a reasonable assumption for metal hydrides (deuterides) at and below room temperature since the energy between transitions is typically 100 meV and the probability ($\propto \exp(-E/2T)$) of higher levels being occupied is very low. For example, at 20K the probability of the proton being in the second excited state in ZrH_2 is about $\exp(-70)$. The optic mode energies can be measured by inelastic neutron spectroscopy, and so this provides a way of checking DINS data. We measure σ_D and σ_H in metal hydrides and deuterides of the same structure. For harmonic vibrations, and assuming that the force constants k_i are the same for both a proton and a deuteron,

$$(\sigma_{Di}/\sigma_{Hi})^2 = \sqrt{\frac{M_D}{M_H}} \tag{92}$$

where the subscripts D and H refer to the deuteride and hydride and M_D and M_H are the masses of a proton and a deuteron.

The above relationship between ω and σ is true for a harmonic oscillator, but it is known that for many metal hydride systems, there is clear evidence of anharmonicity [63, 64]. In the impulse approximation, $J(y)$ for a harmonic potential with a strong x^4 and x^3 perturbation can still be accurately represented by a Gaussian function (making data analysis simpler). The relationship between σ and ω_1, the perturbed energy eigenvalue of the ground state, is derived for such a perturbation. It is shown that equation 92 is still correct in this case.

4.1.2 Anharmonic perturbation theory

Considering a perturbation to the harmonic potential of the form $c_2x^2 + c_4x^4$, then the application of time-independent perturbation theory shows that ω is shifted by an amount

$$\omega_1^{H(D)} = \omega - \frac{2\beta}{M^{H(D)}} \tag{93}$$

where $\beta = -\frac{3}{2}\frac{\hbar^2 c_4}{c_2}$, $M^{H(D)}$ is the mass of the bound proton (deuteron) and c_2 is the harmonic force constant. An analytic expression for the perturbed ground-state kinetic

energy has been derived:

$$\frac{\langle p^2 \rangle}{2M^{H(D)}} = \frac{\omega}{2} f(\gamma) \tag{94}$$

where

$$f(\gamma) = \frac{\frac{1}{2} + \frac{59}{48}\gamma_1^2 + \frac{135}{64}\gamma_2^2 + \frac{3}{2}\gamma_2}{1 + \frac{29}{24}\gamma_1^2 + \frac{39}{32}\gamma_2^2} \tag{95}$$

and p is the momentum of the particle, $\langle ... \rangle$ denotes an expectation value, and

$$\gamma = -\frac{2\beta}{3\omega M^{H(D)}}. \tag{96}$$

The probability distribution in momentum space, p, was calculated (see appendix 1 for full calculation), and the kinetic energy was calculated from the second moment and compared to the analytic expression for a range of β in order to check the code for errors. Agreement between the two was exact to 5 or 6 decimal places. It was noticed that a perturbation of the order typically found in metal hydride systems ($\beta/M \simeq 3$ meV) the momentum distribution (equation 114 in appendix 1) was very well approximated by a Gaussian. Figure 4.1 shows the ground-state momentum distribution, $n(p)$, for ω=100 (the broader Gaussian line) along with the perturbed state with a perturbation $\beta/M = -30$ meV (+), an anharmonicity of about 30 %. This is an exceptionally large perturbation, chosen to demonstrate that for small perturbations, the neutron Compton profile would certainly be fitted well by a Gaussian. It is fitted with a Gaussian, and the difference is the oscillating line at the bottom. This close approximation to a Gaussian for such a large perturbation is useful since it means that the standard eVS analysis can be used to extract σ, and so $\hbar^2\sigma^2$ can replace $\langle p^2 \rangle$ in equation 94.

Making the replacement $\hbar^2\sigma^2 = \langle p^2 \rangle$ in equation 94, equations 93, 94 and 95 can be combined to obtain an expression linking ω_1 and σ (or kinetic energy) with one variable β.

$$\sigma^2_{H(D)} = \frac{M^{H(D)} f(\gamma)}{\hbar^2} \left(\omega_1^{H(D)} + \frac{2\beta}{M^{H(D)}} \right) \tag{97}$$

With this replacement, equation 94 can be used to show that equation 92 still holds and conclude that $(\sigma_D/\sigma_H)^2 = \sqrt{M_D/M_H}$ is valid for the perturbed system.

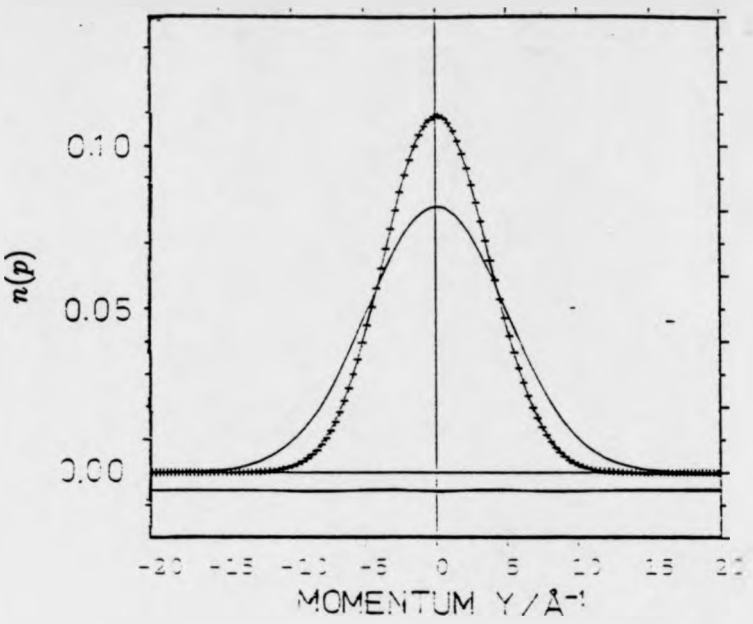

Figure 4.1 The broad Gaussian is the momentum distribution (n(p)) for a harmonic potential with ω=100 meV (the (100) mode in NbD) and mass $M = 2.014$ amu. With a 30 % x^4 perturbation, the perturbed momentum distribution (narrow Gaussian) can be fitted well by a Gaussian (+). The oscillating line at the bottom is the difference between the perturbed n(p) and the fit.

4.1.3 The Zirconium System

At room temperature and pressure, the ZrH_x and ZrD_x systems exists in an ordered phase known as the ϵ-phase for concentrations of $x > 1.70$, the limiting concentration being $x = 2.00$. The H(D) occupy interstitial tetrahedral sites in the fcc zirconium lattice, causing a small tetragonal distortion. The structure is shown in figure 4.2 and was confirmed by Flotow and Osbourne [56], who gives lattice parameters of $a_0 = 4.981 \pm 0.01$ Å and $c_0 = 4.451 \pm 0.01$ Å at 25 ° C. The tetragonal distortion has been found to be temperature dependent and is responsible for the splitting of the optic modes of hydrogen into a doubly-degenerate state and a non-degenerate state at a slightly higher energy. These optic modes have been observed in the Zr-H system by neutron spectroscopy measurements [60, 61, 62] and are also shown in the derived density of states presented in chapter 3.

4.1.4 The numerical calculation of $S(q,\omega)$

It is possible to calculate the neutron Compton profile $J(y)$ from the density of states by performing an exact numerical calculation. The numerical calculation of $S(q,\omega)$ from the density of states has been described in chapter 3, where it was applied to the ZrH_2 vibrational density of states presented in that chapter and compared to a sum of a series of DINS measurements of ZrH_2. Such calculations are compared to one DINS measurement on $ZrH_{1.96}$ and a density of states is derived for the deuteride system by scaling the energy-axis of the density of states data by $\sqrt{2}$. This is valid if the potential in the two systems remains the same, whether or not anharmonicity is present, as shown in section 4.1.2.

4.1.5 The niobium system

The niobium systems are in the β-phase with the H(D) occupying interstitial tetrahedral sites in the bcc niobium lattice. This structure is shown in figure 4.3. The hydride exists in the β-phase at temperatures up to about $420K$, and the deuteride up to $440K$. The tetrahedral point symmetry splits the localised hydrogen vibrations into

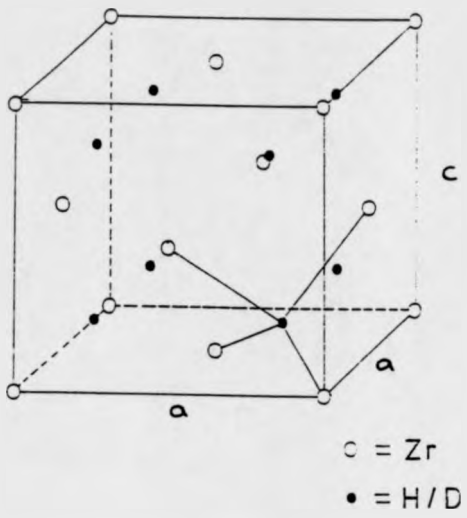

Figure 4.2 The ϵ-phase ZrH_2/ZrD_2 unit cell showing the bonds between one of the interstitial atoms and the nearest neighbour Zr atoms.

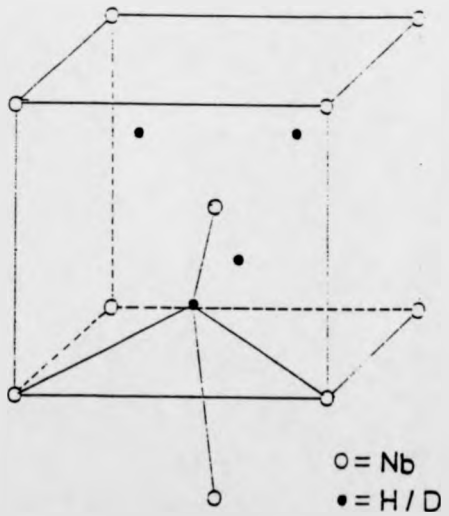

Figure 4.3 The β-phase NbH/NbD unit cell showing the bonds between one of the interstitial atoms and the nearest neighbour Nb atoms.

two levels. According to Richter et al [63], considering coupling to the next nearest four Nb atoms by a longitudinal force constant f, the dynamical matrix ϕ has the form

$$\phi = \frac{4}{5} f \begin{pmatrix} 2 & 0 & 0 \\ 0 & 2 & 0 \\ 0 & 0 & 1 \end{pmatrix} \tag{98}$$

and so the ratio of the upper and lower frequencies , ω_2/ω_1 is given by $\sqrt{2}$. The ω_1 mode is non-degenerate, and the ω_2 mode is doubly-degenerate.

The mean kinetic energies determined with the eVS spectrometer are compared to values determined from directional inelastic neutron spectroscopy measurements. Richter et al [63] and Eckert et al [64] have used incoherent inelastic neutron scattering to observe the optic modes in the Nb-H and Nb-D systems at different temperatures, and have successfully extracted a one-dimensional anharmonicity parameter from the single-crystal measurements on the Nb-D system. They observed the splitting of the three optic modes into two distinct peaks in the Nb-D and NbH systems: the singlet e_{100} and the doublet e_{010} that are expected from the tetrahedral symmetry, and also observed a second harmonic due to the lower D vibration.

Sample	T/K	e_{100}/meV	e_{010}/meV	σ_{Ha}/Å^{-1}	σ_{Anh}/Å^{-1}
$NbH_{0.87}$ †	300	119±1	164±1.5	4.238±0.04	4.238±0.04
$NbH_{0.95}$ †	300	118±1	163±2	4.224±0.05	4.225±0.05
$NbH_{0.85}$ ‡	300	119.0±0.2	166.8±0.5	4.265±0.01	4.265±0.02
$NbD_{0.85}$ ‡	300	87.2±0.2	118.1±0.3	5.096±0.02	5.097±0.02
$NbD_{0.85}$ ‡	300	86.6±0.2	118.1±0.4	5.091±0.02	5.093±0.02

Table 4.1 The experimentally determined first optic mode energies of H/D in Nb-H and Nb-D systems along the crystallographically distinct (100) and (010) directions. Values of σ have been derived from these assuming that the modes are harmonic (σ_{Ha}) and taking the anharmonicity of these systems into account (σ_{Anh}).

For each row in table 4.1, σ_{Ha} is the variance of $J(y)$ calculated from these data assuming the three modes to be harmonic with energies given by e_{100} and e_{010}. σ_{Anh} is that calculated assuming the e_{100} mode possesses an anharmonicity $\beta/M = 3.3$ meV,

and that the e_{010} modes are harmonic, according to the findings of Richter et al. The data are from Richter et al ‡[63] and Eckert et al †[64]. σ_{Anh} is calculated using the equations given in section 4.1.2. In section 4.3, these calculations of σ will be compared to our experimental results.

4.2 EXPERIMENTAL DETAILS

The neutron Compton profiles of the four samples were measured on eVS. The DINS technique and the procedures used to analyse eVS data are presented in chapter 2. Polycrystalline samples were chosen partly because of their easy availability and the fact that the data sets of all relevant detectors can be added together, since $J(y)$ is averaged over all directions and therefore has no directional dependence. This gives better statistical accuracy that a set of directional Compton profiles. The presence of a single phase in the four samples at room temperature makes interpretation of the data simpler.

4.2.1 The manufacturing of the samples

The samples were manufactured at the Department of Physics of the University of Warwick from powdered samples of niobium and zirconium obtained from Goodfellow Metals (Cambridge), and from a zirconium foil supplied by the Compton Scattering Group at Warwick. The grain size and purity of the powdered samples were given as 150 μm and 99.50 % respectively for zirconium and 74 μm and 99.85 % respectively for niobium.

The method used for hydriding the metals allows the monitoring of the amount of hydrogen (deuterium) absorbed by the metal during the process. The procedure is described here in brief and the apparatus is shown in figure 4.4. The sample vessel (Y) and the reaction vessel (X) are made from silica glass that can withstand temperatures in excess of 1500 K. The first procedure is a calibration of certain volumes of the apparatus, which is described below. The sample vessel is first weighed empty, and then weighed with an amount of the metal powder in it. The zirconium foil, which

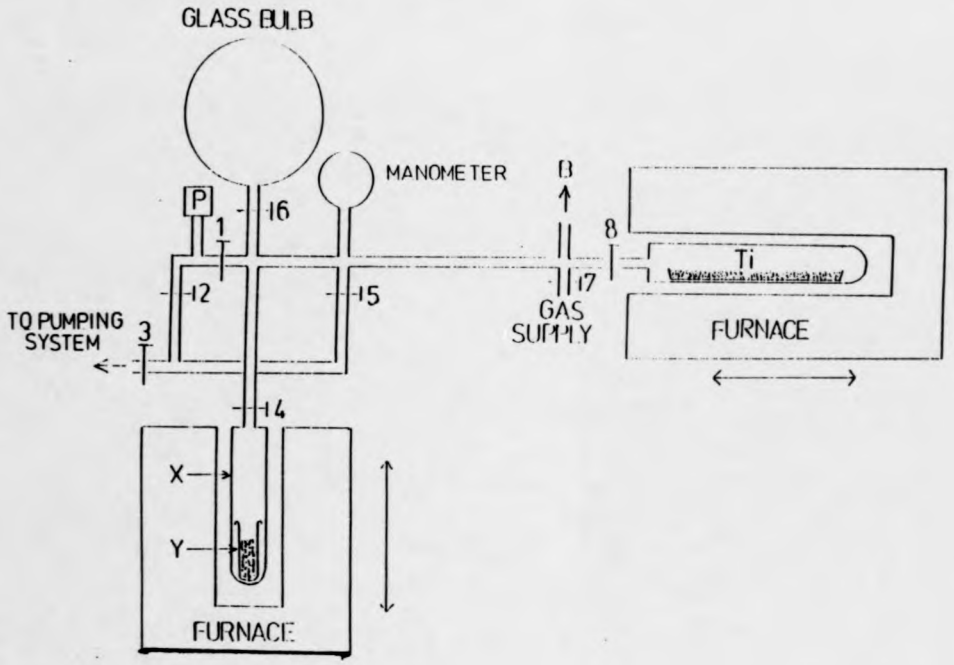

figure 4.4 The apparatus used for preparation of metal hydrides and deuterides.

could not fit inside the reaction vessel, was placed directly into the sample vessel. A titanium 'sponge', consisting of about ten grams of titanium granules in a ceramic boat sits in a silica glass tube, and is used to purify the hydrogen (deuterium) gas, which is absorbed by the 'sponge' before being released again, purified. The very high mobility of hydrogen (deuterium) in titanium causes it to be liberated before heavier impurity atoms, which remain trapped in the 'sponge'. The samples were outgassed at 1200 K for six hours, and then the hydriding process was begun at a temperature determined from the phase diagram of the hydride. The temperature was lowered slowly in each case, and when room temperature was reached, the final pressure reading was made. The sample vessel containing the hydride was weighed to assess the amount of gas absorbed. This provides a check on the pressure measurement. The samples were then transferred to glass containers in an inert dry atmosphere to prevent the absorption of water vapour from the atmosphere during storage. The procedure is described in more detail below.

The volume of the glass bulb is known (2350 cm^3) and is used to calibrate the volume of the tubing enclosed by the valves 2,4,5,6,7 and 8 and the volume of the reaction vessel. This is done by filling the glass bulb with hydrogen at a given pressure, and with the rest of the system evacuated, opening valve 6, thereby allowing it to expand up to the limits defined by the valves 2,4,5,7 and 8. The new volume is determined from the resulting drop in pressure by using the equation of state for an ideal gas, $PV = nRT$. All pressures are measured relative to atmospheric pressure by observing the head of mercury in the manometer. Atmospheric pressure is given by the head of mercury upon fully evacuating the system. Two pumps are used: a mechanical pump is used to reach pressures of a fraction of a mbar, and an oil diffusion pump is used to take the pressure down further to typically 0.01 mbar.

The following procedure describes the outgassing of the titanium sponge. In the case of deuterium, the sponge was replaced with unused titanium. Initially, the reaction vessel X was not attached, valve 4 was closed, and the other valves were open. The system was flushed twice with hydrogen/deuterium and then pumped out to about one mbar using

the rotary pump (taking around 5 minutes) and then the water-cooled diffusion pump was switched on, bringing the pressure down to 0.01 mbar after 2-3 hours. The heater was moved into position around the titanium 'sponge' to clear the titanium from any residual gas, and switched on. The heating liberates trapped hydrogen and deuterium gas, along with some impurities. This procedure was continued until the pressure was stable. The titanium was then isolated by closing valve 8. Hydrogen or deuterium gas was then allowed to enter the system by opening valve 8 and valve 7 at the gas cylinder. The impurities in the hydrogen and deuterium were given by the suppliers as 0.3 %. The titanium was again heated, and valve 8 was opened gradually to allow the gas to enter. Care was taken at this point to prevent the exothermic reaction of the gas being absorbed creating too much heat that might cause the vessel to crack, and it was found that a point was reached when the heater needed to be removed, and the reaction was self-sustaining. When sufficient hydrogen (deuterium) had been absorbed, valve 8 was closed and the remaining gas in the system was pumped out. The whole system was pumped out to 0.01 bar and atmospheric pressure noted by measuring the head of mercury in the barometer.

The following procedure describes the hydriding process. The reaction vessel was weighed, filled with an amount of the sample and re-weighed. It was placed in the sample vessel and this was attached at valve 4, which was opened gradually to evacuate the air. The sample was outgassed at a temperature of 1500K for several hours whilst pumping on the system with valves 7 and 8 closed.

The titanium was re-heated to liberate the hydrogen (deuterium), with valves 2, 4, 5 and 7 closed. The molar volume of gas admitted was in excess of that required to hydride the metal sample to the required concentration. Valve 6 was closed, thus isolating the glass bulb (of volume 2350 cm^3), and the remaining gas pumped out of the system. This volume of gas was allowed to expand up to the limits set by the closed valves 2, 4, 5, 7 and 8 by opening valve 6. The purified gas was allowed to expand into the reaction vessel by opening valve 4 . The reaction was started at a temperature determined from the phase diagram showing the phases as a function of

P, V and T. This was 1100 K for zirconium and 1400 K for niobium. The temperature was lowered by typically several degrees/minute, by turning off the furnace, and the amount of hydrogen (deuterium) absorbed by the sample monitored by observing the pressure drop.

The hydrides were manufactured first, and then the titanium sponge was replaced with fresh titanium to ensure that the deuterides would not be contaminated with hydrogen. The DINS measurements are most sensitive to the latter, due to the small incoherent scattering cross-section of D compared to H, so it is important to minimise contamination from hydrogen in the deuterides.

The samples were weighed after hydriding, and the concentration of absorbed gas in the metal calculated. The concentrations obtained were compared to the concentrations calculated from the pressure drop measurement. The results are compared in table 4.2.

Sample	weight measurement	pressure measurement
Nb-H	$NbH_{1.00}$	$NbH_{0.95}$
Nb-D	—	$NbD_{0.98}$
Zr-H	$ZrH_{1.89}$	$ZrH_{1.96}$
Zr-D	$ZrD_{1.85}$	$ZrD_{2.00}$

Table 4.2 The H/D concentrations of the four hydride / deuteride samples manufactured at the University of Warwick determined by weight and pressure measurements (see text).

A weight measurement of the concentration of Nb-D was not possible because the reaction vessel broke during the hydriding process. The error in the weight measurement is estimated at ± 0.03 atoms H per metal atom, due to an error in the weighing of the samples of ± 0.001 grams, however a systematic error seems to be introduced due to loss of material occurring during the hydriding process, explaining the usually smaller value of the weight measurement. In the case of the powdered samples, metal powder was often deposited on the inside of the sample vessel upon pumping out, when trapped air in the powdered metal would suddenly escape. In the case of the zirconium foil, this became very brittle and small pieces of it may have been lost quite easily.

The pressure measurements are believed to be more accurate. The errors are estimated from the error from the manometer reading, at approximately 1 %. With the reading of the pressure measurements, the meniscus at the mercury/atmosphere interface bulged significantly when the head of mercury was large, and so care was taken not to overestimate the pressure of the gas by reading from the top of the meniscus by reading the value at the centre-point.

4.2.2 The DINS measurements

The detector arrangement on eVS at the time of these measurements is shown in figure 2.10 and consisted of forty detectors at forward scattering angles, and ten detectors at backward scattering. For neutron scattering from hydrogen, scattering is only observed at angles less than 90 ° and so this experimental set-up was ideal for studying hydrogeneous and low-mass systems. The measurements were performed for approximately 24 hours in each case. The experimental procedure is described below.

The samples were removed from their airtight containers. No release of absorbed gas was evident over the period of two weeks between the manufacture of the samples and the experiments. This would have been noticed as a release of pressure on opening the containers. The samples were ground to a fine powder in a clean pestle and mortar, which was cleaned thoroughly with ethanol to avoid contamination of the samples.

The powdered samples were placed in aluminium sample-holders. These were of a standard design and consisted of two 89.5 mm square aluminium plates with a 68 mm square thinned aluminium window for the beam. The neutron beam is circular, with a 30 mm diameter umbra and a penumbra extending out to 50 mm in diameter. The samples were evenly distributed over an area to cover the umbra in the centre of the sample-holder. The samples were placed on the end of a centre-stick, centrally in the eVS sample tank, with the plane of the sample perpendicular to the beam. The sample tank and beam-line was evacuated using the rotary pump which is connected to the eVS experiment.

Gold analyser foils were used in all measurements. The resonance energy used is at 4922 meV. A value of 140 meV is used for the HWHM of the Lorentzian contribution to the resolution function. For scattering from hydrogen and deuterium, this choice of analyser foil offers a good compromise between resolution and counting rate. The experiments proceeded in the manner described in chapter 2.

4.3 ANALYSIS AND RESULTS

4.3.1 The neutron Compton profiles

The experimental results presented here are the neutron Compton profiles of H (D) in the completely ordered polycrystalline metal hydrides (deuterides) $ZrH_{1.96}$, $ZrD_{2.00}$, $NbH_{0.95}$ and $NbD_{0.98}$ measured at 290K. For each sample, the presence of a single phase was confirmed by interpreting the diffraction data gathered in the time-of-flight region 1000 to 15000 μs by the detector at the largest scattering angle at forward scattering (77 °).

The data analysis procedure is described in chapter 2. The sum of three Voigt functions were fitted in time-of-flight: for the metal (Zr/Nb), for the interstitials (H/D) and for aluminium, which was present in the sample holders in each case. The spectra were fitted typically with χ^2 of between 0.9 and 1.1.

Figures 4.5 to 4.8 and 4.9 to 4.12 show $J_m(y)$ for $ZrH_{1.96}$ and $ZrD_{2.00}$ over four ranges of momentum transfer (circles) corresponding to detectors between the angles 36.0 to 43.7 °, 45.8 to 53.7 °, 57.5 to 66.0 ° and 68.4 to 76.9 ° (see figure 2.1). Each 'bank' contains ten detectors and the $J_m(y)$ shown for each momentum transfer range is the sum of these ten detectors. In each case, the line is the exact calculation (see 4.1.4), including resolution broadening, of $J_m(y)$. For scattering from hydrogen, the corresponding momentum transfer ranges are 35.38 to 46.53 $Å^{-1}$, 50.20 to 66.40 $Å^{-1}$, 76.58 to 109.87 $Å^{-1}$, and 123.56 to 211.70 $Å^{-1}$ and for scattering from deuterium, they are 31.99 to 39.65 $Å^{-1}$, 41.90 to 50.36 $Å^{-1}$, 54.65 to 64.84 $Å^{-1}$ and 67.82 to 78.95 $Å^{-1}$.

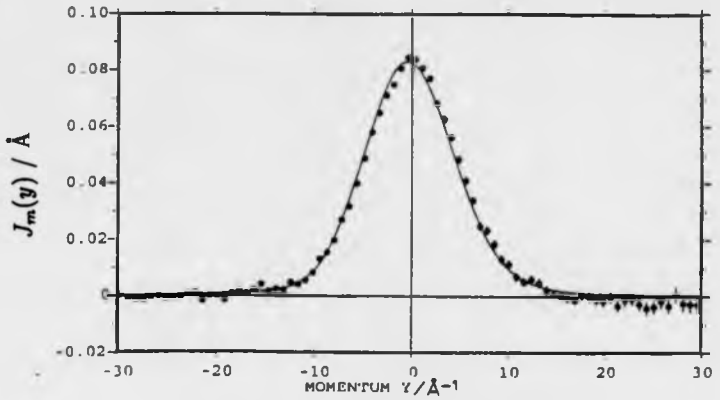

Figure 4.5 The measured NCP (circles) and the numerical calculation of the measured NCP (solid line) for ϵ-phase $ZrH_{1.96}$ for the momentum transfer range 35.4 - 46.5 Å^{-1}.

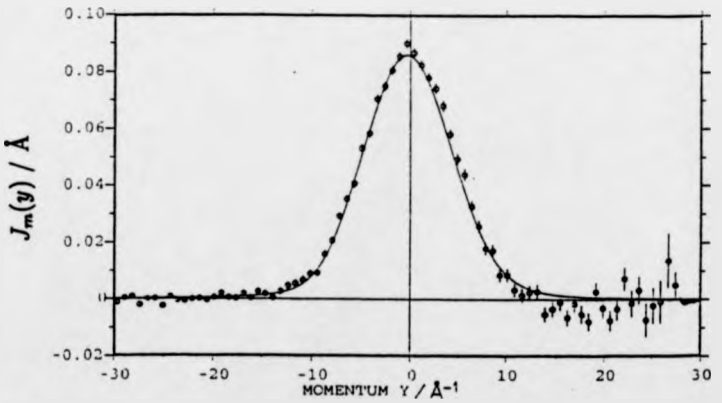

Figure 4.6 The measured NCP (circles) and the numerical calculation of the measured NCP (solid line) for ϵ-phase $ZrH_{1.96}$ for the momentum transfer range 50.2 - 66.4 Å^{-1}.

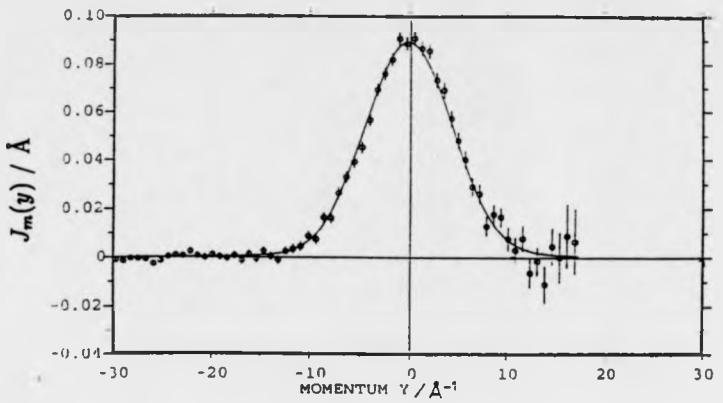

Figure 4.7 The measured NCP (circles) and the numerical calculation of the measured NCP (solid line) for ϵ-phase $ZrH_{1.96}$ for the momentum transfer range 76.6 - 109.9 Å^{-1}.

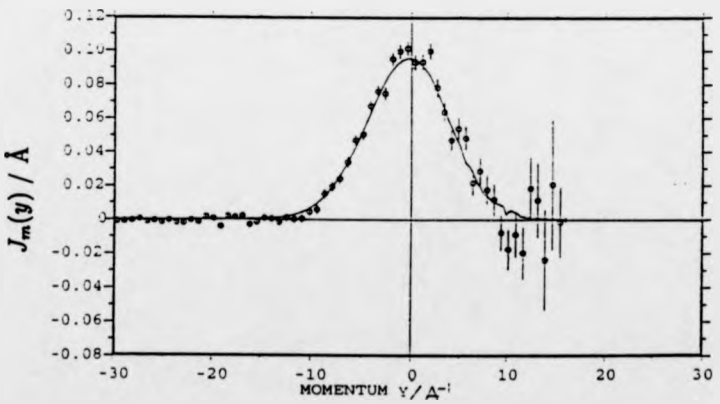

Figure 4.8 The measured NCP (circles) and the numerical calculation of the measured NCP (solid line) for ϵ-phase $ZrH_{1.96}$ for the momentum transfer range 123.6 - 211.7 Å^{-1}.

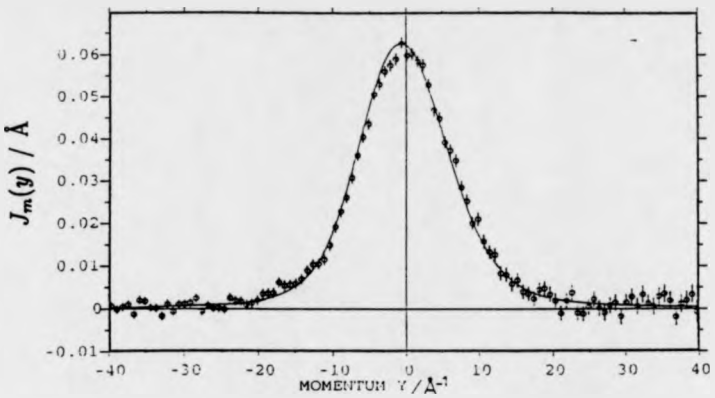

Figure 4.9 The measured NCP (circles) and the numerical calculation of the measured NCP (solid line) for ϵ-phase $ZrD_{2.00}$ for the momentum transfer range 32.0 - 39.7 Å^{-1}.

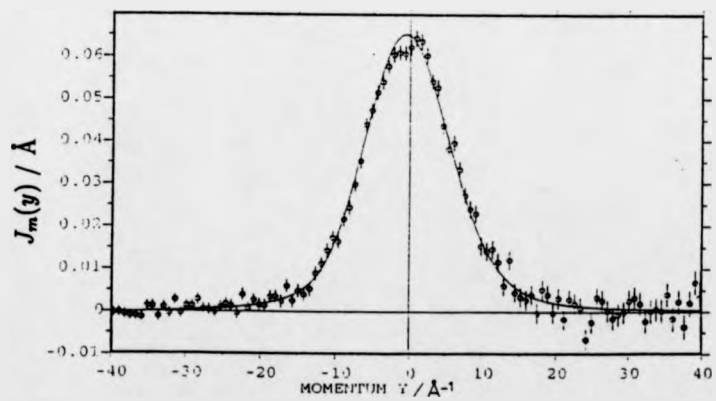

Figure 4.10 The measured NCP (circles) and the numerical calculation of the measured NCP (solid line) for ϵ-phase $ZrD_{2.00}$ for the momentum transfer range 41.9 - 50.4 Å^{-1}.

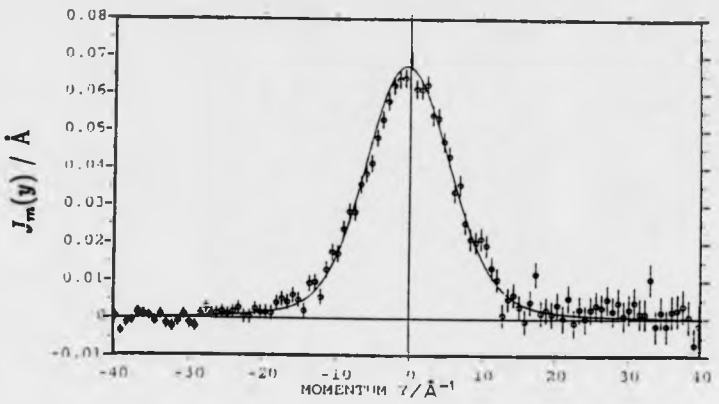

Figure 4.11 The measured NCP (circles) and the numerical calculation of the measured NCP (solid line) for ϵ-phase $ZrD_{2.00}$ for the momentum transfer range 54.7 - 64.8 Å^{-1}.

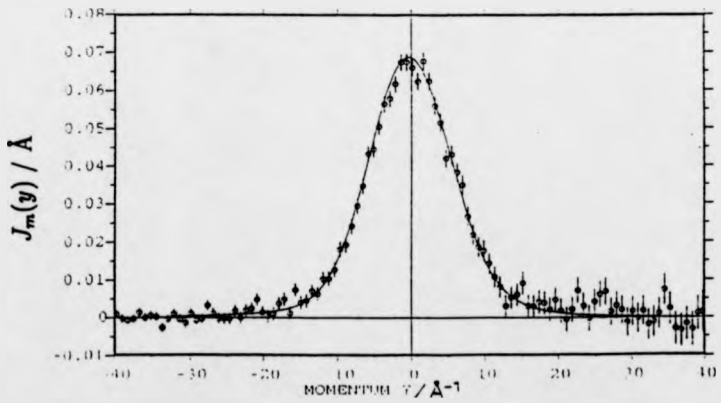

Figure 4.12 The measured NCP (circles) and the numerical calculation of the measured NCP (solid line) for ϵ-phase $ZrD_{2.00}$ for the momentum transfer range 67.8 - 79.0 Å^{-1}.

Figure 4.13 shows the fitted peak position of $J_m(y)$ for $ZrH_{1.96}$ (circles) with the dashed line showing the fitted peak position from the simulation from the density of states. Compared to figure 3.17, the eVS data points have a greater spread, attributable to the poorer counting statistics of this single run. Figure 4.14 shows σ as a function of momentum transfer for $ZrH_{1.96}$. The dashed line shows the values of σ determined by the simulation from the density of states. Figures 4.15 and 4.16 show the data corresponding to figures 4.13 and 4.14 respectively, except for $ZrD_{2.00}$.

The measured neutron Compton profiles for $NbH_{0.95}$ and $NbD_{0.98}$ are shown in figures 4.17 to 4.20. For these data, since no vibrational density of states was available, inelastic neutron spectroscopy data were used to compare to the values of σ determined. Figures 4.21 and 4.22 (circles) show σ as a function of momentum transfer for $NbH_{0.95}$ and $NbD_{0.98}$ respectively. The horizontal line is $x = 4.225$ for the hydride and $x = 5.094$ for the deuteride and marks the value of σ_{Anh} given in table 4.1. The crosses show the corresponding symmetrised data.

Table 4.3 shows weighted average values of σ for each sample for the high and low angle banks at forward scattering angles. In the impulse approximation, $\omega = q^2/(2M)$ at $y = 0$, about which the recoil peak is centred. By fitting a straight line to a plot of q_r^2 verses ω_r (where q_r and ω_r are measurements of q and ω at the recoil peak position) using $\omega_r = q_r^2/(2M) + C$ an effective mass M is obtained and an intercept C, which is a broad measure of how valid the impulse approximation is. The subscripts l and h refer to the low (36 - 66.4 °) and high (58 - 77 °) angle banks respectively.

Sample	σ_lÅ^{-1}	M_l/amu	C_l/meV	σ_h/Å^{-1}	M_h/amu	C_h/meV
$NbH_{0.95}$	4.29±0.04	1.015±0.007	-4±34	4.14±0.08	1.015±0.002	82±85
$NbD_{0.98}$	5.27±0.07	2.03±0.03	-12±24	5.11±0.08	1.98±0.02	-110±44
$ZrH_{1.96}$	4.18±0.03	1.013±0.005	-5±28	3.97±0.06	1.014±0.002	85±62
$ZrD_{2.00}$	5.05±0.05	2.02±0.02	-26±20	5.04±0.07	2.04±0.02	34±43

Table 4.3 The results of the analysis of the eVS measurements. The data were y-transformed and the measured neutron Compton profiles were not symmetrised.

Figures 4.23 and 4.24 show plots of q^2 verses ω at the recoil peak position for the ZrH_2

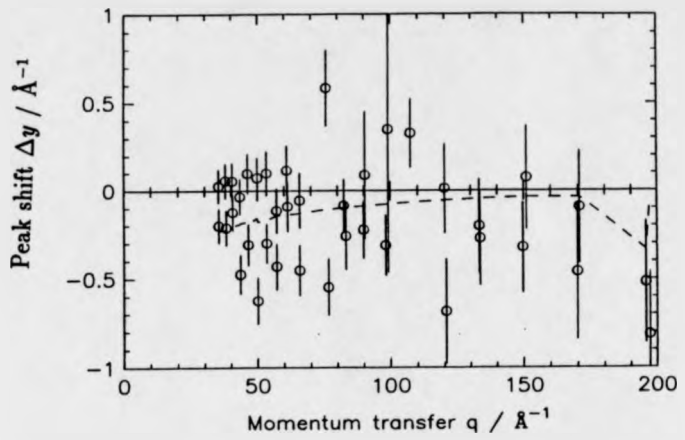

Figure 4.13 The fitted peak position (circles) of the measured NCP, as a function of momentum transfer q in ϵ-phase $ZrH_{1.96}$ at 290 K. The horizontal line at $\sigma = 4.18$ is the result obtained from the numerical simulation.

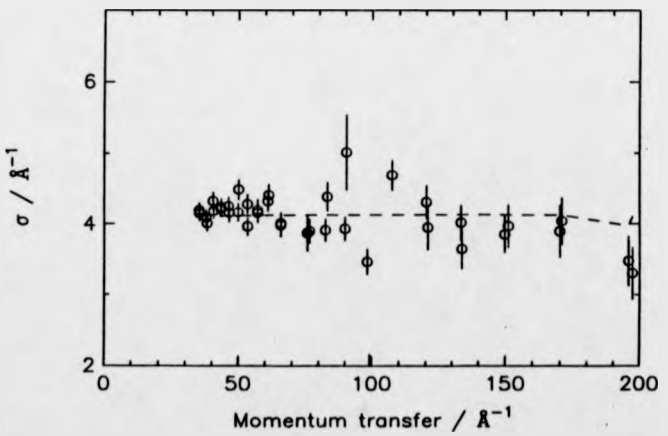

Figure 4.14 σ (circles) as a function of momentum transfer q in ϵ-phase $ZrD_{2.00}$ at 290 K. The horizontal line at $\sigma = 4.96$ is the result obtained from the density of states.

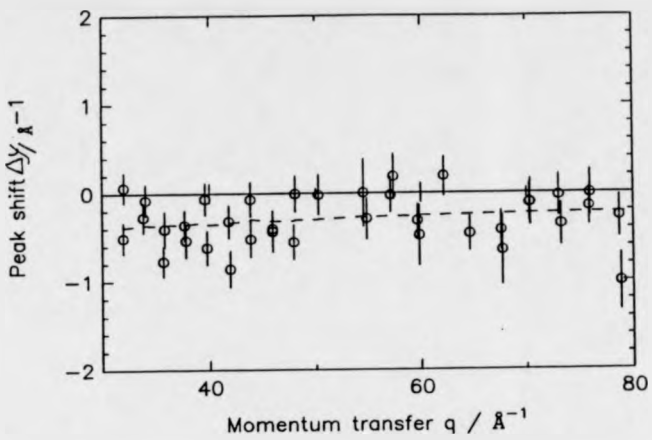

Figure 4.15 The fitted peak position (circles) of the measured NCP, as a function of momentum transfer q in ϵ-phase $ZrD_{2.00}$ at 290 K.

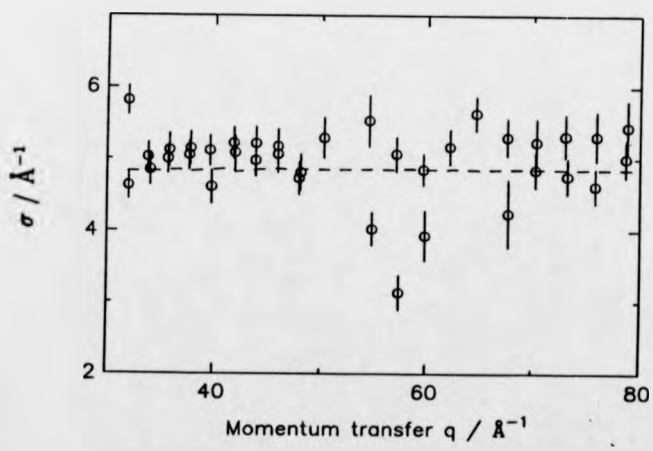

Figure 4.16 σ (circles) as a function of momentum transfer q in ϵ-phase $ZrD_{2.00}$ at 290 K. The horizontal line at $\sigma = 4.96$ is the result obtained from the numerical simulation.

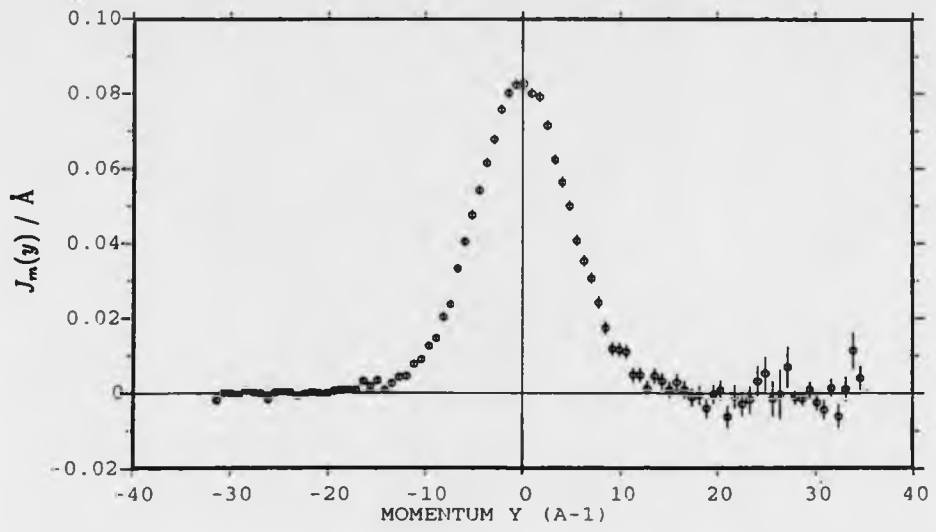

Figure 4.17 The measured NCP for $NbH_{0.95}$ in the momentum transfer range 35.4 - 66.4 $Å^{-1}$.

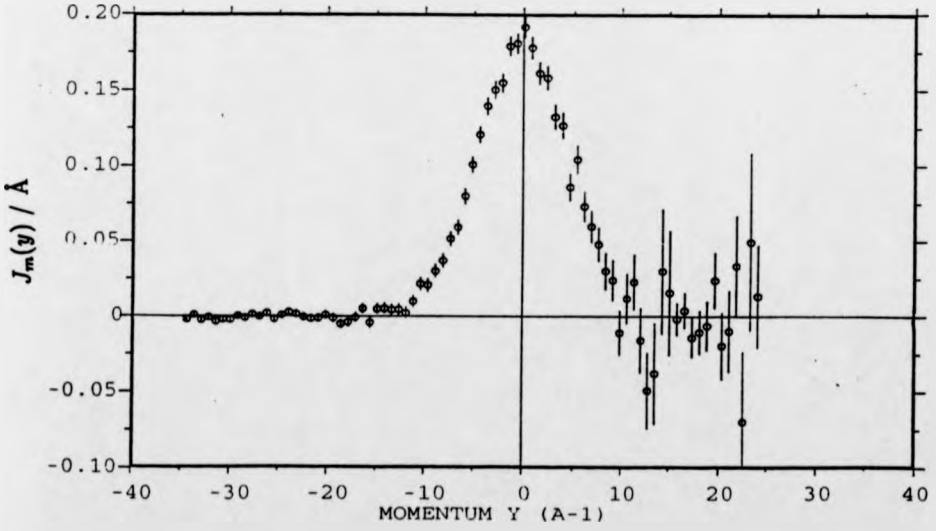

Figure 4.18 The measured NCP for $NbH_{0.95}$ in the momentum transfer range 76.6 - 109.9 $Å^{-1}$.

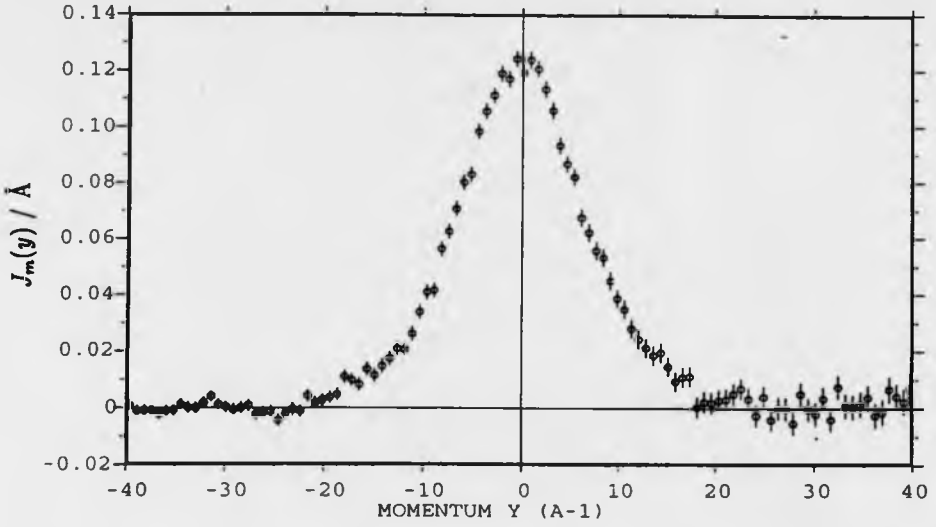

Figure 4.19 The measured NCP for $NbD_{0.98}$ in the momentum transfer range 32.0 - 50.4 $Å^{-1}$.

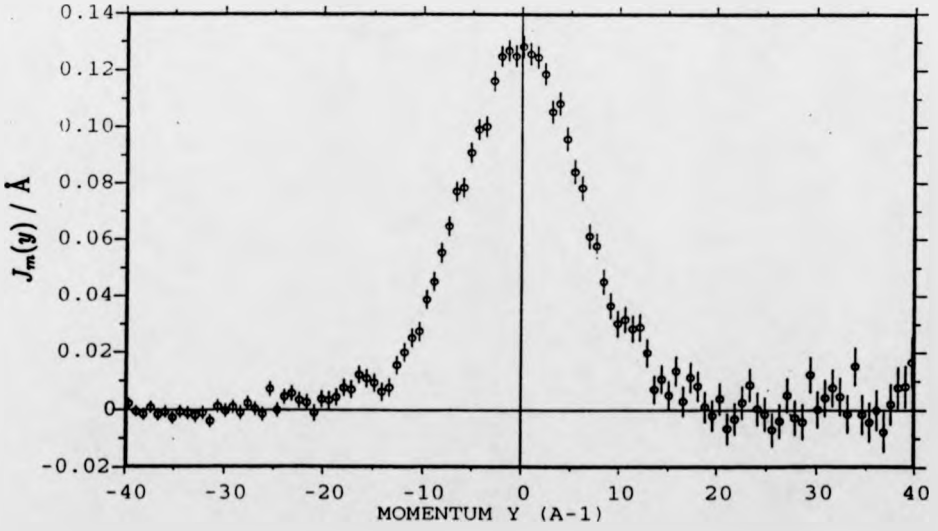

Figure 4.20 The measured NCP for $NbD_{0.98}$ in the momentum transfer range 54.7 - 79.0 $Å^{-1}$.

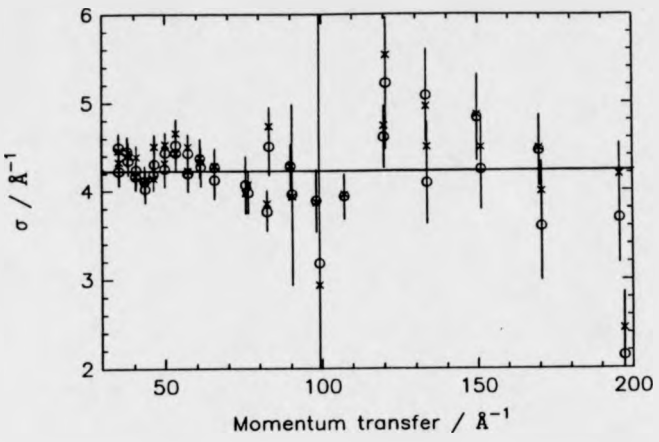

Figure 4.21 σ (circles) as a function of momentum transfer q in β-phase $NbH_{0.95}$ at 290 K. The horizontal line at $\sigma = 4.25$ is the result obtained from inelastic neutron spectroscopy data and the crosses are the σ values determined from the symmetrised data.

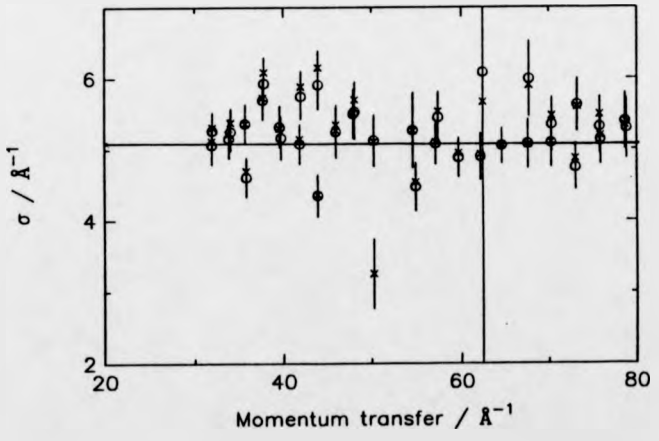

Figure 4.22 σ (circles) as a function of momentum transfer q in β-phase $NbD_{0.98}$ at 290 K. The horizontal line at $\sigma = 5.10$ is the result obtained from inelastic neutron spectroscopy data and the crosses are the σ values determined from the symmetrised data.

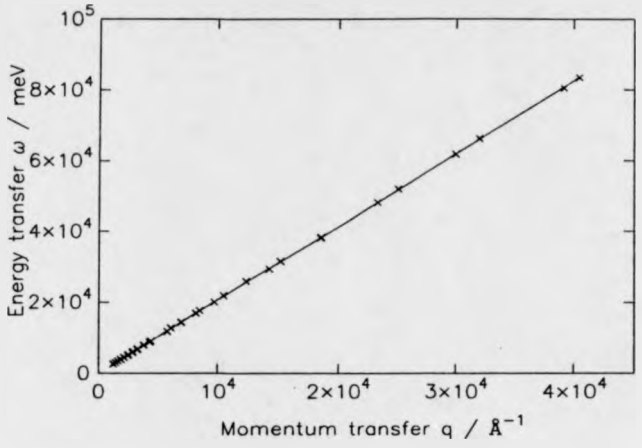

Figure 4.23 ω verses q^2 at the recoil peak position for $ZrH_{1.96}$. The straight line is a least-squares fit to $\omega = q^2/2M + C$.

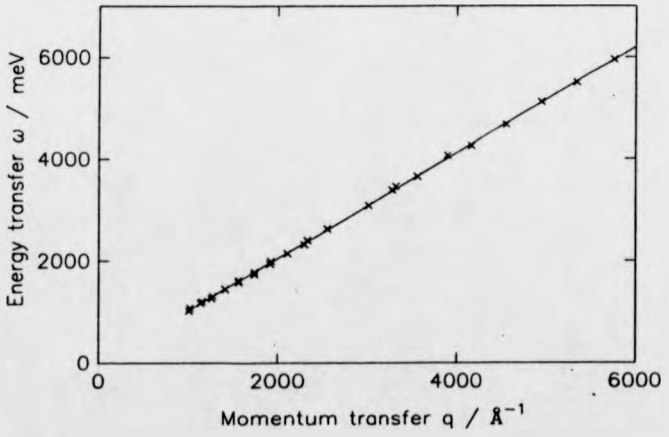

Figure 4.24 ω verses q^2 at the recoil peak position for $ZrD_{2.00}$. The straight line is a least-squares fit to $\omega = q^2/2M + C$.

and ZrD_2 systems respectively. Figures 4.25 and 4.26 show plots of q^2 verses ω at the recoil peak position for the NbH and NbD systems respectively.

Sample	σ_l/Å^{-1}	M_l/amu	C_l/meV	σ_h/Å^{-1}	M_h/amu	C_h/meV
$NbH_{0.95}$	4.34±0.03	1.0078±0.0007	-0.33±0.36	4.24±0.05	1.0078±0.0001	-4.3±4.9
$NbD_{0.98}$	5.32±0.05	2.014±0.005	0.1±0.5	5.16±0.06	2.013±0.002	-3.1±3.9
$ZrH_{1.96}$	4.22±0.02	1.0079±0.0003	-3.8±0.2	4.05±0.04	1.0079±0.0007	1.8±2.9
$ZrD_{2.00}$	5.11±0.04	2.014±0.006	-4.4±0.6	5.09±0.05	2.0136±0.0009	-0.2±21

Table 4.4 The results of the analysis of the eVS data. The data were y-transformed and the measured neutron Compton profiles were symmetrised to remove final-state effects of order q^{-1}.

Table 4.5 shows values for σ, M and C for the $ZrH_{1.96}$ and $ZrD_{2.00}$ numerical calculations.

Table 4.6 shows values for σ, M and C for the $ZrH_{1.96}$ and $ZrD_{1.96}$ numerical calculations (symmetrised data).

The simulations of back-scattering data for the Zr-D system gave values of σ =4.8270±0.0010 M =2.0189±0.0001 amu and $C = -11.2 \pm 9.7$ meV.

The ratio σ_D^2/σ_H^2 was determined for each system, and the results were close to the expected value of $\sqrt{2}$. For the niobium systems, $\sigma_D^2/\sigma_H^2 = 1.503 \pm 0.03$. The zirconium systems yield a value of 1.466 ± 0.03.

4.4 DISCUSSION

The presence of ϵ-phase ZrH_2 and ZrD_2 is confirmed from the presence of the (002) and (202) peaks which are only present in the ϵ-phase and have d-spacings of 2.209 Å and 1.650 Å in ZrH_2 respectively [66]. The powder diffraction pattern determined from the high angle eVS detectors is shown in figure 4.27. The (002) peak is observed in the $ZrH_{1.96}$ sample with d-spacings of 2.22±0.01 Å. The (202) peak was not observed in the hydride, but both peaks were observed in the deuteride with positions of 2.22±0.01Å

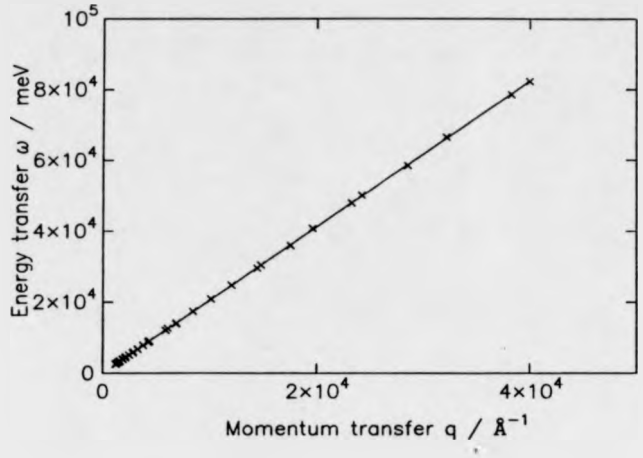

Figure 4.25 ω verses q^2 at the recoil peak position for $NbH_{0.95}$. The straight line is a least-squares fit to $\omega = q^2/2M + C$.

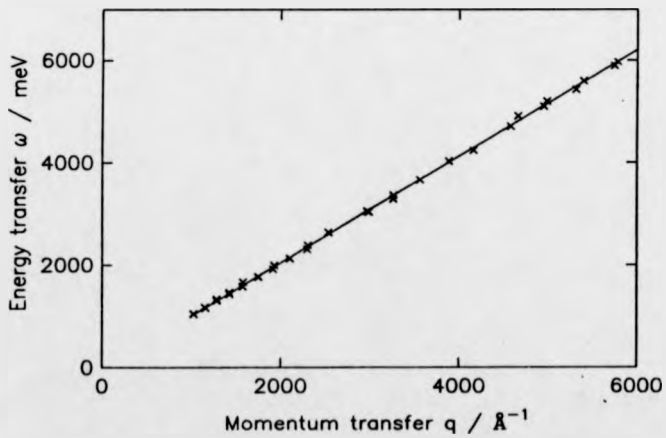

Figure 4.26 ω verses q^2 at the recoil peak position for $NbD_{0.98}$. The straight line is a least-squares fit to $\omega = q^2/2M + C$.

Sample	σ_l/Å^{-1}	M_l/amu	C_l/meV	σ_h / Å^{-1}	M_h/amu	C_h/meV
$ZrH_{1.96}$	4.119±0.003	1.0080±0.0002	-35±1	4.126±0.002	1.0090±0.0005	-2±17
$ZrD_{2.00}$	4.957±0.007	2.0226±0.0009	-38±1	4.969±0.004	2.0193±0.0002	-41±1

Table 4.5 The results of the analysis of the numerical simulations of the Zr-H and Zr-D systems over the low and high angle banks.

Sample	σ_l / Å^{-1}	M_l / amu	C_l / meV	σ_h / Å^{-1}	M_h / amu	C_h / meV
$ZrH_{1.96}$	4.157±0.002	1.007900±1.8×10^{-7}	0.0015±0.0009	4.151±0.002	1.0078±0.0000	-1.6±0.3
$ZrD_{2.00}$	4.847±0.008	2.0217±0.0008	-21.8±0.7	4.853±0.005	2.0170±0.0001	-27±0.3

Table 4.6 The results of the analysis of the numerical simulations of the Zr-H and Zr-D systems over the low and high angle banks (symmetrised data).

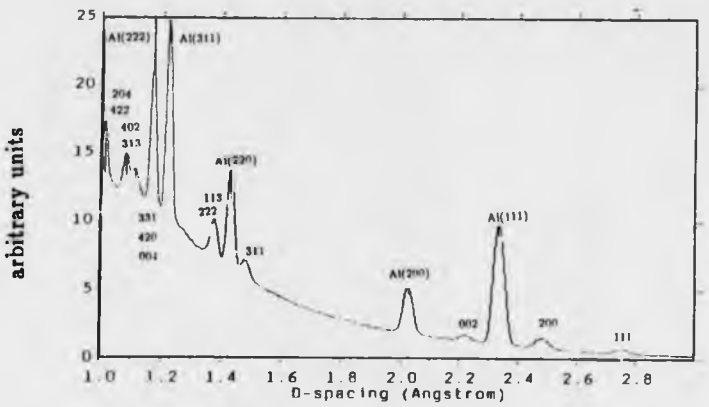

Figure 4.27 Diffraction pattern of $ZrH_{1.96}$ in an aluminium holder. The peaks marked Al are aluminium Bragg reflections. The other reflections are due to the metal hydride. The presence of the (002) peak confirms that ϵ-phase Zr-H is present. All peaks are identified as belonging either to aluminium or the metal hydride.

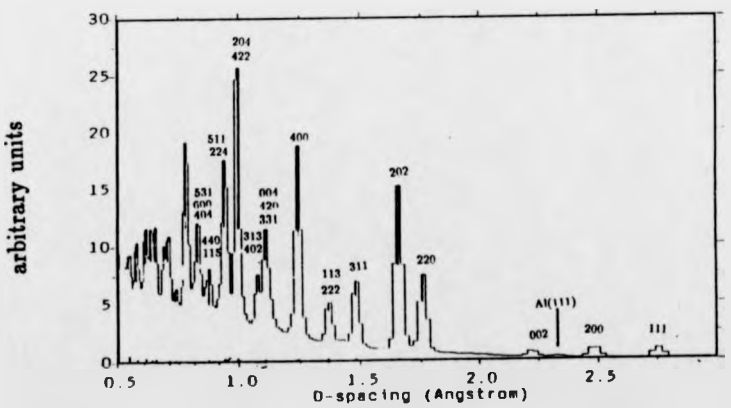

Figure 4.28 Diffraction pattern of $ZrD_{2.00}$ in an aluminium holder. The peaks marked Al are aluminium Bragg reflections. The other reflections are due to the metal deuteride. The presence of the (002) peak confirms that ϵ-phase Zr-H is present. All peaks are identified as belonging either to aluminium or the metal deuteride.

and 1.66±0.01Å respectively. Figure 4.28 shows the diffraction pattern for the $ZrD_{2.00}$. The aluminium scattering here is much weaker because the deuteride experiment was performed in an open holder. Many other peaks were indexed, which are common to both the ϵ and the neighbouring δ-phase, but the difference in the d-spacing for these reflections common to both structures is between 0 and 2 %, and could not be resolved. At room temperature, and between concentrations of 1.70 and 2.00 atoms of H per Zr, ZrH_x exists only in the ϵ-phase, so having confirmed the presence of the ϵ-phase in our sample, the presence of any other is ruled out.

The high temperature (say above 250 K) region of the phase diagrams of the Nb-H and Nb-D systems have been thoroughly investigated [67, 68]. These sources state that NbH_x exists in a single β-phase for $0.72 < x < 1.05$ and that NbD_x exists in a single β-phase for $0.70 < x$. The diffraction data were indexed for the Nb-H and Nb-D samples using neutron diffraction data by Somenkov [59]. These are shown in figures 4.29 and 4.30 for the hydride and deuteride respectively.

It is worth noting that the measurements of σ made between 69 and 77 ° in the hydride systems (at the largest scattering angles) are not very reliable, since at very short times of flight, the data become very noisy. This seems to be a limitation associated with the electronics in the time-of-flight range below 50 μs and only affects the hydride measurements for this bank because the recoil peak occurs in this region. This explains why the results for σ from the high and low angle banks are within error for the deuteride measurements, but there is a significant difference (2.5 - 5 standard deviations) in the case of the hydride measurements. For the hydride measurements, the low angle bank is the more reliable, despite being over a lower momentum-transfer range.

It can be seen that in figures 4.5 to 4.12 the $ZrH_{1.96}$ and $ZrD_{2.00}$ measured neutron Compton profiles compare closely to $J_m(y)$ over all the ranges of momentum transfer. This is expected, since the impulse approximation is not implicit in these calculations. The asymmetry of $J_m(y)$ and $J_m(y)$ indicates the presence of final-state effects. In the impulse approximation, the recoil peak is centred about $y = 0$. This is asymptotically

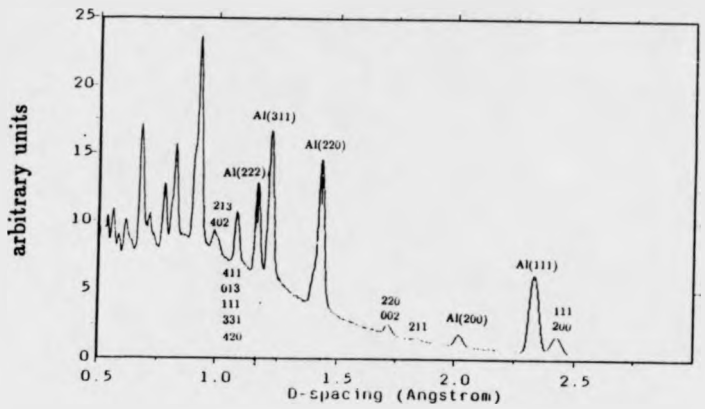

Figure 4.29 Diffraction pattern of $NbH_{0.95}$ in an aluminium holder. The peaks marked Al are aluminium Bragg reflections. The other reflections are due to the metal hydride. All peaks are identified as belonging either to aluminium or the metal hydride.

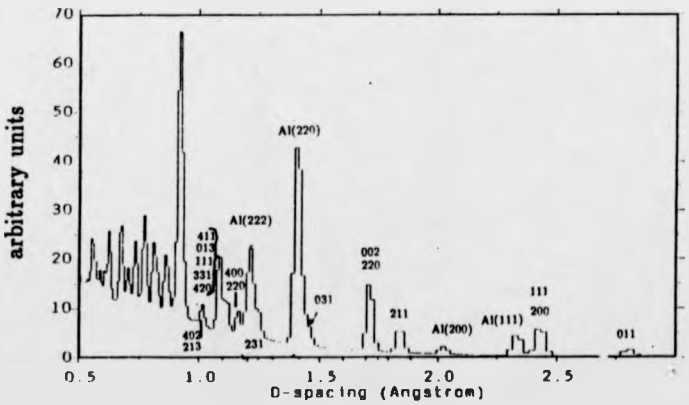

Figure 4.30 Diffraction pattern of $NbD_{0.98}$ in an aluminium holder. The peaks marked Al are aluminium Bragg reflections. The other reflections are due to the metal deuteride. The presence of the (002) peak confirms that ϵ-phase Zr-H is present. All peaks are identified as belonging either to aluminium or the metal deuteride.

reached as $q \rightarrow \infty$. At finite q the recoil peak is shifted to negative y, and this shift becomes more negative as q becomes smaller. This is shown in figures 4.13 and 4.15 where the fitted recoil-peak position is plotted as a function of q for both the experimental (+) and simulated (triangles) measured neutron Compton profiles. Though the error on the peak positions of $J_m(y)$ is relatively large, it can be seen that in general, the recoil peak position of $J_m(y)$ overestimates the recoil peak position of $J_m(y)$ by a factor of about 2 over the whole momentum-transfer range.

Expressing $S(q,\omega)$ at finite q by the additive approach of Sears (section 1.27) gives equations 43 and 44. Since $J(y)$ is symmetric, the terms of order q^{-1} are symmetric and those of order q^{-2} are asymmetric. Therefore, symmetrising $J(y)$ obtained from transforming $S(q,\omega)$ to y-space about $y = 0$ cancels out all terms of order q^{-1} [69] $J_{msym}(y)$ is obtained, which contains residual final-state effects of order q^{-2}. A self-consistent correction procedure for these effects, introduced in Sears' paper can then be used to correct these. Alternatively, if it can be shown that these corrections can be neglected, then values for σ obtained from $J_{msym}(y)$ should be free of final-state effects. Taking just the first three terms in the expansion of $J(y)$ (equation 47) and symmetrising gives [4]

$$S_S(q,\omega) = \frac{m}{\hbar q}\left[1 + A_4(q)\frac{d^4}{dy^4}\right] J(y). \tag{99}$$

A quantitative measure of the relative magnitude of the correction term (the second term in the brackets in equation 99 is obtained from the expression $\eta_s = (q_s/q)^2$ where $q_s = \langle \mathbf{F}^2 \rangle/(4\sqrt{2}K_0)$, $\mathbf{F}$ is the force on the scattering atom and $\eta_s = A_4/y_0^4$ with $y_0 = \int_{-\infty}^{\infty} y^2 J(y)dy$. For a harmonic oscillator,

$$\eta_s = \frac{m\omega}{4\hbar^2 q^2}. \tag{100}$$

Values are obtained of between 0.0075 and 0.0020 for the low-angle bank of detectors and scattering from hydrogen. For scattering from deuterium, values of between 0.013 and 0.0053 are obtained for this bank. For the high-angle bank, values of between 0.0015 and 0.0002 are obtained for scattering from hydrogen, but at these angles, hydrogen data are unreliable. For deuterium on this bank, we obtain between 0.0041

and 0.0019. The peak shift calculated is larger for scattering from deuterium than from hydrogen. This is confirmed by the peak shifts observed in figures 4.13 and 4.15. The statistical uncertainty in σ is typically 1 % and so at this level it is not worth correcting the data for final state effects beyond symmetrising the data.

The effect of symmetrising $J(y)$ is to increase σ by about 1 %, as can be see by comparing σ in tables 4.4 and 4.3. As expected, the values for C given in table 4.4 are close to zero, since the effect of symmetrising is to centre $J_S(y)$ about $y = 0$.

There is a predicted effect on the measured neutron Compton profile due to interatomic interference [70] (i.e. the invalidity of the incoherent approximation). This can be removed by averaging over a range of q. The values of σ presented in tables 4.3 and 4.4 are obtained by a weighted average over the detector bank concerned, and so this correction is performed. In the $NbH_{0.95}$ system, an oscillatory variation is found in σ in the q range 20 – 200 $Å^{-1}$ but it is not clear what causes this. Figures 4.14 and 4.16 and 4.22 show no significant q-dependence for the measurements of σ in $ZrH_{1.96}$, $ZrD_{2.00}$ and $NbD_{0.98}$.

Finding that the momentum distribution of an anharmonic mode may be satisfactorily represented by a Gaussian function is important, since the eVS analysis relies on this assumption. There are expected to be an increase in the number of single-crystal studies on eVS with the introduction of scintillation detectors, and the consequential increase of counting rate by a factor of 10 to 50. It is therefore important to ensure that the fitting of a Voigt function to the measured neutron Compton profile is valid. This has been achieved. It is anticipated, however, that with the increase of counting rate more sophisticated data analysis will need to be introduced in order to correct for final-state effect, as the effects of $\mathcal{O}(q^{-2})$ final-state effects become significant.

4.5 SUMMARY

For anharmonic systems, the assumption that the momentum distribution is a Gaussian (used in the eVS analysis) is valid and that for the statistical accuracy of the

data presented here, final-state effect corrections beyond symmetrising the measured neutron Compton profile are unnecessary. Measurements of the mean kinetic energies in polycrystalline metal hydride/deuteride samples agree with results obtained from two different methods. In the first, mean kinetic energies were derived from inelastic neutron spectroscopy data for the Nb-H/D systems, and in the second, mean kinetic energies were determined from exact numerical calculations of the eVS data based on a measurement of the ZrH_2 vibrational density of states. Consequently, it is shown that despite deviations from the impulse approximations for the momentum transfer ranges in question, the eVS spectrometer measures mean kinetic energies to better than 1 % in these measurements.

CHAPTER 5

The momentum distribution of polycrystalline lithium above and below the martensitic phase transition

5.1 INTRODUCTION

Lithium is bcc at room temperature, but undergoes a martensitic structural phase transition upon cooling below about 78 K [71]. It transforms to a combination of the 9R-related (Sm-type) structure and the bcc structure, both coexisting uniformly throughout the lattice, as confirmed by neutron diffraction studies from polycrystalline lithium [72, 78, 73, 74, 77, 76] and single crystal studies [79, 85, 86, 88] above and below the martensitic phase transition. A partial transition from the 9R structure to an fcc structure under conditions of increased pressure has been observed in high resolution neutron diffraction experiments [74]. The fcc structure can also be obtained by cold working at low temperatures [80]. Theoretical total-energy calculations [89] of several Li structures (hcp, fcc, bcc, 9R) have confirmed that the 9R-phase is favoured at low temperatures and much interest has centred on the observed absence of superconductivity down to 6 mK [90]. The approach to the impulse approximation in liquid lithium at 473 K has recently been investigated by inelastic neutron scattering in the momentum transfer range 0.23 to 29.3 $Å^{-1}$ [87]. The only high-q inelastic studies performed on solid lithium are presented in reference [21]. These were performed on the original eVS spectrometer about six years ago, and are of rather poor quality. The results presented here are undoubtedly the highest quality DINS measurements performed on lithium so far.

The atomic momentum distribution of ^{7}Li in natural polycrystalline lithium has been determined as a function of temperature from 20 to 300K. The experiments were undertaken within the impulse approximation (IA) using the Electron Volt Spectrometer at ISIS. The mean atomic kinetic energy of the lithium nucleus was obtained directly

from our measurements and its temperature dependence is in good agreement with a model derived in the isotropic Debye approximation. This conflicts with an earlier measurement of somewhat poorer statistical quality [2]. It is hoped that the results may prove useful to those determining thermodynamic properties for lithium.

A further objective of this study was to see whether a discontinuity in the mean atomic kinetic energy could be observed in the region of the martensitic transition. This transition is abrupt (at least in the $T \rightarrow 0$ direction) [79]. Just below the transition at 78 K, the bcc lattice constant is $a = 3.483(2)$ Å, whilst the 9R-related structure has lattice parameters of $a = 3.103(2)$ Å and $c = 22.795$ Å[79]. This gives atomic volumes for the 9R and the bcc structures of 21.123 and 21.130 Å respectively, a difference of 0.03 %. The difference in mean atomic spacing is therefore 0.01 %. It is unlikely that the change in mean atomic spacing gives rise to a change in the mean atomic kinetic energy in a polycrystalline measurement (which is averaged over all directions, making any anomaly harder to observe) but the structural change could not be ruled out as a possible source of momentum distribution anomaly at the martensitic transition. No discontinuity was observed in the region of the transition temperature. However, the 9R phase was 'frozen in' upon warming above 78 K (and even remained present at 270 K) so that only the first measurement at 300 K was wholly in the bcc phase. In consequence, it cannot be clear from these measurements whether there is an anomaly in the momentum distribution in the region of the martensitic transition. A single-crystal study of the momentum distribution above and below the martensitic phase transition might reveal changes in the momentum distribution. Along the (110) direction, for example, the spacing between neighbouring planes is about 3.25 Å in the 9R phase and about 3.43 Å in the bcc phase. The eVS has recently had scintillation detectors installed that have increased its sensitivity significantly, and so more than ever eVS is suited to single crystal studies.

5.2 MEASUREMENTS AND DATA ANALYSIS

A white epithermal neutron beam was incident on a slab of natural lithium of dimensions 50mm by 50mm by 3mm thick. The sample was loaded in an open aluminium

frame, which was mounted on an aluminium rod and connected to a closed cycle refrigerator (CCR). Care was taken to ensure that the lithium was not exposed to the atmosphere for longer than necessary. The sample was at an angle of 90 ° to the incident beam and no part of the sample holder was viewed by the incident neutron beam. To avoid detector saturation the sample dimensions were limited to provide a total scattering of 5% of the incident neutron intensity. The detector configuration is the same as for the hydride study presented in chapter 4.

Figure 5.1 illustrates a typical TOF spectrum obtained from one back-scattering detector. Two features are visible in the figure. The more significant peak at 260 to 320 μs corresponds to recoil scattering from ^{7}Li and ^{6}Li nuclei whereas the smaller feature at 320 to 360 μs is the result of recoil scattering from aluminium in the thermal shield surrounding the sample. In order to remove the aluminium scattering, an empty sample-holder measurement was made. The measured scattering was then subtracted from the time-of-flight spectrum with the necessary correction for the counting time. In order to measure the momentum distribution of the ^{7}Li, the scattering from the ^{6}Li was subtracted from the individual time-of-flight difference spectra for each detector and then the difference spectra were transformed into momentum space using an atomic mass of 7 amu. The modelling of the scattering in time-of-flight requires the relative scattering power of the two isotopes, which is the ratio of the product of the abundance and scattering power for each isotope. The isotopic abundances of ^{6}Li and ^{7}Li are 7.52 % and 92.48 % and the total scattering cross-sections are 0.98 and 1.44 barns respectively and so for scattering from natural lithium, this ratio is 1 : 0.055. A least-squares fit in time-of-flight is made to the broad peak with the expression

$$S(t) = R(t) * (aG(t - t_{r7}) + bG(t - t_{r6})) \qquad (101)$$

where * signifies a convolution, R(t) is the instrumental resolution function in time-of-flight, $a : b = 1 : 0.055$, $G(t - t_{ri})$ is a Gaussian centred at the IA recoil peak position $t = t_{ri}$, and t_{r7} and t_{r6} are the recoil peak position for ^{7}Li and ^{6}Li. Chapter 2 details how the resolution function and recoil peak positions in time-of-flight are determined for each spectrum. The variance σ of the momentum distribution of the ^{7}Li was then

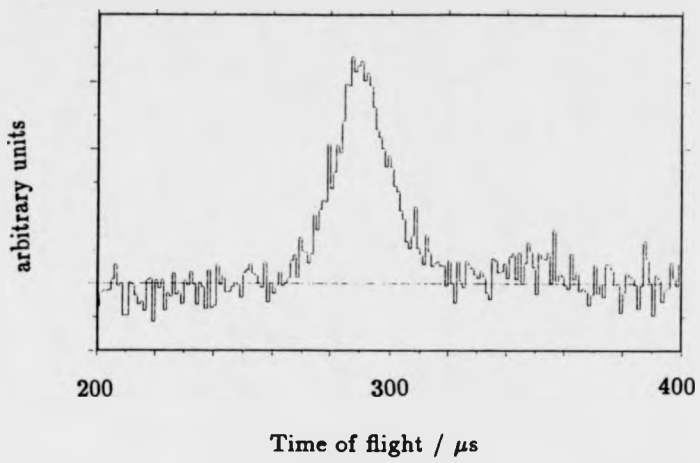

Figure 5.1 The time-of-flight difference spectrum from a back-scattering detector, showing the ^{7}Li and ^{6}Li peak centred at about 290 μs and the narrower peak due to recoil scattering from the aluminium sample holder.

calculated using the standard analysis routines (chapter 2).

The neutron Compton profiles of polycrystalline lithium were measured at 21 temperatures between 300.3 and 22.6 K. The eVS spectrometer permits the simultaneous measurement of DINS profiles and diffraction spectra owing to the two very different time-of-flight regions that these effects are measured over (DINS 100 to 700 μ secs, diffraction 1000 to 20000 μ secs). This means that the structure can be monitored whilst the momentum distribution is measured. Measurements lasted about five hours each. The temperatures and integrated proton current for each measurement are given in table 5.1 along with the results, which will be discussed later.

Upon cooling to 22.6 K, the sample transformed into a mixture of the bcc and the 9R-related structures. Surprisingly, the 9R-related phase remained present in all the subsequent measurements, even above the predicted martensitic transition, the low temperature phase appearing to be frozen in.

Figure 5.2 shows the diffraction data collected with the back-scattering bank of detectors at 300 K (run number 1198). The time-of-flight spectra have been converted to d-spacing after correcting for the electronic delay time. The indices for the bcc phase are marked using measurements by Smith [74]. The region shown is from 1.2 to 2.8 Å. All peaks are assigned to bcc Li. This demonstrates that the sample has not reacted excessively with moisture in the atmosphere. Li and water react to form lithium hydride, which would appear as extra peaks. The presence of hydrogen would appear as a broad peak in the DINS spectra at forward scattering and can cause problems when analysing data from the forward-scattering detectors. No evidence for the presence of hydrogen was seen.

Figure 5.3 shows the diffraction peaks at 22.6 K. Additional peaks have appeared which can be attributed to the 9R phase. The bcc phase is still present, as can be seen by comparison of figure 5.3 with figure 5.2. Aluminium peaks are also visible. The Al 111 peak is marked with a cross at just above 2.3 Å. The position and indices of Bragg reflections belonging to the 9R phase are marked using ideal values for 20 K given

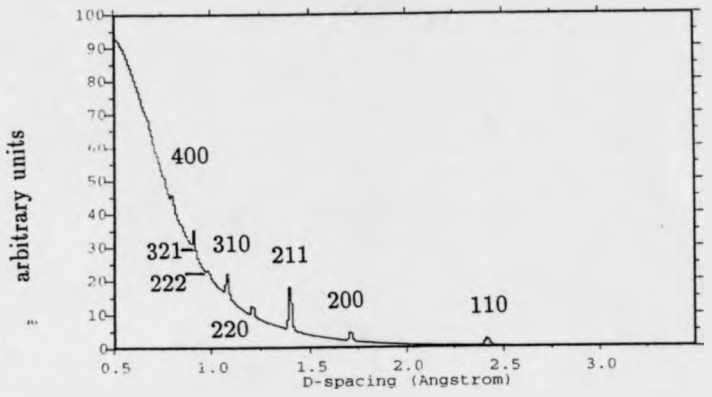

Figure 5.2 The diffraction data collected with the ten back-scattering detectors at 300 K. All peaks are assigned to the bcc phase of Li.

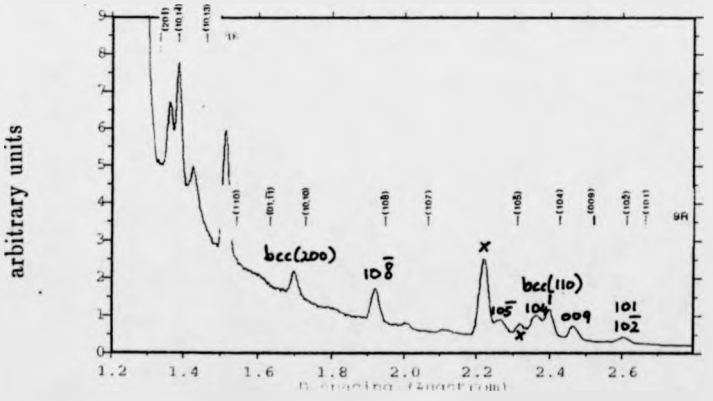

Figure 5.3 The diffraction data at 22.6 K. Additional peaks have appeared which can be largely attributed to the 9R phase of Li.

by Berliner [77]. The difference observed between the eVS results and the ideal peak positions can be attributed to presence of stacking faults. It is known that stacking faults in the 9R structure broaden and cause deviations of the (h k l), $l \neq 0$ diffraction peaks from their ideal values [73], making indexing of the 9R peaks difficult since these peaks are shifted by different amounts. Nevertheless, in figure 5.3 the peaks are marked with the index considered most likely. It has been found in previous studies that a Rietveld refinement is not possible in the 9R phase. Upon warming to 120 K, most of the 9R peaks diminish or disappear, as shown in figure 5.4. A strong peak at 2.22 Å (marked with a cross also) and not attributable to the bcc phase is clearly observable. Though not attributable to the 9R phase, this peak is probably associated with the lithium because it varies in intensity through the temperature scan. Upon cooling to below 70K, the diffraction pattern reverts to that in figure 5.3. Warming to 270 K gives a diffraction pattern shown in figure 5.4.

5.3 RESULTS AND DISCUSSION

Figure 5.5 shows the data collected with the back scattering detector bank at temperatures of 22.6 (circles) and 260.5K (boxes). Each data set is a sum of the data collected in the 10 detectors in this bank of detectors and is normalised to unity. As the resolution broadening is the same in each case the difference in the width of the two data sets is a direct consequence of the temperature change. It should be noted that each data set tends to the zero base line at high momenta thus demonstrating the high quality of these data.

The experimental σ values for both detectors banks at various temperatures between 22.6 and 260.5K are plotted in figure 5.6 and tabulated in table 5.1. Those for the ten detectors at back-scattering (1-10) are shown as circles, whilst the detectors in the angular range 57 to 77 ° (31-50) are shown as boxes. Good agreement is observed between the σ values obtained from the two detector banks. This is a clear indication that the data analysis routines have been successful in extracting σ from the measured spectra. It also indicates that the resolution function is well-defined for these two

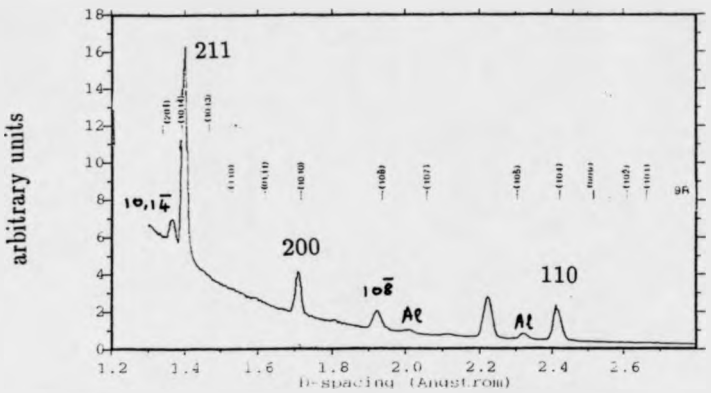

Figure 5.4 At 120 K, the diffraction data show reduced intensity in the 9R peaks. Peaks which cannot be attributed to either the bcc or 9R phase are clearly visible.

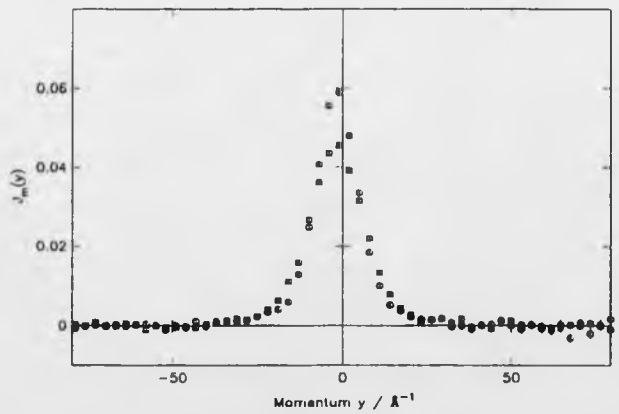

Figure 5.5 The measured neutron Compton profiles summed for the ten back-scattering detectors. The two profiles shown are measured at 22.6 (circles) and 260.5 K (boxes). Because the resolution broadening is the same in each case, the difference in the widths is a direct consequence of the temperature change.

banks. The solid line in figure 5.6 is a theoretical calculation for σ using a Debye model for the density of states, $g(\omega)$. The Debye temperature used in the calculation is obtained by performing a least-squares fit of the theoretical function to the data. The solid line in figure 5.6 is a fit to the back-scattering data. In the case of the back-scattering data, a Debye temperature of $\Theta_D = 401.3 \pm 3.7$ K was obtained. For the detectors 31-50, the fit gave $\Theta_D = 447.2 \pm 5.6$ K. The symmetrised data for the back-scattering data gave a value of $\Theta_D = 419.2 \pm 2.7$. The χ^2 values for the fits were 0.877, 2.02 and 2.81 respectively. A previous measurement of the debye temperature [85] of natural lithium gives $\Theta_D = 395$ K. The unsymmetrised back-scattering data agrees best with this measurement. The good agreement with experiment illustrates that lithium is essentially a Debye solid in the temperature range measured. This result is in contrast to a previous measurement [21].

T / K	$\sigma_{1-10}/\text{Å}^{-1}$	$\sigma_{31-50}/\text{Å}^{-1}$	$\sigma_{S1-10}/\text{Å}^{-1}$
22.6	4.65±0.07	4.90±0.09	4.74±0.05
25.5	4.75±0.07	5.02±0.09	4.80±0.05
33.0	4.69±0.07	4.99±0.09	4.77±0.05
40.5	4.60±0.07	5.04±0.09	4.70±0.05
50.7	4.68±0.07	4.95±0.09	4.78±0.05
60.6	4.71±0.08	4.93±0.11	4.79±0.06
60.8	4.61±0.07	5.08±0.12	4.68±0.05
69.5	4.80±0.08	5.13±0.09	4.91±0.05
79.4	4.80±0.07	5.00±0.10	4.91±0.05
88.2	4.76±0.07	5.33±0.09	4.87±0.05
98.3	5.07±0.08	5.16±0.10	5.15±0.05
98.8	4.86±0.15	5.09±0.20	4.97±0.10
107.5	4.90±0.07	5.29±0.10	5.03±0.05
117.6	5.15±0.09	5.44±0.13	5.22±0.07
126.7	5.06±0.07	5.28±0.09	5.13±0.05
136.7	5.27±0.07	5.50±0.09	5.36±0.05
174.5	5.71±0.13	5.87±0.17	5.81±0.09
203.0	5.94±0.10		6.00±0.07
232.0	6.15±0.08	6.65±0.10	6.21±0.06
260.5	6.54±0.09	7.06±0.13	6.21±0.06
300.3	6.78±0.08	6.97±0.10	6.85±0.06

Table 5.1 The instrument calibration parameters.

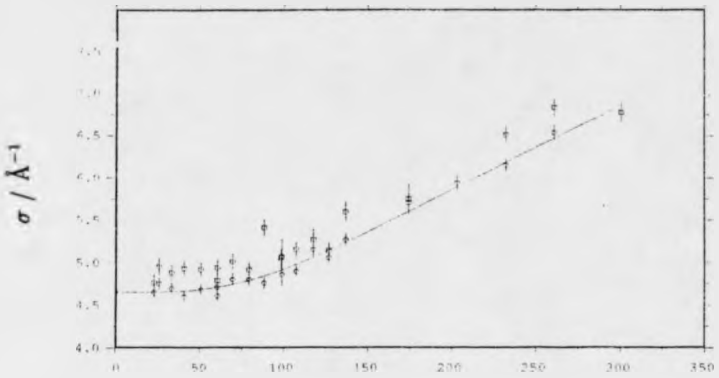

Figure 5.6 The temperature dependence of σ in the range 21.6 to 300.3 K. The circles are the eVS measurements, whilst the solid line is the calculation in the harmonic Debye approximation. Also shown (boxes) are the data from the analysis of detectors 31-50 at forward scattering.

The experiment presented in reference [21] was performed on natural lithium at room temperature and gives for the mean natural Li kinetic energy values of 705 ± 75 and 1000 ± 300 K for Au and U analyser foil measurements respectively. These results of rather poor statistical accuracy correspond to σ values of $\sigma = 8.2 \pm 0.4$ and $\sigma = 9.8 \pm 1.3$ $Å^{-1}$. The eVS result at 260.5 K was $\sigma = 6.54 \pm 0.09$ $Å^{-1}$

Simulations of the measured neutron Compton profile, $J_m(y)$, were performed using the Debye Density of states and a Debye temperature of 400 K, in the same way as the simulations of metal hydride and deuteride data in chapters 3 and 4. Figure 5.7 shows the comparison of the simulated σ values (circles) against the theoretical calculation of σ in the Debye model with a Debye temperature of 400 K (solid line). The very close agreement indicates that the analysis routines described in chapter 2 are effective at extracting the correct variance of $J(y)$ from $J_m(y)$. As can be seen from the simulations in chapter 3 and 4, the simulated (and measured) $J_m(y)$ are slightly asymmetric. Despite this deviation from a Voigt function, the analysis routines extract σ values very close to the Debye model value given by the Debye density of states from which the $J_m(y)$ were simulated. Figure 5.8 shows the summed back-scattering data for the measurement performed at 98.3 K. The solid line is the simulation performed at 100 K. The agreement is very good.

Figure 5.9 compares the symmetrised and unsymmetrised back-scattering data. The circles and crosses are the unsymmetrised and symmetrised data respectively; the lower and upper solid lines are the Debye fits for the unsymmetrised and symmetrised data respectively. The difference in the Debye temperature is just over 4 %.

It is possible in principle to determine mean kinetic energies from the specific heat capacity at constant pressure since

$$\frac{\partial}{\partial T} E_{vib} = C_p. \tag{102}$$

In the harmonic approximation, $E_{kin} = 0.5 E_{vib}$. However, no measurements of the lithium density of states were found in the literature.

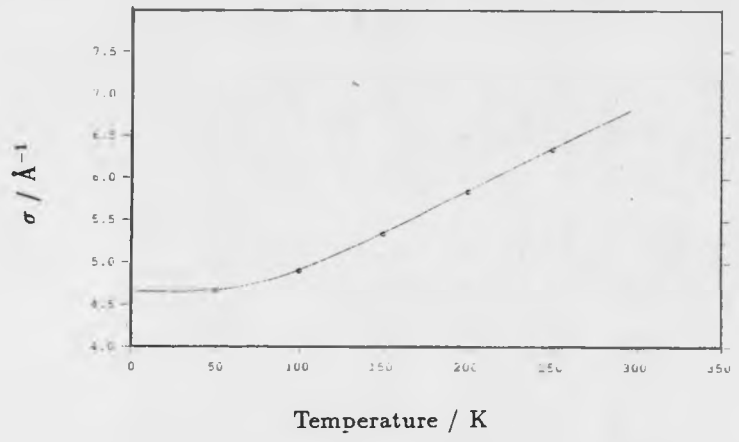

Figure 5.7 Simulations of the eVS data were made from the Debye density of states using Θ_D = 400 K. This figure shows the resulting σ values determined from these simulations against the Debye model fit to the back-scattering data (circles in figure 5.6).

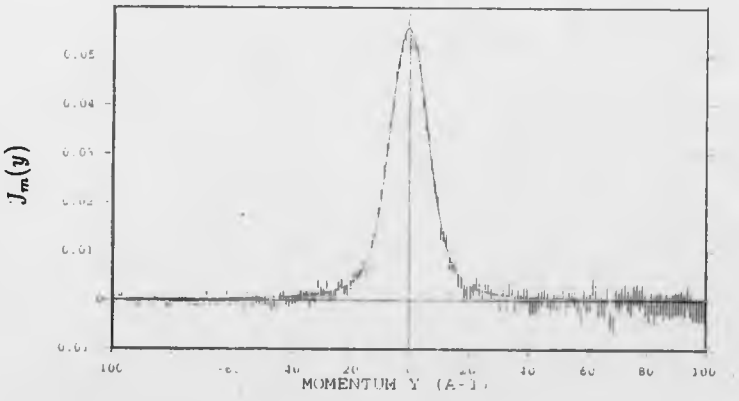

Figure 5.8 A simulation of the eVS data for the summed data of the ten back-scattering detectors for the measurement at 260.5 K.

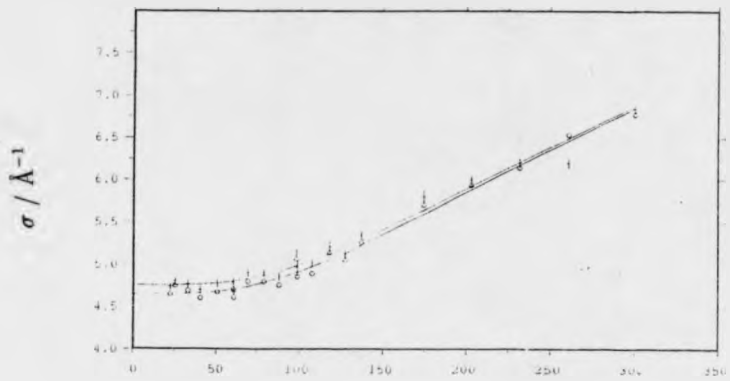

Figure 5.9 The crosses show the σ values determined from the symmetrised back-scattering data. The circles are the unsymmetrised data (figure 5.6). The upper solid line shows the Debye fit to the symmetrised data, and the lower solid line is the corresponding fit to the unsymmetrised data. The Debye temperature determined from the fit is 419±2.7 K as opposed to 401.3 ± 3.7 K for the unsymmetrised data.

5.4 SUMMARY

The mean kinetic energy of ^{7}Li in natural lithium metal has been determined in the temperature range 20 to 300 K by deep inelastic neutron scattering. The back-scattering data (detectors 1-10) had the narrowest associated resolution function and is therefore considered more reliable than the data from detectors 31-50. The half-width of the Lorenzian contribution to the resolution function for the back-scattering detectors is 2.92 $Å^{-1}$, whereas the half-width for the detectors 31-50 is about 4.60 $Å^{-1}$. Nevertheless, the agreement between the two data-sets is good. There is an observed shift of about 1% between the two. The back-scattering data also give a better fit to a Debye model. The symmetrised back-scattering data give σ typically 2 % larger than the unsymmetrised data for the same detectors. From the χ^2 values obtained from the Debye model fits to the three data sets, the unsymmetrised back-scattering data gives the best fit. The symmetrisation procedure relies upon an accurate calibration. Any shift of $J_m(y)$ in y-space due to a calibration error will affect the width of the symmetrised distribution and therefore the derived σ value. A calibration error affects the data more with increasing mass of the scattering particle. The conclusion is that the kinetic energy of the ^{7}Li nuclei is no more than 2 % greater than the Debye model.

CHAPTER 6

Further developments

With the installation and testing of scintillation detectors on eVS in 1993, it is anticipated that eVS data will be of greatly improved statistical accuracy. It is anticipated that it will become necessary to include a fitting of the first Sears' term to the measured neutron Compton profile, which in turn implies some knowledge about the scattering potential.

The resolution of eVS can be improved by cooling the analyser foils. The 6671 meV resonance in uranium, which for a 10 μ thick foil at room temperature has a Gaussian variance of 61.8$\pm$0.1 meV will at liquid nitrogen temperatures have a variance of 40.5$\pm$0.1meV. There are associated problems with a cooled analyser foil system such as the formation of ice (hydrogen scatters strongly) and the requirement that the temperature is stable during the measurement. If these can be overcome, then for uranium foils this will be a useful exercise. It would be especially useful in the case of liquid helium measurements since these require a narrow resolution function. With the increase in statistical accuracy will come a need to be able to deconvolute the measured neutron Compton profile with the resolution function. There is some indication for example, that the discrepancy between the mean kinetic energy determined from gold and uranium foils is due to deviation from the resolution function from a Voigt-function (Gaussian function in the case of uranium).

With the benefit of increased statistical accuracy comes the need to determine more accurately the resolution function. At the moment, inconsistency between measurements made with gold and uranium analysers have been found. These are apparent with high mass systems where the resolution is a larger fraction of the width of the system being measured. These need to be resolved. Regular calibration runs are required to fully understand the resolution function. A good test of this will be the analysis of recently collected neon data. Natural neon (^{20}Ne and ^{22}Ne) were measured on eVS

using both gold and uranium analyser foils. The three resonances of uranium at 6671, 20872 and 36680 meV should give consistent values for the mean kinetic energy. These measurements are currently being analysed. Path Integral Monte-Carlo calculations have already been performed for the four measured temperatures of liquid and solid neon [95], offering a good theoretical comparison for these measurements.

A promising area of development is the use of eVS as a spectrometer for the measurement of anisotropies in the momentum distribution in single crystals. Such measurements have already been performed with a single crystal of VH. It is expected that in systems where the atomic spacing is strongly temperature dependent, that the atomic momentum distribution should also show some anisotropy. The eVS spectrometer measures the momentum distribution of the sample in many different directions at the same time, so in this way a two-dimensional map of the momentum distribution can be obtained from one measurement (in the plane of the instrument).

An automated analysis procedure will be developed to enable users of the eVS spectrometer to analyse their own data in response to a series of straightforward questions. This will be of great benefit to the instrument scientists currently working on the eVS. At the moment, data must be analysed by the instrument scientists and not by the users. A manual will accompany the automated analysis procedure.

No correction currently exists for multiple scattering. This will need to be rectified. Though not evident in the measurements presented in this thesis, multiple scattering has been observed in scattering from pressurised liquid hydrogen (at 1000 bars). It manifests itself as a high energy tail on the data.

The broad extent of future areas of development has been briefly outlined above. With continued development, the electron-volt spectrometer has a lot to offer the field of condensed matter research.

References

[1] Rutherford Laboratory Report RL-77-064/C, 'A Pulsed Neutron Facility for Condensed Matter Research', edited by L. C. W. Hobbis, G. H. Rees and G. C. Stirling.

[2] A. D. Taylor, Rutherford Appleton Laboratory Report RAL-84-120 (1984).

[3] M. J. Cooper, Rep. Prog. Phys. **48** 45 (1985).

[4] V. F. Sears, Phys. Rev. B, **30** 44 (1984).

[5] S. W. Lovesey, Theory of Neutron Scattering from Condensed Matter, Volume 1, Oxford Science Publications (1984).

[6] G. L. Squires, Thermal Neutron Scattering, Cambridge University Press (1978).

[7] V. F. Sears, Phys. Rev. **185** 200 (1969).

[8] J. Mayers, Phys. Rev. B, **41** 1 41 (1990).

[9] J. Mayers, C. Andreani and G. Baciocco, Phys. Rev. B, **39** 4 2022 (1989).

[10] J. J. Weinstein and J. W. Negele, Phys. Rev. Lett., **49** 14 1016 (1982).

[11] V. F. Sears, Phys. Rev. A, **5** 1 452 (1971).

[12] V. F. Sears, Phys. Rev. A, **7** 1 340 (1973).

[13] G. Reiter and R. Silver, Phys. Rev. Letters **54** 10 1047-1050.

[14] G. B. West, Phys. Rep. **18C** 263 (1975).

[15] J. Mayers, Rutherford Appleton Laboratory Report RAL-89-104 (1989).

[16] K. W. Herwig, P. E. Sokol, W. M. Snow and R. C. Blasdell, Phys. Rev. B **44** 1 308 (1991).

[17] S. Stringari, Phys. Rev. B, **35** 4 2038 (1987).

[18] A. C. Evans, J. Mayers, D. N. Timms and M. J. Cooper, Zeitschrift für Naturforschung **A48** 425 (1993).

[19] R. Hempelmann, D. Richter and A. Kollmar, Z. Phys. B **44** 159 (1981).

[20] M. P. Paoli and R. S. Holt, J. Phys. C: Solid State Phys. **21** (1988) 3633.

[21] M. P. Paoli, D. Phil. Thesis, University of Oxford (1988).

[22] D. N. Timms, R. S. Holt, F. Itoh, T. Kobayasi and H. Nara, J. Phys. Condens. Matter **2** 10517 (1990).

[23] P.C. Hohenberg and P. M. Platzman, Phys. Rev. **152** 1 (1966) 198.

[24] T. R. Sosnick, W. M. Snow, R. N. Silver and P. E. Sokol, Phys. Rev. B **43** 1 (1991) 216.

[25] D. A. Peek and R. O. Simmons, J. Chem. Phys. **94** 4 (1991) 3169.

[26] D. A. Peek, I. Fujita, M. C. Schmidt and R. O. Simmons, Phys. Rev., **B45**, 17, (1992), 9680

[27] D. A. Peek, M. C. Schmidt, I. Fujita and R. O. Simmons, Phys. Rev. **B45**, 17, (1992), 9671.

[28] M. A. Fradkin, S.-X. Zeng and R. O. Simmons, paper presented at the Sagamore X Conference, Konstanz September 1991.

[29] M. Warner and S. W. Lovesey, Z. Phys. B - Condensed Matter **51** (1983) 109.

[30] E. O. Wollan and G. G. Shull, Phys. Rev. **73** (1948) 830.

[31] R. S. Carter, H. Palevsky and R. J. Hughes, Phys. Rev. **106** (1957) 1168.

[32] B. N. Brockhouse, Inelastic scattering of neutrons in solids and liquids, vol. 1 (IAEA, Vienna, 1961) p. 189.

[33] G. S. Samosvat, Yu. S. Sayasov and V. T. Chuburkov, Sov. Phys. JETP **27** (1968) 15

[34] R. J. Newport, P. A. Seeger and W. G. Williams,

[35] R. M. Brugger, A. D. Taylor, C. E. Olsen, J. A. Goldstone and A. K. Soper, Nucl. Instr. and Meth. **221** (1984) 393-407

[36] H. Rauh, S. Ikeda and N. Watanabe, Nucl. Instr. and Meth. **224** 469 (1984).

[37] J. M. Carpenter and N. Watanabe, Nucl. Instr. and Meth. **213** 311 (1986).

[38] D. R. Allen, E. W. Mitchel and R. N. Sinclair, J. Phys. E: Sci. Instrum. **13** 639 (1980).

[39] R. J. Newport, J. Penfold and W. J. Williams, Nucl. Instr. and Meth. **224** (1984) 120-132.

[40] C.-K. Loong, S. Ikeda and J. M. Carpenter, Nucl. Instr. Meth. **A260** 381 (1987).

[41] H. Rauh and N. Watanabe, Phys. Letts., **A100**, (1984), 244.

[42] W. E. Lamb, Phys. Rev. **55** (1939) 190.

[43] M. S. Nelkin and D. E. Parks, Phys Rev **119** (1960) 1060.

[44] R. Cywinski, J. Mayers and W. G. Williams, Rutherford Appleton Laboratory Report RL-81-043 (1981).

[45] J. Mayers and A. C. Evans, Rutherford Appleton Laboratory report RAL-91-048 (1991).

[46] C. G. Windsor, 'Pulsed Neutron Scattering', Taylor and Francis, 1981.

[47] C. Andreani, G. Baciocco, R. S. Holt and J. Mayers, Nucl. Inst. Meth. **A276** (1989) 297.

[48] R. G. Parry, K. J. Knowles, C. Moreton-Smith, R. T. Lawrence, W. C. A. Pulford and M. A. Sturdy, 'PUNCH User Guide', RAL (1988).

[49] S. F. Mughabghab, M. Divadeenam and N. E. Holden, 'Neutron Cross-sections' Vol. 1 Parts A and B (Academic Press, 1981, 1985)

[50] J. Mayers, Rutherford Appleton Laboratory.

[51] J. R. D. Copley, Comput. Phys. Commun. **7** 289 (1974).

[52] C. Andreani, J. Mayers, P. Postorino and M. A. Ricci, Molecular Physics **73** 4 737 (1991).

[53] C. Andreani, P. Bosi, F. Sacchetti and C. K. Loong, J. Chem. Phys. **83** 2 750 (1985).

[54] D. K. Ross, P. F. Martin, W. A. Oates and R. Khoada-Bakhish, Zeit. fur Phys. Chemie NF, **114** 5221 (1979).

[55] R. Osborn, Rutherford Appleton Laboratory Report RAL-91-011 (1991).

[56] H. E. Flotow and D. W. Osborne, J. Chem. Phys. **34** 1418 (1961).

[57] D. F. Mcmorrow, R. A. Cowley, R. M. Nicklow, P. W. Mitchel, A. D. Taylor and M. Mostoller, J. Phys. Condens. Matter **2** 1045 (1990).

[58] *Hydrogen in Metals I (1976)*, ed. by G. Alefeld and J. Völkl (Springer-Verlag, Berlin).

[59] V. A. Somenkov, A. V. Gurskaya, M. G. Zemlyanov, M. E. Kost, N. A. Chernoplekov and A. A. Chertkov, Soviet Physics - Solid State **10** 5 1076 (1967).

[60] J. G. Couch, O. K. Harling and L. C. Clune, Phys. Rev. B **4** 2675 (1971).

[61] S. S. Malik, D. C. Rorer and G. Brunhart, J. Phys. F:Met. Phys. **14** 73 (1984).

[62] J. Tomkinson, J. Penfold and S. T. Robertson, Rutherford Appleton Laboratory Report RAL-89-074 (1989).

[63] D. Richter and S. M. Shapiro, Phys. Rev. B **22** 2 599 (1980).

[64] J. Eckert, J. A. Goldstone and D. Tonks, Phys. Rev. B **27** 4 1980 (1983).

[65] D. Klauder, V. Lottner and H. Scheuer, Solid State Commun. **32** 617 (1979).

[66] Unknown source - ZrH_2 diffraction reference.

[67] T. Schober, H. Wenzl in *Hydrogen in Metals II (1976)*, ed. by G. Alefeld and J. Völkl (Springer-Verlag, Berlin.)

[68] H. Zabel and J. Peisl, J. Phys. F: Metal Phys. 1979 **9** 1461-1476.

[69] P. Martel, E. C. Svensson, A. D. B. Woods, V. F. Sears and R. A. Cowley, J. Low Temp. Phys. **23** 285 (1976).

[70] A. D. B. Woods and V. F. Sears, Phys. Rev. Lett. **39** 415 (1977).

[71] C. S. Barret and O. R. Trautz, Trans. Am. Inst. Min. Metall. Pet. Eng. **175** 57 (1948).

[72] C. M. McCarthy, C. W. Tompson and C. A. Werner, Phys. Rev. B **22** 574 (1980).

[73] R. Berliner and S. A. Werner, Phys. Rev., **B34** 3586 (1986).

[74] H. G. Smith, R. Berliner and J. D. Jorgensen, Physica, **B156 & B157** 53 (1989).

[75] A. W. Overhauser, Phys. Rev. Lett. **53** 64 (1984).

[76] H. G. Smith, R. Berliner, J. D. Jorgensen, M. Nielsen and J. Trivisonno, Phys. Rev. B **41** 2 1231 (1990).

[77] R. Berliner, O. Fajen, H. G. Smith and R. L. Hitterman, Phys. Rev. B **40** 18 (1989).

[78] A. W. Overhauser, Phys. Rev. Lett. **53** 64 (1984).

[79] H. G. Smith, Phys. Rev. Lett., **58** 1228 (1987).

[80] C. S. Barret, Acta. Cryst., **9** 671 (1956).

[81] T. N. Mel'nikova and A. G. Mozgovoi, High Temp., **26** 6 (1988).

[82] G. J. Vazquez, Rev. Mex. de Fisica, **36** 4 572 (1990).

[83] G. Sugiyama, G. Zerah and B. J. Alder, Physica **A 156** 144 (1989).

[84] M. J. Cooper, B. G. Williams, R. E. Borland and J. R. A. Cooper, Phil. Mag. **22** 441 (1970).

[85] H. G. Smith, G. Dolling R. M. Nicklow, P. R. Vijayaraghavan and M. K. Wilkinson, Neutron Inelastic Scattering (International Atomic Energy Authority, Vienna, 1968), Vol. 1, p. 149.

[86] W. Schwarz and O. Blaschko, Physica B **180 &** 181 271 (1992).

[87] P. Verkerk, P. H. K. de Jong, M. Arai, S. M. Bennington, W. S. Howells and A. D. Taylor, Physica B **180 &** 181 834 (1992).

[88] G. Ernst, C. Artner, O. Blaschko and G. Krexner, Phys. Rev. B **33** 9 6465 (1986).

[89] A. D. Zdetsis, Phys. Rev. B **34** 11 7666 (1986).

[90] A. Y. Liu and M. L. Cohen, Phys. Rev. B 44 17 9678 (1991).

[91] Y. R. Wang and A. W. Overhauser, Phys. Rev. B **34** 12 8401 (1986).

[92] A. D. Taylor and M. P. Paoli, unpublished.

[93] R. S. Holt, L. M. Needham and M. P. Paoli, Phys. Lett. **126** 373 (1987).

[94] R. N. Silver, Phys. Rev. B **37** 3794 (1988); **38**2283 (1988); in *Momentum Distributions* (Ref 10) p 123.

[95] E. Merzbacher, Quantum Mechanics, second edition, Wiley (1970).

[96] P. W. Atkins, Molecular Quantum Mechanics, Oxford University Press, Oxford (1983).

LIST OF ABBREVIATIONS

DAE	data acquisition electronics
DG	direct geometry
DINS	deep inelastic neutron scattering
eVS	electron-volt spectrometer
FBS	filtered-beam spectrometer
FWHM	full-width at half-maximum
HRMECS	high resolution medium energy chopper spectrometer
HWHM	half-width at half-maximum
IA	impulse approximation
IG	inverse geometry
INS	inelastic neutron spectrometer
IPNS	intense pulsed neutron source
NCP	neutron Compton profile
NCS	neutron Compton scattering
RDS	resonance detector spectrometer
SIA	Stringari impulse approximation

APPENDIX 1

First-order perturbation theory applied to the harmonic oscillator

The definition of the perturbed harmonic potential is

$$V(x) = \frac{1}{2}M\omega^2 x^2 + V_1(x) \tag{103}$$

and

$$V_1(x) = \epsilon_1 \left(\frac{x}{l}\right)^3 + \epsilon_2 \left(\frac{x}{l}\right)^4 \tag{104}$$

l is a characteristic length and is given by $l = \sqrt{\hbar/M\omega}$. The perturbation parameters ϵ_1 and ϵ_2 have dimensions of energy. The x^3 term affects the energy levels in second-order perturbation theory, and the x^4 term affects the energy levels in first-order perturbation theory. The nth eigenvalue of the perturbed system is given by [95]

$$E'_n = E_n + \frac{3}{4}\epsilon_2(2n^2 + 2n + 1). \tag{105}$$

The perturbed ground-state eigenfunction is given by [96]

$$u'_0 = u_0(\zeta) + \sum_{n=1}^{4} \left(\frac{\langle n|V_1(\zeta)|0\rangle}{E_0 - E_n}\right) u_n(\zeta) \tag{106}$$

where $u_n(\zeta)$ is the normalised harmonic oscillator eigenfunction associated with the nth energy level, and

$$u_n(\zeta) = (2^n n! l\sqrt{\pi})^{-\frac{1}{2}} \exp(\frac{-\zeta^2}{2}) H_n(\zeta). \tag{107}$$

$H_n(\zeta)$ is the Hermite polynomial of nth order defined by

$$H_n(\zeta) = (-1)^n \exp(\zeta^2) \frac{d^n}{d\zeta^n} \exp(-\zeta^2) \tag{108}$$

and $\zeta = x/l$. The matrix elements in equation 106 are evaluated from expressions given in Merzbacher:

$$\langle 1|V_1(\zeta)|0\rangle = \epsilon_1\langle 1|\zeta^3|0\rangle = 3(\frac{1}{2})^{\frac{3}{2}}\epsilon_1 \tag{109}$$

$$\langle 2|V_1(\zeta)|0\rangle = \epsilon_2\langle 2|\zeta^4|0\rangle = (\frac{9}{2})^{\frac{1}{2}}\epsilon_2 \tag{110}$$

$$\langle 3|V_1(\zeta)|0\rangle = \epsilon_1\langle 3|\zeta^3|0\rangle = (\frac{3}{4})^{\frac{1}{2}}\epsilon_1 \tag{111}$$

$$\langle 4|V_1(\zeta)|0\rangle = \epsilon_2\langle 4|\zeta^4|0\rangle = (\frac{3}{2})^{\frac{1}{2}}\epsilon_2 \tag{112}$$

The perturbed spatial eigenfunction is a sum of terms which have analytical solutions to their Fourier transforms. The existence of a simple transformation between harmonic oscillator eigenfunctions in spatial coordinates and momentum coordinates is a special feature of this system. The advantage of this is that it is possible to calculate an analytical form for the perturbed eigenfunction in momentum coordinates and hence the momentum distribution.

The harmonic oscillator eigenfunction in momentum representation is given by

$$\tilde{u}_n(p) = \frac{i^{-n}}{\sqrt{M\omega}} u_n\left(\frac{p}{M\omega l}\right). \tag{113}$$

The momentum distribution is then given by

$$n(p) = \tilde{u}_n(p)\tilde{u}_n^*(p) \tag{114}$$

where $\tilde{u}_n^*(p)$ is the complex conjugate of $\tilde{u}_n(p)$. It follows that

$$n(p) = \frac{A}{M\omega l\sqrt{\pi}} \exp(-p'^2)\left[(aH_0(p') - cH_3(p') + eH_5(p'))^2 + (dH_4(p') - bH_2(p'))^2\right] \tag{115}$$

where $p' = p/(M\omega l)$, $a = 1$, $b = -\frac{3\epsilon_1}{4\hbar\omega}$, $c = -\frac{3\epsilon_2}{8\hbar\omega}$, $d = -\frac{\epsilon_1}{24\hbar\omega}$, and $e = -\frac{\epsilon_2}{64\hbar\omega}$. A is defined by the requirement that $\int_{-\infty}^{\infty} n(p)dp = 1$ The kinetic energy is evaluated by determining the expectation value of $p^2/2M$

$$\frac{1}{2M}\int_{-\infty}^{\infty} p^2 n(p)dp = \frac{\langle p^2\rangle}{2M}. \tag{116}$$

To evaluate this integral, the following integrals are needed:

$$\int_{-\infty}^{\infty} [H_n(x)]^2 \exp(-x^2)dx = (2^n n!\sqrt{\pi})^{\frac{1}{2}}, \tag{117}$$

the standard integral

$$\int_{-\infty}^{\infty} \exp(-x^2)dx = \sqrt{\pi} \tag{118}$$

VARIABLE PRINT QUALITY